



Sentinel-6 MF Poseidon-4 radar altimeter: Main scientific results from S6PP LRM and UF-SAR chains in the first year of the mission

Salvatore Dinardo^{a,1,*}, Claire Maraldi^b, Emeline Cadier^c, Pierre Rieu^{d,2},
Jeremie Aublanc^c, Adrien Guerou^c, Francois Boy^b, Thomas Moreau^c,
Nicolas Picot^b, Remko Scharroo^a

^a EUMETSAT (European Organisation for the Exploitation of Meteorological Satellites), Eumetsat Allee 1, 64295 Darmstadt, Germany

^b CNES (Centre National d'Etudes Spatiales), 18 Av. Edouard Belin, 31400 Toulouse, France

^c CLS (Collect Localisation Satellites), Parc Technologique du Canal, 11 Rue Hermès, 31520 Toulouse, France

^d Magellium, Parc Technologique du Canal, 1 Rue Ariane, 31520 Toulouse, France

Received 11 July 2022; received in revised form 5 July 2023; accepted 16 July 2023

Available online 22 July 2023

Abstract

Poseidon-4 is a dual-frequency redundant radar altimeter on board the European Commission Copernicus Programme Sentinel-6 Michael Freilich satellite, that represents a significant breakthrough with respect to its predecessors Jason-class altimeters due to its digital architecture and to its innovative measurements and calibration modes.

In the framework of the Sentinel-6 Michael Freilich commissioning preparatory activities, CNES has contracted CLS for the development of a Sentinel-6 Processing Prototype (S6PP) application. S6PP is a multi-chain processing suite able to process Sentinel-6 Level-1A and Level-1B data products up to Level-2. The novel algorithms developed in the CNES/CLS research and development activities are implemented within S6PP and validated to support the different thematic applications (in particular inland water and ocean) and in view of promoting them for possible implementation in the operational ground segment.

The present work covers in particular the main results over open ocean for the main altimetric geophysical variables over the sea surface (sea surface height anomaly, significant wave-height, sigma-nought and wind speed) derived by the Low-Resolution Mode (LRM) and High-Resolution Mode (HRM) chains of S6PP in terms of precision, accuracy, spectral content and measurement stability.

Given the reported variation of the payload in-orbit temperatures along with the reported instrumental ageing, and given the tight requirement to measure the GMSL (Global Mean Sea Level) in seamless continuity with Jason-3, the clear goal for S6PP was to process the S6-MF data with the minimum possible level of approximations along the processing pipeline but still maintaining a very efficient prototype from the computational point of view.

For this scope, a novel and computationally efficient numerical retracking scheme with interface to the in-flight PTR (Point Target Response) provided by the instrument calibration chain has been put in place within S6PP for both the Low-Resolution and High-Resolution modes whereas the Delay-Doppler beam-forming is carried out by applying the range walk correction based on a computationally efficient algorithm (Chirp Zeta-Transform).

* Corresponding author.

E-mail addresses: salvatore.dinardo@eumetsat.int (S. Dinardo), claire.maraldi@cnes.fr (C. Maraldi), ecadier@groupcls.com (E. Cadier), pierre.rieu@magellium.fr (P. Rieu), jaublanc@groupcls.com (J. Aublanc), aguerou@groupcls.com (A. Guerou), francois.boy@cnes.fr (F. Boy), tmoreau@groupcls.com (T. Moreau), nicolas.picot@cnes.fr (N. Picot), remko.scharroo@eumetsat.int (R. Scharroo).

¹ Salvatore Dinardo worked on the study when he was affiliated with CLS.

² Pierre Rieu worked on the study when he was affiliated with CLS.

The impact of the range walk correction and of the in-flight PTR interface is assessed for HRM and LRM, respectively.

The paper shows that the proposed processing baseline ensures a dataset robust from the currently known instrumental degradation or ageing issues, both in LRM and HRM mode and, once this is done, that Sentinel-6 Michael Freilich global mean sea level measurement is in line with the one measured by Jason-3.

© 2023 COSPAR. Published by Elsevier B.V. All rights reserved.

Keywords: Radar altimetry; Chirp zeta-transform; Calibration; Sentinel-6 Michael Freilich; Delay-Doppler; Retracking

1. Introduction

Sentinel-6 is an Earth Observation satellite constellation developed in partnership between ESA, EUMETSAT, European Commission, NASA, and NOAA with the support of CNES as part of the European Commission Copernicus Programme (European Union, 2014). The Sentinel-6 mission will be implemented by two identical satellites. The first satellite of this Sentinel-6 constellation (Sentinel-6 Michael Freilich, Sentinel-6 MF or S6-MF for short) was launched on 21 November 2020 (Copernicus Service, 2020) from Vandenberg Space Force Base in California and named after Dr Michael Freilich, former director of NASA Earth Science Division, whereas the second satellite of the constellation (Sentinel-6B) is expected to be launched in 2025.

The S6-MF satellite carries a suite of scientific sensors devoted to surface topography measurements:

- POSeidon-4 (POS-4) radar altimeter,
- Advanced Microwave Radiometer-Climate (AMR-C) microwave radiometer,
- DORIS (Doppler Orbitography and Radio-positioning Integrated by Satellite) receiver,
- Laser Retro-Reflector Array (LRA) receiver,
- Global Navigation Satellite System-Precise Orbit Determination (GNSS-POD) Receiver

And to atmospheric sounding measurements (two Radio Occultation GNSS receivers), (Donlon et al, 2021). POS-4, the main payload carried on board S6-MF, is an electronically redundant dual-frequency (15.575 GHz and 5.41 GHz) radar altimeter manufactured by THALES-Alenia Space. The altimeter is supported by the AMR-C sensor which is a three-frequency (18.7 GHz, 23.8 GHz, and 34.0 GHz) Dicke-type microwave radiometer provided by NASA/JPL to provide the wet tropospheric path delay. The GNSS-POD receiver, the LRA receiver and the DORIS receiver ensure precise determination of the satellite orbit, a real-time navigation system and ultra-stable clock signal of 10 MHz that drives both the POS-4 and GNSS-POD.

Finally, to support the high-resolution mode from the Poseidon-4 altimeter (as for instance in the coastal zone), an experimental High-Resolution Microwave Radiometer (HRMR) subsystem was integrated into the AMR-C in order to provide high spatial resolution water vapour mea-

surements at 5 km resolution at frequencies 90, 130 and 168 GHz (Donlon et al., 2021).

The mission objective of S6-MF (Scharroo et al., 2016) is to provide accurate, continuous, and timely topography measurements over marine and continental waters during its nominal life duration of 5.5 years. It will also provide wind and wave measurements over marine surfaces, and it is expected to offer improved performances in the marine coastal zones with respect to Jason-class altimeters.

In the framework of the Copernicus services portfolio, S6-MF will respond in an operational context to the routine needs of many thematic applications such as: marine meteorology, operational oceanography/ocean-modelling and climatology with three different data latencies: NRT (Near Real Time, around three hours), STC (Short Time Critical, around 36 h) and NTC (Non Time Critical, around 60 days) delivered by the EUMETSAT PDAP (Payload Data Acquisition and Processing) ground segment by means of its integrated PDP (Payload Data Processing) facilities.

With regard to the climate monitoring demands, the mission design has been driven by the need to provide seamless continuity to the Topex/Poseidon and Jason series satellites in measuring the global sea level trends and to extend this long climate-record of sea level measurements well beyond 2030 with an error of less than 1 mm/year on the GMSL (Global Mean Sea level) trend (Scharroo and von Engeln, 2018).

Once in routine operation, the S6-MF data products are expected to be of sufficient accuracy and quality so that S6-MF can take the role of the “reference” altimeter mission against which all the other in-flight radar altimeter missions can be cross-calibrated in the Ocean Surface Topography Virtual Constellation (OST-VC), under the coordination and aegis of the Committee for Earth Observation Satellites (CEOS).

In order to reach these tight measurement stability goals, the Poseidon-4 altimeter has been outfitted with new dedicated calibration modes such as CAL-1 ECHO CAL and CAL-1 INSTR (see section 2.2), whereas the AMR-C payload integrates an external Supplemental Calibration System (SCS) that includes a small reflector placed between the radiometer feed-horn and the main reflector able to direct the AMR-C beam “on demand” to a black-body warm calibration target (~300 K) or to a cold space target (~3K) in order to calibrate the radiometer internally and accurately.

On 28 November 2020, the S6-MF Poseidon-4 altimeter was successfully powered-on in orbit and the first data acquired (EUMETSAT, 2020).

In compliance with the end-user requirements (Scharroo and von Engel, 2018), the S6-MF nominal orbit is the same as for the preceding Topex/Poseidon and Jason series missions: a non-sun-synchronous LEO (Low-Earth Orbit) with a reference altitude of 1347 km, an orbital inclination of 66, an orbit period of around 115 min and repeat cycle of around 10 days.

On 18 December 2020, S6-MF reached this nominal orbit, flying in tandem only 30 s behind Jason-3.

This tandem phase with Jason-3 was supposed to last 12 months (ESA, 2020) but it was extended to March 2022, after the decision to switch over the altimeter from side-A (nominal radar chain) to side-B (redundant radar chain), to allow the characterisation of the full POS-4 (i.e. both sides), thus better safeguarding the 30 year time series in an event of failure of a single altimeter side. The switch-over to side-B took place on 14 September 2021 (EUMETSAT, 2021a, 2021b, 2021c).

In 2019, in the framework of the S6-MF commissioning preparatory activities, CNES contracted CLS for the development of an end-to-end Sentinel-6 multi-chain processing prototype application referred to as “Sentinel-6 Processing Prototype”, S6PP for short.

The present work addresses the most prominent scientific results over open ocean for the main altimetric geophysical variables over the sea surface: sea surface height (SSH), sea surface height anomaly (SSHA), significant wave-height (SWH), sigma-nought (σ_0) and wind speed from the LRM (Low-Resolution Mode) and HRM (High-Resolution Mode, also known as UnFocused-Synthetic Aperture Radar or UF-SAR) chains of S6PP. Results are analysed in terms of precision, accuracy, spectral content and measurement stability. Continuity with the Jason-3 reference mission is also assessed. In particular, the GMSL in LRM is derived and then compared with the one measured by Jason-3 GDR-F (Geophysical Data Record-F) in order to verify the continuity between the two missions.

The paper will make use of the main outcomes from (Dinardo et al., 2022) in order to ensure that the altimeter is properly calibrated and characterised during the science processing time.

Naturally, the period around the switch-over between side-A and side-B of the Poseidon-4 altimeter will be covered in order to identify any bias between the two sides or change in behaviour in the measurement stability.

The structure of the paper is briefly described here. Section 2 presents an overview of the architecture of the radar altimeter and its new measurement and calibration modes; Section 3 describes the S6PP prototype with its main design architecture; Section 4 features the LRM S6PP chain processing baseline while the HRM S6PP processing baseline is addressed in Section 5; Section 6 outlines the main results from the Cal/Val and stability analysis of the S6PP LRM

and HRM data; and finally, conclusions are reached in Section 7.

2. Poseidon-4 radar altimeter

2.1. Poseidon-4 radar altimeter architecture and new measurement modes

Poseidon-4 is an electronically redundant dual-frequency radar altimeter with an interleaved chronogram (“open-burst” configuration) in which one echo is received between two transmitted ones and which permits simultaneous operation in LRM and in SAR, as proposed by (Raney, 2012).

This interleaved radar chronogram makes it possible to transmit almost twice as many pulses per radar cycle (20 Hz) compared to the “closed-burst” chronogram used in SAR mode for CryoSat-2 and Sentinel-3 A/B radar altimeter (Gommenginger et al., 2013) and hence to have almost twice as many looks accumulated per 20 Hz measurement. The increase of accumulated looks means an improvement in the precision of the retrieved measurements.

The main measurement frequency is the Ku-Band (13.575 GHz) whereas the C-Band (5.41 GHz) is an auxiliary band used mainly for the ionospheric path delay correction.

The Ku-Band linearly frequency modulated pulses, or chirps, are digitally generated with 320 MHz bandwidth at the carrier frequency and transmitted at a PRF (Pulse Repetition Frequency) which slightly varies with the orbit altitude, and which takes the average value of 9178 Hz (between 9076 and 9280 Hz) at an orbit altitude of 1347 km (1332 to 1362 km). In any case, by instrument design (Raney, 2012) (Phalippou et al., 2012), the Ku-Band pulses are transmitted at a PRF rate which is lower than the Doppler bandwidth. That means that Nyquist’s rate is not fulfilled and hence the received data will be aliased in azimuth with range ambiguities showing up on top of the processed data. This does not represent an issue for the achievement of the mission objectives since several ways to deal with range ambiguities are proposed and developed in section 5.

The altimeter (see Fig. 1) is fully redundant, except for the antenna sub-system, with the two sides (side-A which is the nominal side and side-B which is the redundant side) having an identical chain, which is composed of a Radio-Frequency Unit (RFU) and a Digital Processing Unit (DPU). The two are separated by two redundancy switches (one for Ku-Band and one for C-Band).

The Poseidon-4 digital architecture represents a significant breakthrough with respect to the previous Jason-class altimeters and its design is essentially based on the on board pulse-compression, carried out via a digital “matched-filtering” process (Phalippou et al., 2012) which has replaced the heritage “full-deramping” architecture (MacArthur, 1976). In addition, the gain control loop, to frame the received echo power to the power dynamics of

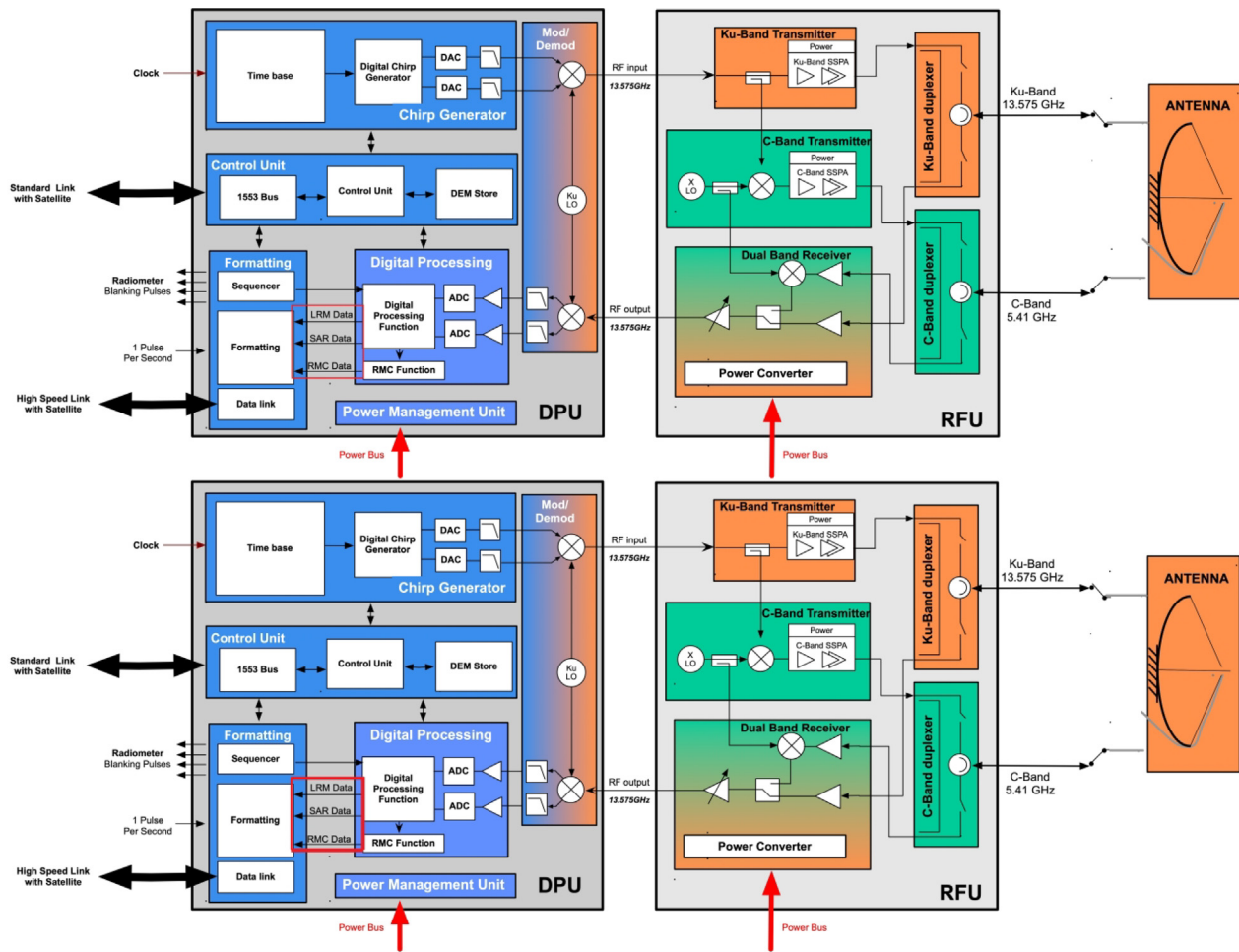


Fig. 1. Poseidon-4 Architecture Block Scheme. In the rectangle outlined in red, the three science data channels can be seen: RMC (I/Q SAR RMC), RAW (I/Q SAR RAW) and Tracking (I2Q2, LRM).

the on board digitiser, is digital, thus not requiring any on ground calibrations or corrections. The RF (Radio-Frequency) attenuators are fixed to a reference step position of 18 dB during the measurement modes. Another unique characteristic of the Poseidon-4 design is the direct analogue modulation/demodulation of the Ku-Band RF signal in base-band and vice versa, which largely simplifies the altimeter design.

As shown in Fig. 1, in output the Poseidon-4 design features three main science data channels:

- I/Q RAW channel (SAR RAW), in Ku- and C-Band (I stands for In-Phase and Q stands for Quadrature).
- I/Q RMC (Range Migration Correction) channel (SAR RMC), in Ku-Band only.
- I2Q2 tracking channel (LRM), in Ku- and C-Band.

The RAW channel delivers I/Q samples (8 bits, 256 range-bins) at each PRF after the range matched-filtering compression, a range swath selection (~ 107 m) and an on board range IFFT (Inverse Fast Fourier Transform).

The RAW telemetry data are formatted in 7 patterns of 1C-64Ku pulses per radar cycle.

The RMC channel delivers I/Q samples (8 bits, 128 range bins) at each PRF after the on board RMC compression (Donlon et al, 2021), which aims at reducing the data rate by a factor of two with respect the I/Q RAW channel and which is subsequently inverted on ground during the science data pre-processing (i.e. prior to the PDP Level-1A stage, EUMETSAT, 2021b).

The RMC telemetry data are formatted in 7 patterns of 64Ku pulses per radar cycle.

Also, the modes RAW and RMC are meant to allow a SAR processing downstream.

The group of 64Ku pulses is usually referred to as a “burst”.

The LRM channel delivers the LRM power (I2Q2) waveform samples (16 bits, 256 range bins) per radar cycle (20 Hz), which have been generated on board to be used by the tracking loop algorithm. In this case, after the range matched-filtering compression and swath selection, the power of successive individual echoes is extracted (power-detection) and incoherently averaged (multi-looking) over 50 ms.

The I/Q data are sampled by the on board digitiser at a frequency of $F_s = 395$ MHz (i.e. the range bins are

separated by 1/395 MHz in time), which is higher than the receiver's useful bandwidth ($BW = 320$ MHz). Thus, the range bin sampling is $c_0/2F_s$, whereas the range resolution is $c_0/2BW$ where c_0 is the speed of light.

Poseidon-4 can provide in output various telemetries from the above-mentioned science data channels according to specific predefined combinations, referred to as “measurement modes”:

- the telemetries from the three science channels are commanded to be available at the same time (and this measurement mode is known as “LX2”).
- only the telemetries from the RAW and tracking channel are commanded to be available at the same time (“LX” measurement mode).
- only the telemetries from RMC and tracking channel are commanded to be available at the same time (“LRMC” measurement mode).
- only the telemetries from tracking channel are commanded to be available (“LRM” measurement mode).

For limitations in the on board storage and maximum value of transmission and reception data rate between satellite and ground stations, the S6-MF cannot provide global coverage in “LX”, so compromises have to be made.

For this purpose, a zone mask, commanding the measurement mode in which Poseidon-4 will be operated according to its geographical position, is defined in the instrument operation plan and it followed a specific calendar during the commissioning time (EUMETSAT, 2019). Since the end of the commissioning time, “LRMC” measurement mode is commanded nearly globally.

Finally, the Poseidon-4 altimeter design features a special tracking mode in the measurement mode called the Open Loop Tracking Command (OLTC) which allows the sensor to maintain stable tracking control over complex topographic surfaces such as coastal and inland waters via an on board digital elevation model (around 9 Megabytes), which stores a coarse height of the overflowed surface. For S6-MF, the OLTC is fully uncompressed allowing a sampling of elevation each 0.01° along-track over the 127 orbits constituting a cycle.

The heritage tracking mode in which the sensor autonomously and internally commands the tracking control of the surface without the support of any external information is referred to as “closed-loop”.

The Open-Loop tracking mode is not available when using the “LX2” measurement mode.

2.2. Poseidon-4 radar altimeter new internal calibration modes

The scope of the altimeter internal calibrations is to monitor the long-term stability of the internal path of the sensor, to survey its instrumental ageing and performances, to characterise the intra-orbital thermal response of the instrument and to estimate the calibration parameters

and tables necessary to calibrate the sensor during the science data processing.

Two main classes of internal calibrations are distinguished for Poseidon-4:

- CAL-1: in this type of calibration, the instrument response to a radar impulse (Point Target Response or PTR, also known as Impulse Response or IR) is measured by looping back the transmit chain with the receive chain through the duplexer's calibration path (i.e. the antenna is by passed). This is an active calibration mode type.
- CAL-2: in this type of calibration, the instrument response to the thermal noise (TNR, Thermal Noise Response or Receiver Transfer Function) is measured inside the receiving window. This is a passive calibration mode (i.e. no impulse generated by the DPU is received in this calibration mode).

The Poseidon-4 features the following specific CAL-1 and CAL-2 calibration modes:

- CAL-1 SAR: the telemetries are from the altimeter RAW channel. The PTR is generated on ground from the downlinked I/Q data in Ku- and C-Band.
- CAL-1 LRM: the telemetries are from the altimeter I2Q2 tracking channel. The PTR is generated directly on board by the instrument in Ku- and C-Band.
- CAL-1 INSTR (INSTRument): the telemetries are from the altimeter INSTR channel. The PTR and chirp are generated on ground from the downlinked I/Q data in Ku- and C-Band.
- CAL-1 RMC: the telemetries are from the altimeter RMC channel. The PTR is generated directly on board by the instrument in Ku-Band.
- CAL-1 ECHO CAL: the telemetries are from the altimeter RAW channel. The PTR is generated on ground from the downlinked I/Q data in Ku-Band only.
- CAL-2: the telemetries are from the altimeter RAW channel. The TNR is generated on ground from the downlinked I/Q data in Ku and C-Band.

The ideal output of CAL-1 is a squared sinc function. The ideal output of CAL-2 is white noise.

In the case of ECHO CAL, the CAL-1 calibration is directly embedded in the tracking cycle (i.e. is executed continuously during the measurement mode) and provided in the SAR RAW/RMC science telemetries at a configurable posting rate. This was set during commissioning to 10 Hz. Its main purpose is to calibrate most of the intra-orbital thermal-induced variation of the range PTR which would otherwise impact the science measurements if not calibrated out.

The other CAL-1 and CAL-2 calibrations are executed “on demand” out of the measurement mode, commanding the uplink of a dedicated tele-command to the instrument.

CAL-1 INSTR is a special CAL-1 calibration mode which is executed just after the base-band signal's digitation and prior to the matched-filtering: by means of this calibration mode, the transmitted signal (i.e. the digital chirp) can be measured and characterised on ground. Further details about Poseidon-4 calibrations and performances can be found in (Dinardo et al. 2022).

The calibration parameters computed from the CAL-1 PTR and which are routinely monitored are usually represented by:

- the internal path delay and the internal path power of the PTR.
- the 3-dB main-lobe width of the PTR and main-lobe width degradation with respect to the squared sinc ideal case.
- the powers and positions of the first ten left- and right-hand side-lobes with respect to the squared sinc ideal case.
- the powers and positions of the ten first left-hand side-lobes with respect to the ten first right-hand side-lobes.

The CAL-1 SAR mode also allows the calculation of calibration tables, such as AUTO-ATT (AUTO-ATTenuation) tables, AUTO-PRI (AUTO-Pulse Repetition Interval) tables, and intra-burst correction tables that characterise the PTR when changing one specific instrument parameter (RF attenuation steps of the gain control loop, pulse repetition interval, and the number of the burst pulse in the received burst, respectively). In particular, the intra-burst correction tables represent the amplitude and phase corrections that should be applied at the burst level in order to compensate for the measured distortions along the burst pulses.

The calibration parameters computed from the CAL-2 TNR and which are routinely monitored are usually represented by:

- the CAL-2 TNR power over three short windows used to determine the occurrence or the degradation of spikes or spurious signals at the beginning, in the middle and at the end of the CAL-2 TNR.
- the difference between the max and min values (ripple) for each side of the TNR.
- the mean power, slope, and standard deviation for each side of the TNR.

The CAL-1 and CAL-2 routine monitoring from the beginning of the mission is referred to as long-term monitoring (LTM).

3. Sentinel-6 processor prototype

S6PP is a multi-chain (LRM, UF-SAR, fully-focused SAR) processing suite able to process Sentinel-6 Level-1A (L1A) and Level-1B (L1B) data products up to Level 2 (L2). It can also process transponder data in a dedicated

processing mode. The fully focused SAR processing mode will not be addressed in this paper, but readers may refer to (Egido & Smith, 2017) for more information.

The innovative algorithms developed in the CNES/CLS research and development activities are implemented in S6PP and validated in support to the different thematic applications (in particular inland water and ocean) and in view of promoting them for a possible implementation in an operational ground segment context such as the EUMETSAT PDAP centre.

S6PP has a strong heritage from the CLS/CNES SMAP (Standalone Multi-mission Altimetry Processor) processor (<https://gitlab.cnes.fr/rieup/smap>).

Furthermore, once developed, the S6PP application was deployed on the CNES HPC (High Performance Computing) cluster for a computationally gridded data production.

Given the reported variation of the payload in-orbit temperatures along with a payload instrumental ageing stronger than that observed for pulse-limited Jason-class altimeters (Dinardo et al., 2022) and given the aforementioned tight requirement to measure the GMSL in seamless continuity with Jason-3 with an error lower than 1 mm/year, the clear goal for S6PP was to process the S6-MF data with minimum possible level of approximations along the processing chain but still maintaining an extremely efficient prototype from the computational point of view.

Therefore, for this purpose, novel algorithms have been developed and implemented within the S6PP LRM chain (which is the heritage pulse-limited altimetry mode), such as:

- o Possibility to retrack the LRM waveform built on board (LRM I2Q2) or the one built on ground from HRM RAW/RMC L1A data products. This is part of the L1B chain.
- o LRM physics-based (frequency domain) waveform model (Buchhaupt et al., 2018) with possibility to set as input the ocean topography skewness coefficient. This is part of the L2 chain.
- o Numerical LRM waveform retracking scheme based on an in-flight PTR or on an ideal PTR (squared sinc) interface. This is part of the L2 chain.

and in the S6PP HRM chain as:

- o Beam-forming carried out by Chirp Zeta-Transform (CZT) (Oppenheim and Schaffer, 1975), (Rieu et al., 2020) in the approximate beam-steering (ABS) configuration in order to correct for the Range Walk (RW) effect (Moreau et al. 2017, Scagliola et al., 2021) with only a limited increment of computational cost estimated around 10%. This is part of the L1B chain.
- o Possibility of using different multi-looking number in building the UF-SAR waveform in order to be less affected by ocean surface motion effects such as wave orbital velocity (Boisot et al. 2016, Reale et al. 2020, Buchhaupt, 2019). This is part of the L1B chain.

- o Posting rate of the UF-SAR waveforms at the standard 20 Hz rate or higher (Dinardo et al., 2013; Egido et al., 2021a; Rieu et al. 2021). This is part of the L1B chain.
- o UF-SAR physics-based (frequency domain) waveform model (Buchhaupt et al., 2018) with possibility to set as input the topography ocean skewness coefficient. This is part of the L2 chain.
- o Numerical UF-SAR waveform retracking scheme based on an in-flight PTR or on an ideal PTR (squared sinc) interface. This is part of the L2 chain.
- o Delay-Doppler Map (DDM) ambiguities natively modelled in the UF-SAR waveform model (Dinardo et al., 2020b). This is part of the L2 chain.

All the S6-MF Poseidon-4 data from beginning of tandem phase (18 December 2020) to December 2021 in STC/NTC LRM and STC HRM data flavours have been processed by the S6PP processor up to Level 2. In both modes, the orbits can be swapped in post-processing to the JPL ones.

As it stands now, S6PP can only process Ku-Band data from the Poseidon-4 radar altimeter. Consequently, the C-Band data will not be processed in this work, but the ionospheric correction will be the one relative to the Jason-3 mission during the tandem phase period analyzed in this paper.

The wet tropospheric correction (WTC) and the atmospheric attenuation correction instead can be that measured by AMR-C radiometer or, alternatively, the one provided by the ECMWF model. The Sea State Bias (SSB) solution will be the one computed from Jason-3 Ku-Band SSB table with input SWH and wind speed from S6PP.

The S6PP LRM and HRM L2 data products are formatted in a standard NetCDF-4 (Network Common Data Format-4) data format and ingested routinely in the CLS Cal/Val (Calibration/Validation) database tables.

4. LRM S6PP chain processing baseline

4.1. L1B LRM processing baseline

In this subsection, we are going to describe the main processing algorithms which are part of the LRM L1B processing baseline.

The S6PP can retrack LRM waveforms originating from the three science data channels:

- From I2Q2 tracking channel in Ku-Band.
- From I/Q RAW channel in Ku-Band.
- From I/Q RMC channel in Ku-Band.

The reason to generate a LRM waveform on ground from the RAW and RMC channels data comes from the need to build the LRM waveform by decimating the individual echoes in the radar cycle at the same PRF as Jason-3 (2060 Hz). This can then be used to demonstrate

whether the high PRF used on board by Poseidon-4 to build the LRM waveform may give rise to any systematic bias on the geophysical measurements with respect to the case in which a heritage PRF of 2 kHz is used. The Pulse-to-pulse correlation effect on the geophysical parameter estimation has been analysed on Cryosat-2 data using various PRF for LRM echoes reconstruction (Egido and Smith, 2019). Comparisons to the standard 2 kHz PRF have shown that additional biases were introduced in SSH and SWH estimations using higher PRF.

As part of the S6-MF MPWG (Mission Performance Working Group), an analysis was performed by CNES showing the impact when decimating the individual echoes at lower pulse repetition frequencies. Specifically, to perform this analysis, we retracked LRM waveforms built with different PRF values: 9 kHz, 4 kHz, and 2 kHz. In our analysis, only RAW data have been selected in order to reproduce exactly the on board LRM waveform behaviour. The different acquisitions in RAW mode covered various sea state conditions so as to detect an eventual SWH dependency as expected and shown in (Egido and Smith 2019). In order to build the LRM waveform on ground based on a PRF of ~ 4 kHz and ~ 2 kHz, these individual RAW echoes (acquired at 9 kHz during the radar cycle) are decimated (one every two echoes and one every four echoes, respectively), range-compressed and then incoherently averaged. The LRM waveform based on a PRF of 9 kHz is built without any decimation. To build the LRM waveform, it is sufficient to carry out a simple incoherent summation of the individual echoes since these individual echoes have been already aligned on board for the orbit variation inside the radar cycle.

After retracking these LRM waveforms based on a PRF of ~ 9 kHz, ~ 4 kHz, ~ 2 kHz, we found that the impacts (see Fig. 2) in term of bias are at millimetric level for SSH and at centimetric level for SWH. Results differ from a similar study of Egido and Smith (2019) as this latter analysis was carried out using CryoSat-2 data whose acquisition scheme is considered to not be representative of the POS-4 one. Cryosat-2 altimeter (SIRAL-2, Synthetic Interferometric Radar Altimeter-2) operates in a closed-burst configuration (a new burst is transmitted only after the previous burst is received) while POS-4 operates in a continuous emission/reception interleaved mode. Then, compared to the CryoSat-2 altimeter case, the number of individual echoes in the POS-4 radar cycle is significantly higher on POS-4 side (448 pulses at 9 kHz). In particular, while the number of uncorrelated pulses for SIRAL-2 is only around 32, on POS-4 case the number of statistically independent looks is large enough to allow a speckle noise reduction by an incoherent averaging. This may explain why for POS-4 there is a smaller pulse-to-pulse bias between the 2 kHz and 9 kHz geophysical parameter estimations compared to the CryoSat-2 altimeter case.

This detected millimetric pulse-to-pulse range bias may be corrected *a posteriori* through a post-processing look-up table based on the curve in Fig. 2-left.

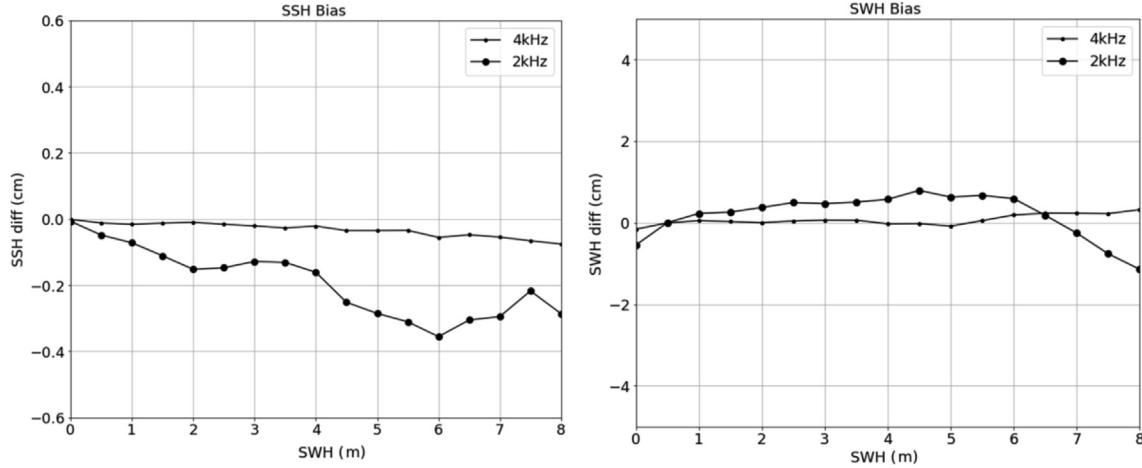


Fig. 2. SSH (left) and SWH (right) difference between the dataset “9 kHz” and the dataset “4 kHz” and “2 kHz” (CNES courtesy).

Furthermore, as expected, the noise is reduced in SSH and SWH whatever the SWH regime. In particular, a significant improvement of between 10% and 15 % at high sea state regimes (SWH greater than 5 m) is observed for the SSH and SWH noise level.

Moreover, it has been observed that whereas the LRM waveform built on board by the I2Q2 tracking channel is almost perfectly in line with the one reconstructed on ground from the I/Q RAW channel data, this is not the case when the LRM waveform is reconstructed on ground from the I/Q RMC channel. For this latter case, as shown in Fig. 3, a distortion of the waveform’s leading edge is mainly observed, which is considered to be linked to a quantisation effect arising from the I/Q data formatting in 8 bits as performed at the end of the RMC on board compression.

Given the above results, it has been decided, as the nominal LRM processing baseline, to retrack the LRM waveforms built on board by the I2Q2 tracking channel. These waveforms are retrieved from the PDP L1B LRM data products.

4.2. L2 LRM processing baseline

In this subsection, we are going to describe the main processing algorithms which are part of the LRM L2 processing baseline.

In order to be as much in line as the PDAP LRM L2 measurements estimated by the MLE-4 (Maximum Likelihood Estimator-4) retracker (Amarouche et al., 2004), it has been decided to retrack four geophysical parameters: epoch t_0 , significant wave-height SWH, waveform amplitude P_u and antenna squared mis-pointing ξ^2 . For the LRM waveform model, we use the model proposed by (Buchhaupt et al., 2018) which provides a model’s analytical formulation in the frequency domain which is then converted in the time domain by an IFFT operation. In particular, in the case of a circular antenna pattern as for

S6-MF, the Flat Sea Surface impulsive Response (FSSR) Fourier transform can be rewritten as:

$$FSSR(f) = \frac{1}{\left[2\pi j \cdot f + \frac{c_0}{H \cdot \alpha_{Earth}} \cdot \left(\frac{4}{\gamma} + \nu\right)\right]} \cdot \exp\left[\frac{-\frac{4}{\gamma} \xi^2 \left(2\pi j \cdot f + \frac{\nu \cdot c_0}{H \cdot \alpha_{Earth}}\right)}{2\pi j \cdot f + \frac{c_0}{H \cdot \alpha_{Earth}} \cdot \left(\frac{4}{\gamma} + \nu\right)}\right] \quad (1)$$

With:

$$\begin{cases} \Delta\theta_{3dB} = \sqrt{\Delta\theta_{x_{3dB}} \cdot \Delta\theta_{y_{3dB}}} \\ \gamma = \frac{\sin^2(\Delta\theta_{3dB})}{2 \cdot \ln(2)} \\ \alpha_{Earth} = \left(1 + \frac{H}{R_{Earth}}\right) \end{cases} \quad (2)$$

The model has been computed using a spectral oversampling factor of 6 in the frequency domain since for this value the approximation error is reported to be less than 10^{-3} in (Buchhaupt et al., 2018).

The LRM waveform model in (Buchhaupt et al., 2018) has been expanded in order to include, in its mathematical formulation, the skewness coefficient λ_s in the ocean topography PDF (Probability Density Function) model. This expansion is necessary in order to adopt the same ocean topography PDF model in our processing as the one used by heritage in the Jason missions.

We use this classic definition of the ocean topography PDF (Hayne and Hancock, 1982) which represents a skewed Gaussian function:

$$PDF(z) = \frac{1}{\sqrt{2\pi}\sigma_z} e^{-\frac{z^2}{2\sigma_z^2}} \left\{1 + \frac{\lambda_s}{6} (\zeta^3 - 3\zeta)\right\} \quad (3)$$

$$\zeta = \frac{z - z_0}{\sigma_z}, \sigma_z = \frac{SWH}{4}$$

where σ_z is the ocean surface roughness, λ_s is the ocean skewness coefficient, and $z - z_0$ is the sea surface elevation with respect to z_0 which is the mean sea surface elevation.

Making the Fourier transform of (3) analytically and after some cumbersome calculations, the expression of

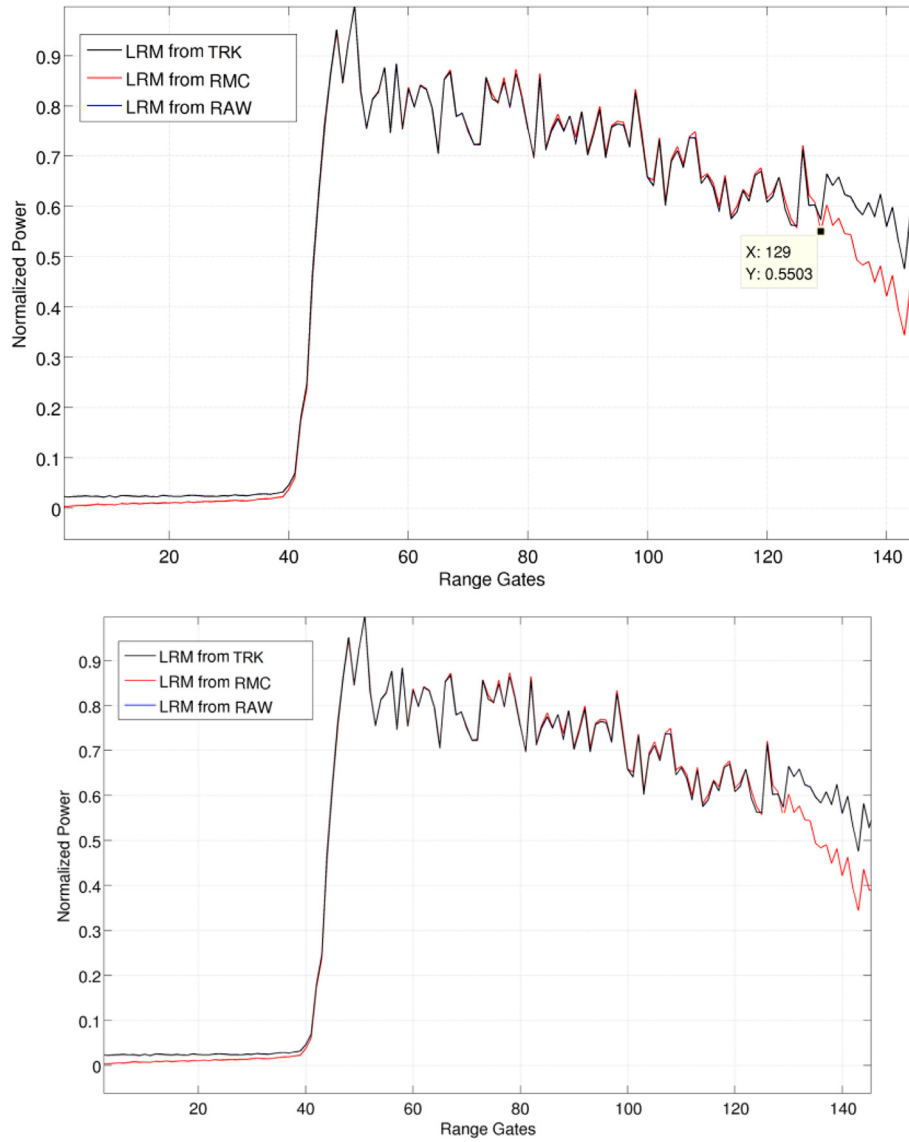


Fig. 3. An example of LRM waveform built from the I2Q2 tracking channel (black curve), from the RMC channel (red curve) and from the RAW channel (blue curve) when using LX2 measurement mode.

the Fourier transform of the skewed gaussian PDF in equation (3) is found to be given by:

$$PDF(\omega_z) = e^{-j\omega_z z_0} e^{-\frac{\zeta^2}{2}} \left\{ 1 + j \frac{\lambda_s}{6} \zeta^3 \right\} \quad (4)$$

$$\zeta = \omega_z \sigma_z$$

Applying the following equations to convert the sea surface elevation into the radar return time:

$$\begin{cases} t - t_0 = -\frac{2(z-z_0)}{c_0} \\ \sigma_t = \frac{2\sigma_z}{c_0} \\ \omega = 2\pi f = -\frac{c_0 \omega_z}{2} \end{cases} \quad (5)$$

the Eq. (4) becomes:

$$PDF(\omega) = e^{-j\omega t_0} e^{-\frac{\zeta^2}{2}} \left\{ 1 - j \frac{\lambda_s}{6} \zeta^3 \right\} \quad (6)$$

$$\zeta = \omega \sigma_t = 2\pi f \sigma_t$$

In case $\lambda_s = 0$, we find the same expression as in (Buchhaupt et al., 2018). The fact that we know the analytical expression of the PDF Fourier transform allows us to avoid computing the FFT (Fast Fourier Transform) of the PDF given in (3) at each retracking iteration step and hence to be more computationally efficient.

As skewness coefficient, a Jason-heritage value of +0.1 is used.

In general, if the PDF is given in a more general formulation, (see for instance (Hayne, 1980) and (Lipa, and Barrick, 1981)) as:

$$PDF(z) = \frac{1}{\sqrt{2\pi}\sigma_z} e^{-\frac{z^2}{2\sigma_z^2}} \left\{ 1 - \frac{\gamma}{2} He_1(\zeta) + \frac{\lambda_s}{6} He_3(\zeta) + \frac{k_s}{24} He_4(\zeta) + \frac{\lambda_s^2}{72} He_6(\zeta) \right\} \quad (7)$$

$$\zeta = \frac{z-z_0}{\sigma_z}, \sigma_z = \frac{SWH}{4}$$

where γ is the cross-skewness coefficient (describing the correlation between the elevation and square of the slope and responsible for the electro-magnetic sea state bias), k_s is the

kurtosis coefficient and $He_n(\zeta)$ is the n-th degree Hermite polynomial, its Fourier transform is given by:

$$PDF(\omega) = e^{-j\omega t_0} e^{-\frac{\zeta^2}{2}} \left\{ 1 - j\frac{\lambda_s}{2}\zeta - j\frac{\lambda_s}{6}\zeta^3 + \frac{k_s}{24}\zeta^4 - \frac{\lambda_s^2}{72}\zeta^6 \right\} \quad (8)$$

$$\zeta = \frac{z-z_0}{\sigma_z}, \sigma_z = \frac{SWH}{4}$$

In the LRM retracking scheme, we discard any statistical moments higher than the skewness λ_s . In addition, defining $\text{sign}(x)$ as the sign function, we introduce in equation (9) the term $\text{sign}(\sigma_t)$ in the argument of the exponential term in order to allow the estimation of negative SWH in the retracking scheme, as is usually done in the SAMOSA retracking (see for instance [Dinardo, 2020a](#) at equation 3.13) or in the frequency domain retracker ([Buchhaupt et al., 2018](#)). The final $PDF(\omega)$, which is used in the LRM retracking scheme, is therefore given by:

$$PDF(\omega) = e^{-j\omega t_0} e^{-\frac{\text{sign}(\sigma_t)\zeta^2}{2}} \left\{ 1 - j\frac{\lambda_s}{6}\zeta^3 \right\} \quad (9)$$

$$\zeta = \omega\sigma_t = 2\pi f\sigma_t$$

The same PDF formulation given by (9) is used for the HRM chain in [section 5](#).

The second significant innovation in the retracking scheme is the interface with the in-flight PTR.

Given the low geographical variations of the internal path delay along the pass (as reported in [Dinardo et al., 2022](#)) and in order to be as computationally efficient as possible, it has been decided to use as in-flight PTR the one from CAL-1 SAR RAW calibration mode (commanded three times per day). In this case, only one CAL-1 SAR RAW PTR is used per pass: the one closest in time to the pass central time.

The CAL-1 SAR RAW data are processed routinely from the PDP L0 data products on the CNES HPC cluster, and the PTR samples are stored in database tables.

For each pass, the closest CAL-1 SAR RAW PTR is fetched from this in-house database and is transformed to the frequency domain by a FFT.

In order to assess the temporal stability of the PDP LTM applied calibration parameters, the LRM retracking scheme can also use as PTR the ideal impulse response (that is a squared sinc) and in this case the internal path delay and total power reported in the PDP L1B LRM data products are used for calibrations.

The Fourier transform of a squared sinc centred at instant t_0 is given by:

$$\text{sinc}^2[BW(t - t_0)] \xrightarrow{\mathcal{F.T.}} \frac{1}{BW} \left[\Delta\left(\frac{f}{BW}\right) \right] e^{-j2\pi f t_0} \quad (10)$$

where Δ represent the triangular function defined as:

$$\Delta\left(\frac{f}{BW}\right) = \begin{cases} 1 - \frac{|f|}{BW} & |f| \leq BW \\ 0 & |f| > BW \end{cases} \quad (11)$$

Since the Fourier transform of a real-value signal is conjugate-symmetric (Hermitian property, see [Oppenheim and Schaffer, 1975](#)), the magnitude of the PTR spectrum

is even-symmetric whereas the phase is odd-symmetric. Given these symmetry properties, we can restrict our PTR spectrum to only non-negative frequencies and consequently reduce the computational complexity by a factor of two.

The non-negative frequency spectrum's magnitude and phase are then linearly oversampled by a factor of 6 (which is the chosen spectrum oversampling factor) after the spectrum generation.

The oversampling may be even achieved by symmetrically zero-padding the PTR prior the spectrum generation via FFT.

In [Fig. 4](#), an example of spectrum magnitude and phase is shown for an in-flight PTR (CAL-1 SAR RAW) for the non-negative frequencies side. As expected, the spectrum magnitude is a leg of the triangular function: the inverse of the slope of this leg (`mag_slope`) is proportional to the chirp bandwidth by the formula:

$$BW = -\frac{1}{\text{mag_slope}} \quad (12)$$

Also as expected, the spectrum phase is a linear ramp: the slope of the ramp (`phase_slope`) returns the time shift of the PTR by the formula:

$$t_0 = -\frac{\text{phase_slope}}{2\pi} \quad (13)$$

The benefits of proposed in-flight approach is:

- o We can get rid of any Look-Up Tables (LUT) which are typically used inside the heritage MLE-4 retracker ([Amarouche et al., 2004](#)), ([Thibaut et al., 2004](#)).
- o We can get rid of any empirical methods which are typically used to compute the PTR internal path delay as centre of gravity, half-power or peak-power methods.
- o There is no need to recentre the PTR as in ([Poisson et al. 2018](#)) but the PTR is injected in the model “as-is”.
- o We can calibrate the altimeter perfectly in range, power and bandwidth since the full PTR is used in the waveform model generation.
- o As the model is computed analytically in the frequency domain and then transformed in the time domain by one simple IFFT operation, the computational complexity of the model is expected to be very low.

For the antenna irradiation pattern characterisation, it has been decided to use an antenna pattern beamwidth of 1.34° (both in the along and across track direction), which is 0.01° different from the value found in ([Dinardo et al. 2022](#)) but still inside the antenna post-measurement uncertainty.

Clearly, the same value will be used in the HRM chain.

Given the different default tracking gates for Jason-3 and S6-MF altimeter (44 and 50, respectively) and given the different range bin sampling (the sampling frequency is 320 MHz for Jason-3 and is 395 MHz for S6-MF), the S6-MF window needs to start from gate 2 and to end at

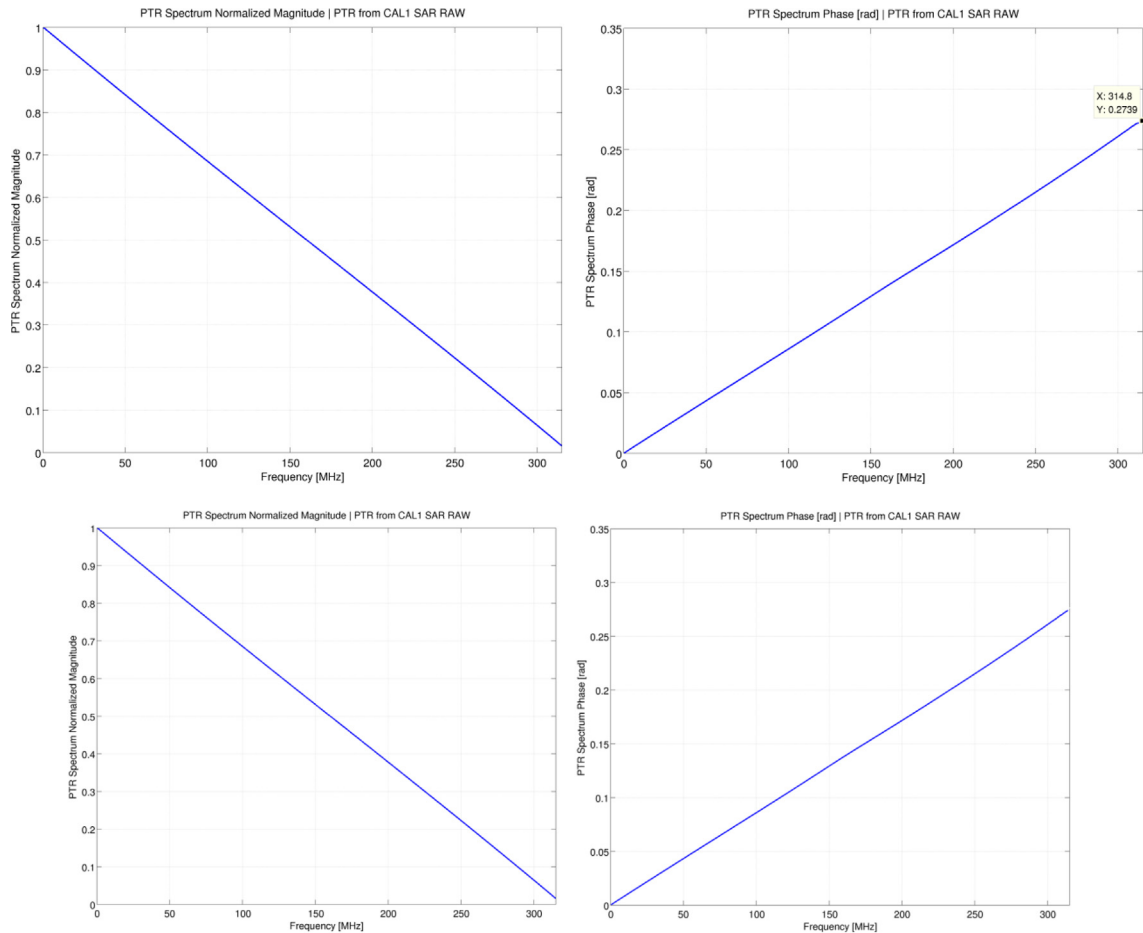


Fig. 4. Normalised magnitude spectrum (left) and phase spectrum (right) of one in-flight PTR (CAL-1 SAR RAW).

gate 140 in order to fit as closely as possible to the Jason-3 12 to 114 gate window size in metre. With these values, the size of the range window in metre after the default tracking gate value is about the same between Jason-3 and S6-MF. These values are the same used by the PDP version 3.4.2.

The thermal noise, which we have used in the waveform model, is simply given by the mean of the waveform's gates on the window interval $[2 \rightarrow 12]$. These values are the same as those used by the PDP version 3.4.2.

The CAL-2 TNR is not applied to calibrate the LRM waveform, following the outcome reported in (Dinardo et al., 2022).

To retrieve the range at 1 Hz, the PDP approach is applied to the 20 Hz S6PP data. As for Jason-3 (J3) data, the compression method from 20 Hz to 1 Hz range uses a linear regression based on the minimisation of the absolute deviation. However, contrary to J3 or other missions, the compression step is not applied to the 20 Hz range but to the 20 Hz range minus the 20 Hz altitude. This new approach allows better accounting for numerical instabilities and higher order effects, and also the reduction of the potential pseudo-time tag bias errors introduced by the compression. This method was analysed on J3 data and

validated during the preliminary PDP developments. The residual differences between SSH and range-compression are negligible: differences ranging between -4 mm and 4 mm and centred in zero, with the strongest differences localised on the low radial speed and high latitude (with a bias lower than 1 mm for lowest altitude rate).

The SWH compression from 20 Hz to 1 Hz is carried out by a direct averaging of the 20 Hz SWH. The heritage method of sigma-composite compression, as done in J3, is no longer possible with the S6PP numerical retracking as sigma-composite is a parameter linked to the Gaussian approximation of the PTR. However, both methods of compression were compared, as Jason-3 uses the sigma-composite compression method. J3 and S6PP SWH are very consistent between each other and only in the case of low SWH regimes (i.e. SWH less than 1 m), we observe appreciable differences between them. A possible explanation of this discrepancy between J3 and S6PP at these low SWH may arise from how the compression manages the low SWH. On the S6PP side, the negative SWH are estimated from the S6PP retracker and considered valid 20 Hz measurements in the compression. This method differs from the heritage sigma-composite processing strategy

(in which the negative SWH are not allowed). Comparison between the two methods shows differences larger than 5 cm for the SWH lower than 1 m.

The sigma-nought compression from 20 Hz to 1 Hz is carried out by a direct averaging of the 20 Hz sigma-nought.

Finally, the fitting scheme used inside the LRM retracking is a standard Levenberg-Marquardt least-squares algorithm with four fitting parameters: epoch, significant waveheight, amplitude, waveform squared mis-pointing.

In conclusion, the LRM processing baseline is summarised in Table 1:

With regard to the computational time, the LRM numerical retracker implemented in S6PP is typically twice as fast as real-time for a single thread of execution.

Using CNES cluster's high computing capabilities, one year of S6-MF LRM data products can be retracked in only a few hours.

5. HRM S6PP chain processing baseline

5.1. LIB HRM processing baseline

In this subsection, we are going to describe the main processing algorithms which are part of the HRM (or UF-SAR) LIB processing baseline. The main HRM LIB processing algorithms are summarised in Table 3.

A UF-SAR processing chain in the form of a Delay-Doppler algorithm (Raney, 1998) is implemented. The input data are the PDP L1A data products. The flow-chart of the Delay-Doppler algorithm is shown in Fig. 5 and consists in the following stages:

a) Calibration

After being extracted from L1A data products, the burst echoes need to be calibrated and corrected by all the sensor's instrumental artefacts. Aside from the heritage

Table 1
LRM Processing Baseline.

LRM Processing Baseline	Value
Input data product	Ku-Band I2Q2 tracking channel data provided by the PDP LRM L1B data products (STC and NTC latency)
Waveform model	numerical frequency domain with oversampling factor of 6
In-flight PTR	from CAL-1 SAR RAW
Fitting scheme	Levenberg-Marquardt least-squares with four unknowns
Antenna pattern beamwidth	1.34°
Retracking window size	[2 → 140]
Thermal noise interval	[2 → 12]
CAL-2 TNR	non-applied
Skewness coefficient	+0.1
Negative SWH	allowed
1 Hz compression	direct approach

CAL-1 and CAL-2 calibrations, two special calibrations, which are the intra-burst phase and amplitude calibration defined in section 2.2, are dedicated to SAR mode. Their scope is to calibrate any variation in phase and amplitude between the pulses within each burst.

b) Ground-Cell Gridding

The purpose of this stage is to identify a set of surface locations (or surface samples or ground-cells) along the overflown surface elevation profile wherein the synthesised Doppler beams will be later focused, steered and incoherently accumulated. This grid step is usually set at around 20 Hz (given by the size of the Doppler beam footprint) but a higher posting rate, as such 80 Hz or 140 Hz, can be experimented.

c) Beam-Steering and Beam-Forming

The purpose of this stage is to synthesise and focus a set of 64 Doppler beams per burst, exploiting the Doppler effect due to the satellite motion with respect to the ground. For each burst, an FFT is usually performed on the burst data in the along-track direction (this is the “beam-forming”). In this section, we demonstrate that better focusing for the off-nadir beams can be achieved by Chirp Zeta-Transform. After the beam-forming, a steering of the Doppler beams is carried out so that the 64 Doppler beam footprints are perfectly co-located with the 64 surface sample locations in view by the current burst (this is the “Beam-Steering”). This steering can be of two types: approximate or exact.

In the Approximate Beam-Steering (ABS), all the Doppler beams will be steered by the same angle and thus only the Doppler central beam will be exactly co-located with the own closest surface sample location. In the Exact Beam-Steering (EBS), each of the Doppler beams will be steered by a different angle. As a result, each Doppler beam (e.g. not only the central Doppler beam) will now be co-located exactly with the own closest surface sample location. In this configuration, each Doppler beam can be focused by an FFT (i.e. a total of 64 FFT are made) or by a DFT (Discrete Fourier Transform).

d) Beam-Stacking

The purpose of this stage is to collect in one matrix of data (referred to as a “stack”) all the Doppler beams that are pointing to exactly the same surface sample location. These Doppler beams in the stack stare at the same surface location from different burst centre positions (i.e. from different look angles).

e) Range-Alignment and Range-Compression

The purpose of this stage is to correct all the misalignments in range between the beams of the same stack. Three

Table 2

Level of the first five side-lobes on the left and right side of the azimuth PTR in the case of the ABS + CZT, EBS + 64FFT, ABS + FFT beam-forming and squared sinc.

Azimuth PTR	First Side-lobe [dB]	Second Side-lobe [dB]	Third Side-lobe [dB]	Fourth Side-lobe [dB]	Fifth Side-lobe [dB]
ABS + CZT (PTR left side)	-13.25	-17.70	-20.69	-22.91	-24.83
ABS + CZT (PTR right side)	-13.27	-17.77	-20.72	-23.15	-24.61
EBS + 64FFT (PTR left side)	-13.23	-17.77	-20.64	-22.81	-24.65
EBS + 64FFT (PTR right side)	-13.29	-17.78	-20.72	-23.15	-24.63
ABS + FFT (PTR left side)	-13.54	-17.97	-20.95	-23.17	-25.04
ABS + FFT (PTR right side)	-13.59	-18.06	-20.99	-23.40	-24.84
SINC**2 (PTR left side)	-13.27	-17.81	-20.75	-22.91	-24.63
SINC*2 (PTR right side)	-13.27	-17.81	-20.75	-22.91	-24.63

Table 3

L1B UF-SAR Processing Baseline.

L1B HRM Processing Baseline	Value
Input data products	PDP L1A data products (STC latency)
UF-SAR algorithm	Delay-Doppler
Beam-forming	ABS + CZT
Surface gridding	20 Hz
Multi-looking number (or stack size)	448
Zero-padding (range)	2
CAL-2 TNR	non-applied
Burst table corrections	non-applied

Table 4

L2 UF-SAR Processing Baseline.

L2 UF-SAR Processing Baseline	Value
Input data products	S6PP L1B data products
Waveform model	numerical frequency domain with oversampling factor of 4
Ambiguity treatment	ambiguities not masked-out
In-flight PTR	from CAL-1 SAR RAW
Beam sub-sampling	3 out of 7
Fitting scheme	Levenberg-Marquardt least-squares with three unknowns
Antenna pattern beamwidth	1.34°
Skewness coefficient	0.1
Retracking window size	[10 → 132]
Thermal noise interval	[12 → 16]
Platform mis-pointing	constant for roll: -0.03° constant for pitch: -0.005°
Negative SWH	allowed
1 Hz compression	direct approach

range corrections need to be operated: slant range correction, tracker range correction and Doppler range correction. After the range-alignment, the stack matrix is pulse-compressed in the range dimension. The range-

compression is implemented as a simple FFT. After the FFT, the signal is square-law detected (i.e. the power is extracted).

Usually, prior to the range-compression, the Doppler beams can be zero-padded in range by a factor of two, thereby doubling their extension. The effect is to oversample the range-compressed signal by a factor of 2. After the range-compression, the Doppler beams are referred to as “looks” since now they are a statistically independent “look” of the same surface location.

f) Multi-Looking

This multi-looking is simply the incoherent summation in the along-track direction of the square-law detected range-compressed Doppler beams in the stack. The scope of the multi-looking is to knock down the speckle noise, accumulating statistically independent looks of the same measurement. The final result of the multi-looking is the generation of a single SAR return power waveform. This waveform is usually referred to as unfocused SAR waveform since it has been focused in azimuth dimension, exploiting only a fraction of the full available synthetic aperture length. This fraction is the duration of the burst. Some looks in the stack can be discarded out of the multi-looking summation by a look angle thresholding. In the case of the S6PP L1B HRM chain, this number of looks has been set to 448.

For more information, the reader is invited to consult several publications on the subject, as such (ESA, 2013) (Gommenginger et al., 2013), (Wingham et al., 2004), (Dinardo, 2020).

In the case of S6-MF, the L1A I/Q data can be from the RAW or RMC Poseidon-4 data channel according to the zone mask in use.

In the case of the RMC data stream, the on board RMC compression is inverted on ground prior to the PDP L1A

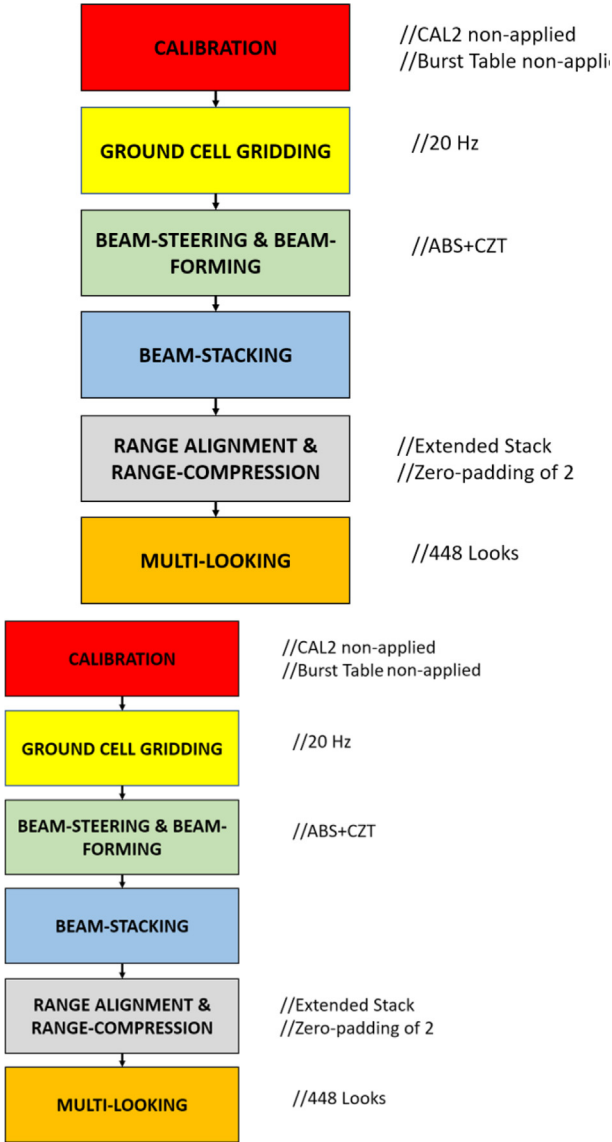


Fig. 5. Delay-Doppler algorithm as applied to the PDP L1A data products.

stage (EUMETSAT, 2021b). In both cases (RAW and RMC), the applied Delay-Doppler processing within S6PP can therefore be the same.

Following the reported impact in term of range stability from the omission of the range walk correction for Sentinel-3A STM (Surface Topography Mission) mission (Aublanc et al, 2020), the range walk correction was deemed to be an essential process to be applied along the S6PP HRM L1B processing chain.

In order to be as computationally efficient as possible, the range walk correction has been applied following (Rieu et al., 2020), who proposed an approach based on Chirp Zeta-Transform (Oppenheim and Schafer, 1975).

The Chirp Zeta-Transform approach allows us to efficiently carry out the range walk correction inside the beam-forming stage in an approximate beam-steering configuration, while an alternative approach in (Scagliola et al.

2021) requires a more time-consuming exact beam-steering configuration. The CZT approach was also previously proposed by (Guccione, 2008) for Cryosat-2 in the frame of the Delay-Doppler algorithm and is also used in spotlight SAR imagery in the frame of the polar format algorithm (Doerry, 2012).

Under reasonable assumptions, (Egido et al, 2017) and (Guccione et al., 2018) provide the following expression of the unfocused Impulse Response Function (IRF or phase history) of a generic (x,y) scatterer as a bi-dimensional function of the slow time η (i.e. time in the illumination period) and fast time t (i.e. time in the transmitted pulse-width):

$$h(\eta, t) = G_{cr} \cdot G_{al} \cdot \exp\left\{j2\pi\left[f_c\tau'(\eta) - (\alpha\tau'(\eta) - f_D)t + \frac{\alpha}{2}\tau'^2(\eta)\right]\right\} \quad (14)$$

where:

$$\begin{cases} \tau'(\eta) = \tau(\eta) - \tau_{trk} = \frac{2(R(\eta) - R_{trk})}{c_0} \\ f_D = \frac{2 \cdot v_r \cdot f_c}{c_0} \end{cases} \quad (15)$$

R represents the distance between the sensor and the generic scatterer (x,y) and R_{trk} is the tracker range.

Neglecting the residual video-phase term $\frac{\alpha}{2}\tau'^2$ (as it is usually done in the case of UF-SAR altimetry and which is expected in particular to be null in the case of a pulse-compression via a matched-filtering as for POS-4), we can reshuffle the terms in (14) as:

$$h(\eta, t) = G_{cr} \cdot G_{al} \cdot \exp\left\{j2\pi\left[\left(1 - \frac{\alpha t}{f_c}\right)f_c\tau'(\eta) + f_D t\right]\right\} \quad (16)$$

Letting $f' = \left(1 - \frac{\alpha t}{f_c}\right)f_c$ and $\tau'' = \frac{f'}{f_c}\tau'$, the equation (16) can be rewritten as:

$$\begin{aligned} h(\eta, t) &= G_{cr} \cdot G_{al} \cdot \exp\{j2\pi[f'\tau'(\eta) + f_D t]\} \\ &= G_{cr} \cdot G_{al} \cdot \exp\{j2\pi[f_c\tau''(\eta) + f_D t]\} \end{aligned} \quad (17)$$

Time τ'' can be regarded as resampled version of the time τ' , with the resampling factor $\frac{f'}{f_c}$ being a linear function of the fast time t . In short, both times τ' and τ'' are linearly and equally spaced but with a different uniform step.

Once this time interpolation is realised, the bi-dimensional problem of the 2D (2 Dimensional) IRF focusing can be decoupled in two mono-dimensional focusing problems: one in azimuth (slow time η) through a FFT in azimuth and one in range (fast time t) through a FFT in range.

However, the interpolation step in SAR processing is usually considered to be an inefficient operation that may easily cause artefacts in the processed data. On the other hand, this interpolation and azimuth-focusing can be accomplished natively in one step via the Chirp Zeta-

Transform algorithm, without requiring any explicit interpolation.

By definition (Oppenheim and Schaffer, 1975), the Chirp Zeta-Transform of a sampled signal $x[p]$ of finite length N_b is given by:

$$X[m] = \sum_{p=0}^{N_b-1} x[p]z_m^{-p} \quad (18)$$

With $z_m = A \cdot W^{-m}$ and $m = 0, 1, \dots, M-1$ and where the complex coefficients A and W are generally expressed by:

$$\begin{cases} A = A_0 e^{j\theta_0} \\ W = W_0 e^{-j\varphi_0} \end{cases} \quad (19)$$

It represents the z-transform of the input signal over spiral contours in the z-plane (Oppenheim and Schaffer, 1975), with A_0 representing the contour radius at the starting sampling point, θ_0 is the phase of the starting sampling point, φ_0 the angular separation between adjacent sampling points, and W_0 the growth ratio of the spiral.

The FFT can be seen as a special case of the CZT for $A_0 = W_0 = 1$, $\theta_0 = 0$ and $\varphi_0 = \frac{2\pi}{M}$ and therefore the FFT can be interpreted as a z-transform of the input signal made over a unit circle at a uniform step given by $\frac{2\pi}{M}$.

In any case, whereas the FFT comes with the intrinsic limitation to compute the frequency spectrum only at a uniform angular step given by $2\pi/M$ (and M can be $N_b \cdot z_p$, where z_p is an eventual zero-padding integer factor and N_b is usually a power of two), the CZT can compute the frequency spectrum at any (desired) uniform angular step given by φ_0 . Hence, with the CZT, the angular step φ_0 can be arbitrary and this gives the possibility to yield a resampled version of the frequency spectrum without any explicit interpolation.

In order to respond to our resampling needs during the beam-forming stage, clearly the CZT needs to be applied with the following parameters: $M = N_b$, $A_0 = W_0 = 1$ and $\varphi_0 = \frac{f'}{f_c} \frac{2\pi}{N_b} = \left(1 - \frac{\Delta f}{f_c}\right) \cdot \frac{2\pi}{N_b}$.

This means that in our case the z-transform is made over a unit circle of the z-plane (A_0 and W_0 are unitary) for N_b samples uniformly spaced, but now having them an angular step size given by $\frac{f'}{f_c} \frac{2\pi}{N_b}$.

The θ_0 is the phase of the starting sampling point. We can tailor the value of θ_0 in order to put the zero-frequency at the centre of the Doppler spectrum (something analogous to the canonical fitshift operation to place the zero-frequency at the middle of the spectrum) and in order to correct for the Doppler centroid f_D (as typically done during the beam-forming stage):

$$\theta_0 = \frac{f'}{f_c} \frac{2\pi}{N_b} \left(-\frac{N_b}{2} + \frac{f_D}{df} \right) \quad (20)$$

here df is defined in (34).

Therefore, the final expressions of the coefficients A and W are given by:

$$\begin{cases} A = e^{2\pi j \frac{f'}{N_b f_c} \left(-\frac{N_b}{2} + \frac{f_D}{df} \right)} \\ W = e^{-2\pi j \frac{f'}{f_c} \frac{1}{N_b}} \end{cases} \quad (21)$$

In the case $f' = f_c$, we re-find the classic beam-forming by FFT.

The phase of the coefficients A and W is thus a linear function of the fast time t (i.e. of the range bins). We can further break down the time $\tau''(\eta)$ as:

$$\begin{aligned} \tau''(\eta) &= \frac{2}{c_0} \frac{f'}{f_c} (R_0 + \delta R(\eta) - R_{trk}) \\ &= \frac{2}{c_0} \frac{f'}{f_c} (R_0 - R_{trk}) + \frac{2}{c_0} \frac{f'}{f_c} \delta R(\eta) \end{aligned} \quad (22)$$

where R_0 is the range between the burst centre and the generic scatterer.

The term $(R_0 - R_{trk})$ is the usual slant range migration term compensated by a phase rotation prior to the range-compression stage, whereas $\delta R(\eta)$ is sometimes referred to as “range walk”: it represents the variation in range distance during the burst acquisition (Guccione, 2008) (Scagliola et al. 2021).

Under the first-order approximation (being $R_0 \gg \delta R$), and taken the burst centre as the origin of the slow time and of the along-track coordinate \times of the generic scatterer, the range walk is given by:

$$\begin{aligned} \delta R(\eta) &\approx V_s \cdot \eta \cdot \sin(\theta_{Look}) \approx V_s \cdot \eta \cdot \theta_{Look} \approx V_s \cdot \eta \cdot \frac{x}{H} \\ &= V_s \cdot PRI \cdot \left(p - \frac{N_b - 1}{2} \right) \cdot \frac{x}{H} \end{aligned} \quad (23)$$

where p is the pulse index varying between 0 and $N_b - 1$, whereas \times varies with the index m. As expected, the range walk is zero at nadir and gets bigger off-nadir.

Thus, from the CZT definition in (18), collecting all the terms, the operation which we are carrying out basically consists in:

$$\begin{aligned} X[m] &= \sum_{p=0}^{N_b-1} e^{j2\pi f_c \left[\frac{2f'}{c_0} V_s \cdot PRI \cdot \left(p - \frac{N_b-1}{2} \right) \cdot \frac{x}{H} \right]} e^{-2\pi j \frac{f'}{f_c} \left(p - \frac{N_b-1}{2} \right) \frac{f_D}{df}} \left(m - \frac{N_b}{2} + \frac{f_D}{df} \right) \\ &= \\ &= \sum_{p=0}^{N_b-1} e^{j2\pi f_c \left[\frac{2f'}{c_0} V_s \cdot PRI \cdot \left(p - \frac{N_b-1}{2} \right) \cdot \frac{x}{H} \right]} e^{-2\pi j \frac{f'}{f_c} \left(p - \frac{N_b-1}{2} \right) \frac{f_D}{df}} e^{-2\pi j \frac{f'}{f_c} \left(p - \frac{N_b-1}{2} \right) \frac{f_D}{df}} = \\ &= e^{-2\pi j \frac{f'}{f_c} \left(\frac{N_b-1}{2} \right) \frac{f_D}{df}} \sum_{p=0}^{N_b-1} e^{-2\pi j \frac{f'}{f_c} \left(\frac{2f'}{c_0} V_s \cdot PRI \cdot \frac{x}{H} \cdot N_b + l \right) \frac{f_D}{df}} = \\ &= e^{-2\pi j \frac{f'}{f_c} \left(\frac{N_b-1}{2} \right) \frac{f_D}{df}} \sum_{p=0}^{N_b-1} e^{2\pi j \frac{f'}{f_c} \left(\frac{x}{Lx} - l \right) \frac{f_D}{df}} = \\ &= e^{-2\pi j \frac{f'}{f_c} \left(\frac{N_b-1}{2} \right) \frac{f_D}{df}} \sum_{n=-\frac{N_b-1}{2}}^{\frac{N_b-1}{2}} e^{2\pi j \frac{f'}{f_c} \left(\frac{x}{Lx} - l \right) \frac{f_D}{df}} = \end{aligned}$$

$$\begin{aligned}
& e^{-2\pi j \frac{f'}{2f_c} \left(\frac{N_b-1}{N_b} \right)} \cdot N_b \\
& \cdot \text{sinc} \left\{ \frac{f'}{f_c} \left(\frac{x}{L_x} - l \right) \right\} / \text{sinc} \left\{ \frac{1}{N_b} \frac{f'}{f_c} \left(\frac{x}{L_x} - l \right) \right\} \\
& \approx \\
& e^{-2\pi j \frac{f'}{2f_c} \left(\frac{N_b-1}{N_b} \right)} \cdot N_b \cdot \text{sinc} \left\{ \frac{f'}{f_c} \left(\frac{x}{L_x} - l \right) \right\} \quad (24)
\end{aligned}$$

with $l = m - \frac{N_b}{2} + \frac{f_D}{df}$, L_x is defined in (34) and we have exploited the well-known relationship (Rudin, 1976):

$$\sum_{n=-\frac{N_b-1}{2}}^{\frac{N_b-1}{2}} e^{2\pi j \frac{n\xi}{N_b}} = \frac{\sin(\pi\xi)}{\sin\left(\frac{\pi\xi}{N_b}\right)} = N_b \cdot \frac{\text{sinc}(\xi)}{\text{sinc}\left(\frac{\xi}{N_b}\right)} \approx N_b \cdot \text{sinc}(\xi) \quad (25)$$

and the normalised sine cardinal (sinc) definition and approximation.

The peak position of (24) is given by $x_{peak} = L_x \cdot l$ and is independent on the fast time t .

After the azimuth-focusing by CZT, the azimuth response is therefore a sinc function centred on beam l but evaluated over a resampled grid (see Fig. 6-right) with a resampling rate given by $\frac{f'}{f_c}$.

The CZT is typically realised using the Bluestein's formulation (Rabiner et al., 1969):

$$\begin{aligned}
X[m] &= CZT(x[p]) \\
&= W^{\frac{m^2}{2}} \cdot \text{IFFT} \left(\text{FFT} \left(x[p] \cdot A^{-p} \cdot W^{\frac{p^2}{2}} \right) \cdot \text{FFT} \left(W^{-\frac{p^2}{2}} \right) \right) \quad (26)
\end{aligned}$$

Which provides a computationally efficient way to yield the CZT based on a popular FFT library as FFTW (Frigo and Johnson, 1998).

Once the burst data are arranged in a matrix of N_b rows and N_p columns, $x[p]$ in equation (26) is the k_{bin} -th azimuth row of the matrix and (26) has to be carried out for each azimuth row (i.e. for each range bin k_{bin}). Then, the CZT operation in (26) has to be carried out per burst along the product pass (burst loop), similar to the beam-forming via FFT approach, in which a FFT operation is carried out per burst.

Since the term $\text{FFT} \left(W^{-\frac{p^2}{2}} \right)$ is not dependent on the input signal $x[p]$, it can be computed only one time and outside of the burst loop. Therefore, apart from the complex multiplications, the CZT-based beam-forming computational complexity consists of one FFT operation, and one IFFT operation in contrast to FFT-based beam-forming in which the computational complexity is driven by one FFT operation. In short, the better focusing through the CZT-based beam-forming is achieved at the expense of a moderately higher computational cost than the FFT-based beam-forming (i.e. just one extra IFFT per burst).

Prior to performing the range-compression, it is necessary to compensate for the phase ramp term $e^{-2\pi j \frac{f'}{2f_c} \left(\frac{N_b-1}{N_b} \right)}$ in equation (24) since, otherwise, this phase rotation term will translate into unwanted range shifts after the range-compression step.

For this purpose, after the azimuth-focusing by CZT, a phase rotation shift by of $\frac{1}{2} \frac{f'}{f_c} \left(\frac{N_b-1}{N_b} \right)$ is applied to the $X[m]$ matrix:

$$\tilde{X}[m] = X[m] \cdot e^{2\pi j \frac{f'}{2f_c} \left(\frac{N_b-1}{N_b} \right)} \quad (27)$$

The expression (14) has been originally derived assuming by convention a negative chirp slope sign (Egido et al, 2017), which is usually the case for radar altimetry. But, in a more general case, it stands:

$$\frac{f'}{f_c} = \left(1 + \text{sgn}_{chirp} \frac{\alpha t}{f_c} \right) \quad (28)$$

The scheme in Fig. 7 is tested for the S6-MF Crete transponder pass on 18 December 2020.

The 2D PTR for the outer (off-nadir) beam #-24 is displayed in Fig. 8 in the case of ABS + CZT beam-forming (the first on the left plot), in the case of EBS + 64FFT beam-forming (the second on the left plot) and in the case of ABS + FFT beam-forming (the third on the left plot). The case EBS + 64FFT is carried out applying the range walk correction following (Scagliola et al., 2021).

Whereas the 2D PTR in the case of ABS + FFT beam-forming is clearly blurred, once the beam-forming is carried out via ABS + CZT or through the EBS + 64FFT, the 2D PTR yields a much better focusing, matching the expected ideal 2D PTR (Fig. 8, the fourth on the left plot).

In Table 2, we have quantified the improvement for the azimuth PTR in terms of side-lobe level (the first five side-lobes on the right-hand side and on the left-hand side of the PTR). The side-lobes level in the case of ABS + CZT is significantly closer to the level of side-lobes expected from the theoretical impulse response (squared sinc) compared to the case ABS + FFT and no major deviation is observed with respect to the EBS + 64FFT case. A zoom of the azimuth PTR over the first two side-lobes and for the cases ABS + CZT, ABS + FFT, EBS + 64FFT and squared sinc is shown in Fig. 10.

In any case, compared to the ideal case 2D squared sinc, the 2DPTR, yielded by the ABS + CZT beam-forming, is still slightly degraded in the trailing part along the range direction (between the range gates -35 and -20 in Fig. 8, see also in Fig. 9 the PTR right side-lobe which is higher than the left side-lobe). This degradation is considered to originate from the transponder itself (Amraoui et al., 2021) and not from the processing errors. We have the same degradation even in the case of EBS + 64FFT.

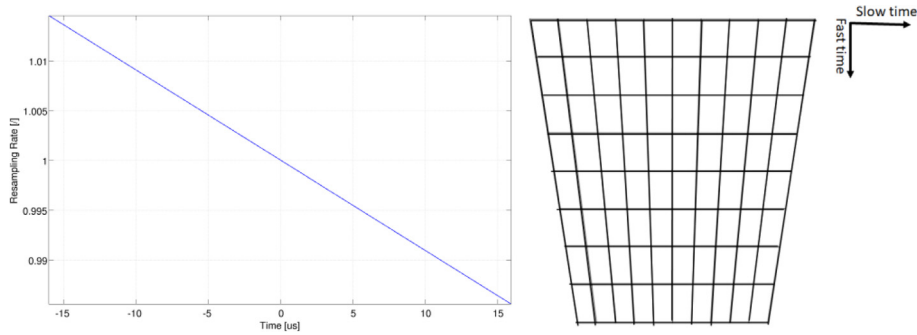


Fig. 6. Plot of the resampling rate $\frac{f'}{f_c}$ versus fast time (left). “Trapezoidal” grid driven by the resampling rate function of the fast time (right).

The effect of the phase rotation multiplication in equation (27) is displayed in Fig. 9: with this phase rotation multiplication, after range-compression, the range PTR is range shifted and is now aligned in range with the range PTR yielded by the FFT-based beam-forming.

The computational complexity of the different algorithms is $O(N_b \cdot \ln(N_b))$ for ABS + FFT, $N_b \cdot O(N_b \cdot \ln(N_b))$ for EBS + 64FFT and is $2 \cdot O(N_b \cdot \ln(N_b))$ for ABS + CZT where the symbol $O()$ means “of the order of” and \ln is the natural logarithm.

The equation (23) for the range walk is strictly valid only if the vertical displacement of the centre of phase of the instrument is neglected. Hence, after the azimuth-focusing by CZT, the orbit height variation inside the burst acquisition still needs to be corrected for (the so-called intra-burst orbit correction).

The S6PP beam-forming stage does not apply the intra-burst orbit correction since this is done on board in the case of RMC or on ground (prior to L1A stage) in the case of RAW data streams (EUMETSAT, 2021b) but, if this is not the case, it shall be included in the beam-forming stage.

The CAL-2 TNR is not applied to calibrate the LRM waveform, following the outcome reported in (Dinardo et al., 2022), given its minimum level of distortions and its excellent temporal stability. Similarly, given the minimal distortions exhibited by the Poseidon-4 along the burst pulses (Dinardo et al., 2022) and given that a sensitivity

analysis has shown a negligible impact on the retracked output from these distortions along the burst, it has been decided to not apply the burst table calibrations.

Following the CryoSat-2 heritage, a zero-padding factor of 2 is applied in the range direction prior to the range FFT operation.

The number of beams in the stack which have been nominally multi-looked is set to 448, which represents the number of the pulses in a burst (64) times the number of bursts in a radar cycle (7). Since the default tracking gate is set to 50 (or 100 with a zero-padding of 2), by geometrical reasons, it happens that all the 448 looks are received in the data stack and can be multi-looked (see for instance Fig. 12-left).

The nominal posting rate of the surface grid points is set to about 20 Hz.

5.2. L2 HRM processing baseline

In this subsection, we are going to describe the main processing algorithms which are part of the HRM L2 processing baseline. The main HRM L2 processing algorithms are summarised in Table 4.

At L2, as UF-SAR waveform model, we use the one proposed by (Buchhaupt et al., 2018) which provides a waveform model analytical formulation in the frequency domain which is then converted in the time domain by an IFFT operation.

Clearly, for the UF-SAR chain, the same PDF formulation is used as expressed by equation (6).

As skewness coefficient, a Jason mission heritage value of 0.1 is used since it is obvious that the same ocean topography model must be used for the LRM and UF-SAR chain for the sake of processing baseline consistency between the two modes.

Also, in the UF-SAR retracking scheme, the same interface to the in-flight PTR is implemented as proposed in section 4.

Therefore, we are using the same waveform model derivation for LRM and UF-SAR chain with the only difference represented by the expression of the FSSR between LRM and UF-SAR which is naturally different. This

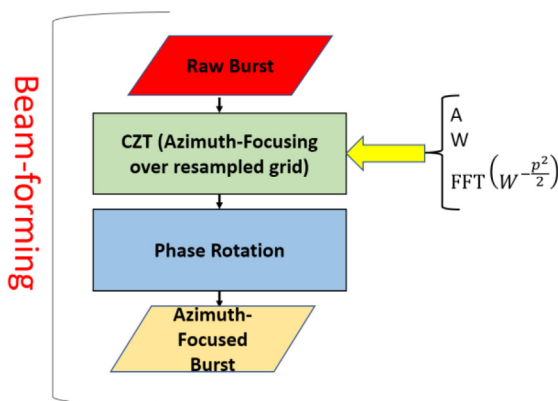


Fig. 7. Flow-chart of the CZT-based beam-forming.

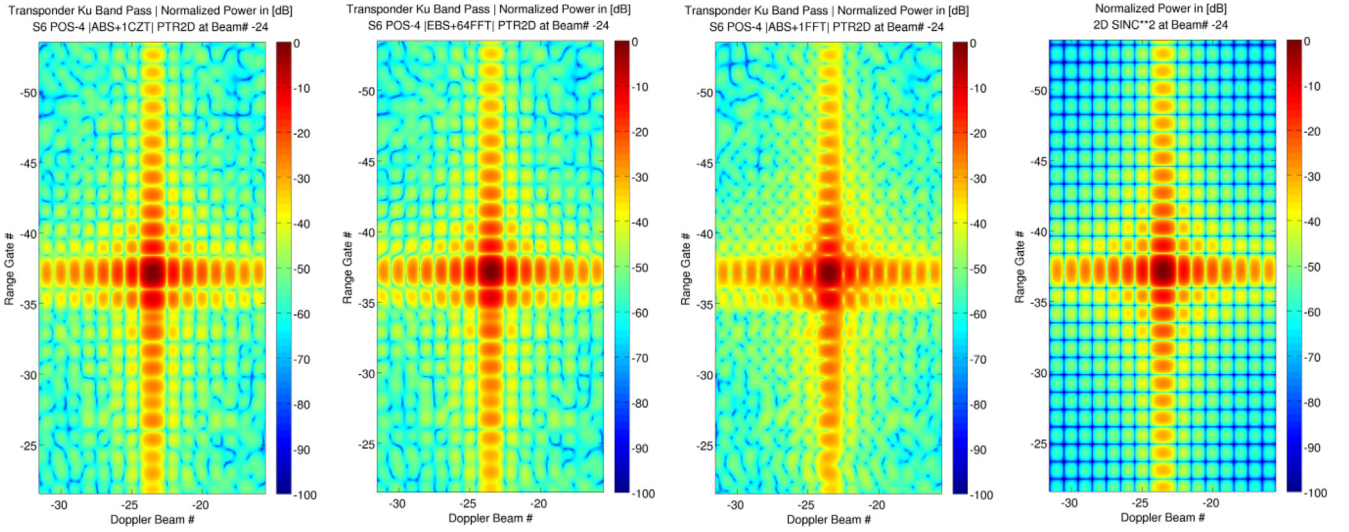


Fig. 8. PTR2D for an outer (off-nadir) beam #-24 over the Crete transponder for the case ABS + CZT (the first on the left), for the case EBS + 64FFT (the second on the left) and for the case ABS + FFT (the third on the left). The ideal PTR2D (squared sinc) is the fourth on the left plot.

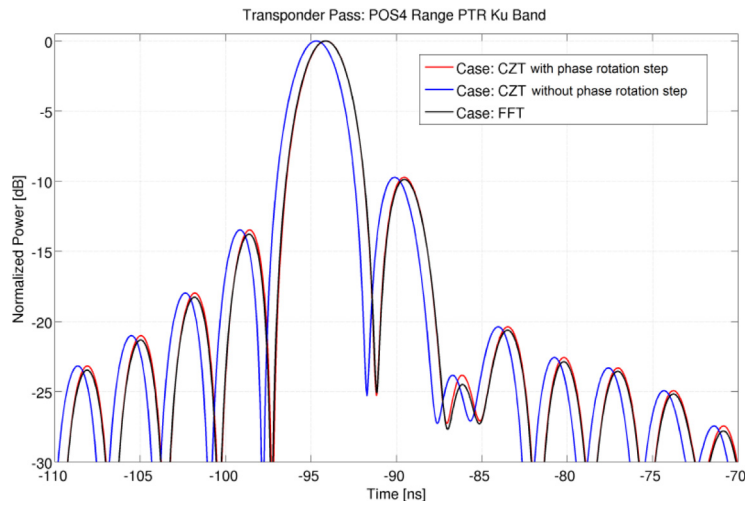


Fig. 9. Effect of the phase rotation in equation (27) for the range PTR (after ABS + CZT-based beam-forming) over the transponder: without this phase rotation step, the range PTR is shifted compared to the FFT-based beam-forming case (blue curve). With the phase rotation compensation step, the range PTR after CZT-based beam-forming (red-curve) is aligned compared to the FFT-based beam-forming case (black curve).

approach is also expected to enhance the level of consistency between the LRM and UF-SAR measurements.

By instrument design (Raney, 2012) (Phalippou et al., 2012), the S6-MF received data are sampled “in slow time” at a PRF rate which is lower than the Doppler bandwidth. That means that Nyquist’s rate is not fulfilled, and data are under-sampled in the “slow time” dimension. The Doppler bandwidth B_D is given by:

$$B_D = \frac{2V_s}{\lambda_0} \sin(\Delta\theta_{x3dB}) \quad (29)$$

where $\Delta\theta_{x3dB}$ is the 3 dB antenna aperture in the along-track direction. B_D takes a value around 16 kHz, which is higher than the PRF.

Therefore, after the beam-forming stage, the burst data are aliased with the folding occurring at the two frequencies:

$$f_{Fold} = f_D \pm \frac{PRF}{2} \quad (30)$$

where f_D is the Doppler Centroid Frequency. The along-track position of the folding is then:

$$x_{Fold} = \frac{f_{Fold} L_x N_b}{PRF} \quad (31)$$

The consequence of this design choice is that azimuth ambiguities show up on the burst data at position given by equation (31) and thus, after the stacking and range-alignment, on the stack data (see Fig. 12-left).

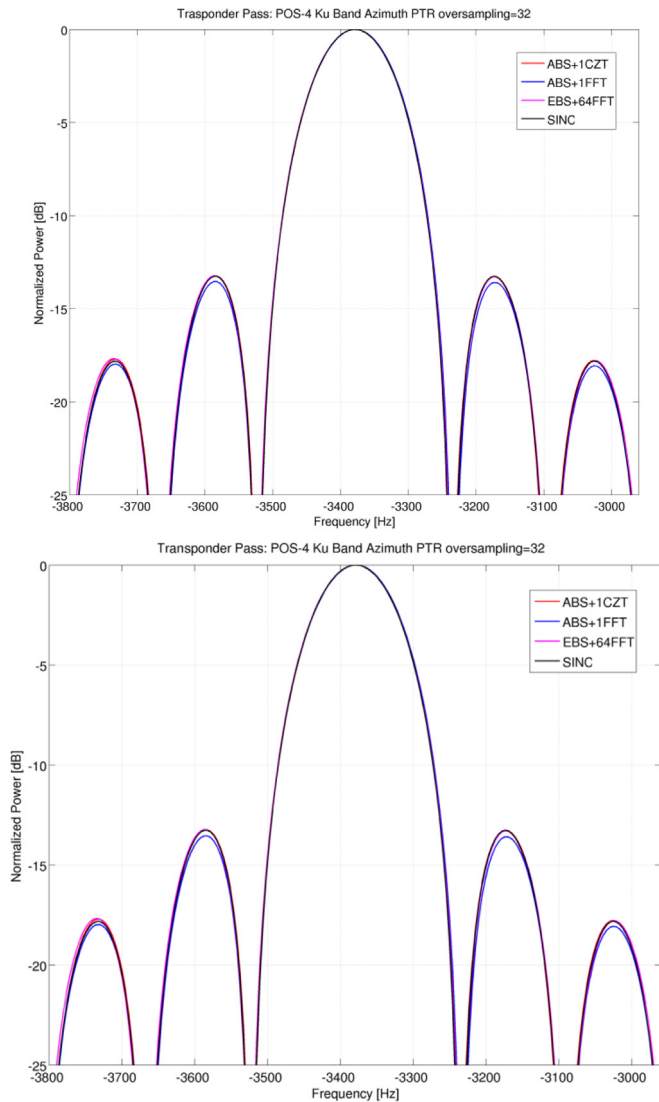


Fig. 10. Transponder azimuth PTR for the cases ABS + CZT, ABS + FFT, EBS + 64FFT and SINC**2.

The S6PP UF-SAR retracker does not implement any dedicated ambiguity masking as the PDP does, but the ambiguities are generated by the waveform model and retained in the Delay-Doppler Map (see Fig. 11-right). This approach is different from the PDP one in which the ambiguities are masked out on the stack data side, and they are not generated on the SAMOSA (Ray et al., 2015) model's DDM side (EUMETSAT, 2021c), see Fig. 11-left.

Still, due to the limited size of the Poseidon-4 radar receiving window, after the range-alignment stage, the Doppler beams in the stack are usually padded with zeroes or with a placeholder like NaN (Not a Number), see Fig. 12-left for instance. After the stack range-alignment stage, the ambiguities appear with a triangular shape at each side of the stack, given the parabolic profile of the slant range shift; see also (Phalippou et al., 2012).

In order to maintain the one-to-one consistency between the model's DDM and the stack data, it is necessary to

compute at L1B from the stack data a bitwise mask giving the position of the pixels in stack data matrix wherein the zeroes (or NaN) are located and then apply this mask at L2 after the model DDM generation in order to place the zeroes (or NaN) in the model's DDM at the same pixel positions. In S6PP, this zero-mask is constructed using the total range shift (sum of the slant range shift, the tracker range shift and the Doppler range shift) as computed and applied at L1B to align the Doppler beams in the stack in range (i.e. using exact range shifts). This operation is usually referred to as DDM zero-masking (CP40 Project Report 2014a), (CP40 Project Report 2014b) or DDM geometry masking (EUMETSAT, 2021b).

As a result, only this geometry masking needs to be applied on the S6PP model's DDM at L2.

The proposed approach to deal with the Doppler ambiguities applies only in the case of a sufficiently small surface slope in the along-track direction, as is expected for the ocean surface, which is the focus of the paper. In the case of higher surface slope in the along-track direction (over land ice as an example) the slope is expected to combine with the mis-pointing component in the along-track direction so that the location of the ambiguities in the stack might be modified as well as their power due to the different section of the antenna pattern which is pierced.

The model's DDM is evaluated in input at exact look angles as computed at L1B stage and provided in the S6PP L1B data products.

Following the outcome from (Figerou et al., 2020), the model DDM is not computed for all the beams (i.e. 448) but a decimation of “3 out of 7” (known as beam subsampling operation) is considered sufficient and applied. For a “3 out of 7” beam configuration, the assessment of the impact of the Doppler beam sampling factor by (Figerou et al., 2020) shows that the impact in range is negligible whereas in SWH is about 5 cm at maximum for SWH larger than 5 m.

Finally, the model waveform (in red in Fig. 13) is computed by multi-looking all the decimated DDM beams.

The model is computed using a spectral oversampling factor of 4 in the frequency domain.

The choice of 4 was verified comparing the retracking results from the frequency domain numerical retracker against a “reference” time domain numerical retracker based on the DDM model formulation provided by Ray et al., 2015:

$$P_{k,l} = \frac{\lambda_0^2}{(4\pi)^3} \int_{-\infty}^{+\infty} dz PDF(z) \int_{-\infty}^{+\infty} dx \int_{-\infty}^{+\infty} dy \times \frac{\Gamma(x,y)}{R^4(x,y,z)} |C_{k,l}(x,y,z)|^2 \quad (32)$$

where $\Gamma(x,y) = G^2(x,y)\sigma_0(x,y)$ is the product between the two-way antenna irradiation power gain and the surface backscattering coefficient and where $|C_{k,l}(x,y,z)|^2$ is the instrument impulse power response after Range Cell

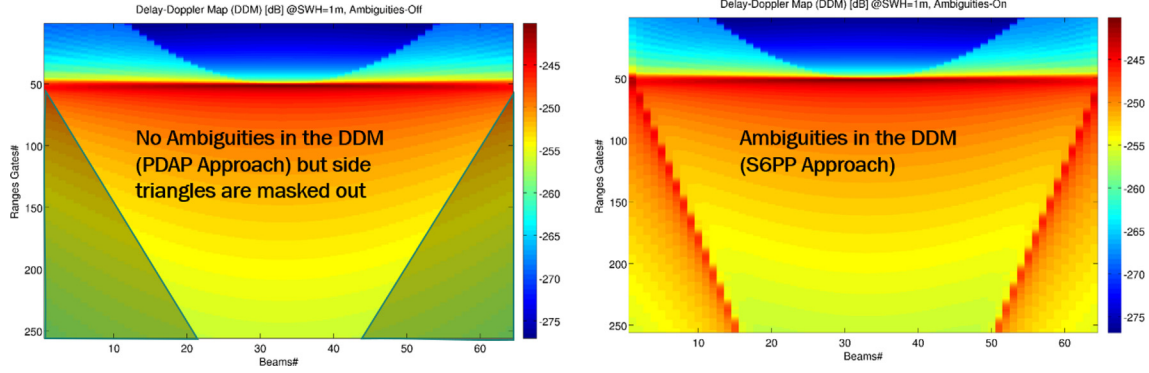


Fig. 11. On left, the PDP approach to deal with the ambiguities: DDM does not include the ambiguities but the triangular “ambiguity zones” are masked out. On right, the S6PP approach to deal with the ambiguities: DDM is natively generated with ambiguities and no ambiguity masking is applied.

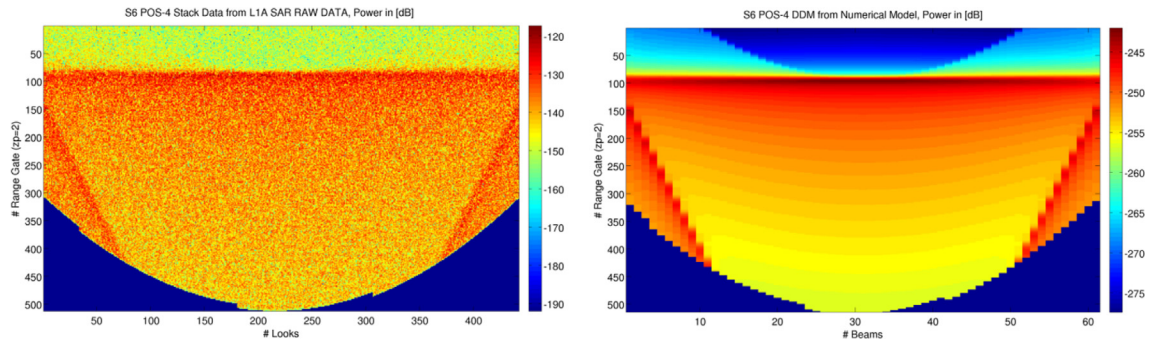


Fig. 12. Ambiguous stack data (left) after range-alignment and ambiguous DDM (right) after the geometry masking.

Migration Correction (RCMC) and Doppler Centroid Correction (DCC) which is expressed in Ray et al., 2015 as:

$$|C_{k,l}(x, y, z)|^2 = N_p^2 N_b^2 PTR_{k,l}^{rge}(x, y, z) \cdot PTR_l^{azi}(x) \approx \left[N_b N_p \text{sinc}\left(\frac{BW}{F_s}(k - k_l)\right) \cdot \text{sinc}(u) \right]^2 \quad (33)$$

where $PTR_{k,l}^{rge}$ is the range PTR, PTR_l^{azi} is the azimuth PTR, and we take into account that now for S6-MF $BW \neq F_s$, and we make the following definitions:

$$\left\{ \begin{array}{l} u = \frac{x}{L_x} - l \\ v = \frac{y}{L_y} \\ w = \frac{z}{L_z} \\ R(x, y, z) = H - z + \frac{2\alpha_{Earth}}{2H} [x^2 + y^2] \\ k_l = 2l \left(\frac{L_x}{L_y}\right)^2 u + \left(\frac{L_x}{L_y}\right)^2 u^2 + v^2 - w \\ k = k_{bin} - k_0 \\ df = \frac{PRF}{N_b} \end{array} \right\} \left\{ \begin{array}{l} L_x = \frac{H \alpha_{Earth}}{2V_s} \\ L_y = \sqrt{\frac{c_0 H}{\alpha_{Earth} F_s}} \\ L_z = \frac{c_0}{2F_s} \\ \alpha_{Earth} = \left(1 + \frac{H}{R_{Earth}}\right) \\ k_{bin} = \text{rangebin}[0, N_p - 1], k_0 \text{retrackingbin} \\ l = \text{DopplerBeam}\left[-\frac{N_b}{2}, \frac{N_b}{2} - 1\right] \end{array} \right. \quad (34)$$

We have adopted the approximation proposed in (Ray et. III.A, 2015) based on the peakiness of the $|C_{k,l}(x, y, z)|^2$ function around the maximum point $(x, y)|_{max} = (l \cdot L_x, L_y \cdot \sqrt{k + w})$ and on the slow-varying behaviour of the function $\Gamma(x, y)/R^4$ over the (x-y) integration domain, which makes it possible to re-write the (32) as:

$$P_{k,l} \cong \frac{\lambda_0^2}{(4\pi)^3} \int_{-\infty}^{+\infty} PDF(z) \cdot \left(\frac{\Gamma_{k,l}^e(z)}{R_{k,l}^4(z)}\right) \cdot W_{k,l}(z) \cdot dz \quad (35)$$

With:

$$W_{k,l}(z) = \int_{-\infty}^{+\infty} dx \int_0^{+\infty} dy |C_{k,l}(x, y, z)|^2 \quad (36)$$

And where $\Gamma^e(x, y) = \Gamma(x, y) + \Gamma(x, -y)$ and finally:

$$\left\{ \begin{array}{l} \Gamma_{k,l}^e(z) = \Gamma^e(x = L_x \cdot l, y = L_y \cdot \sqrt{k + w}) \\ R_{k,l}(z) = R(x = L_x \cdot l, y = L_y \cdot \sqrt{k + w}, z) \text{ if } w \geq -k \end{array} \right. \quad (37)$$

$$\left\{ \begin{array}{l} \Gamma_{k,l}^e(z) = \Gamma^e(x = L_x \cdot l, y = 0) \\ R_{k,l}(z) = R(x = L_x \cdot l, y = 0, z) \text{ if } w < -k \end{array} \right. \quad (38)$$

For the waveform model expressed by (35) to be able to reproduce a DDM with ambiguities, the $PTR_l^{azi}(x)$ term in (33) can be computed by a FFT using the following formula:

$$PTR_l^{azi}(x) = \left| \text{FFTSHIFT}\left(\frac{1}{N_b} \text{FFT}\left(e^{2\pi j\left(\frac{x}{L_x}\right)\left(\frac{x}{N_b}\right)}\right)\right) \right|^2 \quad (39)$$

Or, equivalently, the exact solution of the discrete Fourier transform in (39) can be used:

$$PTR_l^{azi}(x) = \left| \frac{\text{sinc}(u)}{\text{sinc}\left(\frac{u}{N_b}\right)} \right|^2 \quad (40)$$

Which is usually referred to as periodic or aliased squared sinc and has a period of N_b .

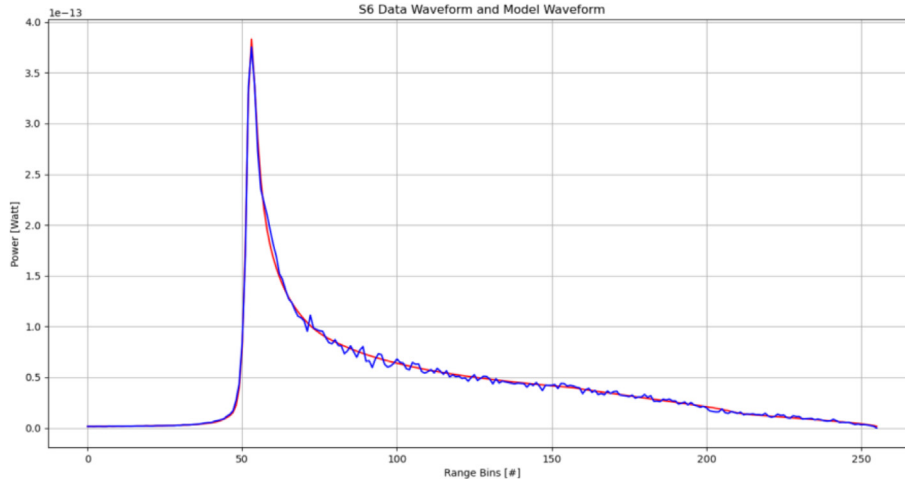


Fig. 13. Example of the fit between the data waveform (in blue) and the model waveform (in red). The “ambiguous” model can accurately reproduce the data power for the full radar window of the 256 range gates. The numerical retracker can also fit the waveform’s toe.

The $PTR_l^{azi}(x)$ term is displayed in dB in Fig. 14-top as function of the along-track distance x and of the beam index l .

The azimuth PTR for beam index $l = 0$ (nadir beam) given by the equation (39) is displayed in Fig. 14-bottom where two ambiguous “replica” PTR rise up at the along-track distance:

$$x_{rep} = \pm N_b \cdot L_x \quad (41)$$

which corresponds to around ± 19.2 km.

The term $W_{k,l}(z)$, which represents the double-integration of the 2D instrument impulse power response $|C_{k,l}(x, y, z)|^2$ over the (x-y) domain, has been pre-computed numerically and hence only the integration (35) along the z-dimension is carried out at retracking run-time.

As two-way antenna power gain pattern, the standard gaussian model has been used, as given by:

$$G^2(x, y) = G_0^2 e^{-\alpha_x(x-x_p)^2 - \alpha_y(y-y_p)^2} \quad (42)$$

$$\begin{cases} \alpha_x = \frac{8 \cdot \ln(2)}{H^2 \Delta\theta_{x,3dB}^2} \\ \alpha_y = \frac{8 \cdot \ln(2)}{H^2 \Delta\theta_{y,3dB}^2} \end{cases} \quad (43)$$

x_p - coordinate of the mispointing point
 y_p - coordinate of the mispointing point

whereas the backscattering coefficient has been considered uniform over the antenna footprint and expressed by an amplitude term P_u .

In practice, a more realistic antenna pattern model, based on the Bessel function, as proposed in (Dinardo et al., 2022) can be tested or even a more sophisticated backscattering model such as Geometric-Optics or Physical-Optics (Beckman and Spizzichino, 1963).

Once a few passes are processed by the time domain and frequency domain retracker, the results show an excellent

level of consistency between them with a range bias less than 1 mm and a SWH bias less than 1 cm (see Fig. 15).

The α_p LUT used by the PDP in the SAMOSA retracker was computed by the waveform model given in (32), assuming that:

$$PTR_l^{azi}(x) = |\text{sinc}(u)|^2 \quad (44)$$

since the ambiguities in the PDP stack data are masked out by a dedicated ambiguity masking and they don’t get generated on the SAMOSA model’s DDM side (EUMETSAT, 2021c).

The method to compute the thermal noise from the early waveform samples is also used in the S6PP HRM chain in which the “noise range bins” [12 → 16] are now used. These values are the same as used by the PDP version 3.2.4.

About the retracking window size, a value of 10 as first gate and 132 as last gate is chosen since the purpose is to use the same window size for the RMC and RAW data streams.

These values are the same used by the PDP version 3.2.4.

The range-compression from 20 Hz to 1 Hz is carried out by the Absolute Deviation Method (ADM) on the 20 Hz range – 20 altitude Hz quantity, then the 1 Hz altitude is added to retrieve the 1 Hz range. This is the same PDP approach.

The SWH (respectively sigma0) compression from 20 Hz to 1 Hz is carried out by a direct averaging of the 20 Hz SWH (respectively sigma0). The negative SWH are estimated from the retracker and considered valid 20 Hz measurements in the compression.

The fitting scheme used inside the HRM retracking is a standard Levenberg-Marquardt least-squares algorithm with three fitting unknown parameters: epoch, significant wave-height, amplitude whereas the roll and pitch platform mis-pointing angles are provided in input. As platform

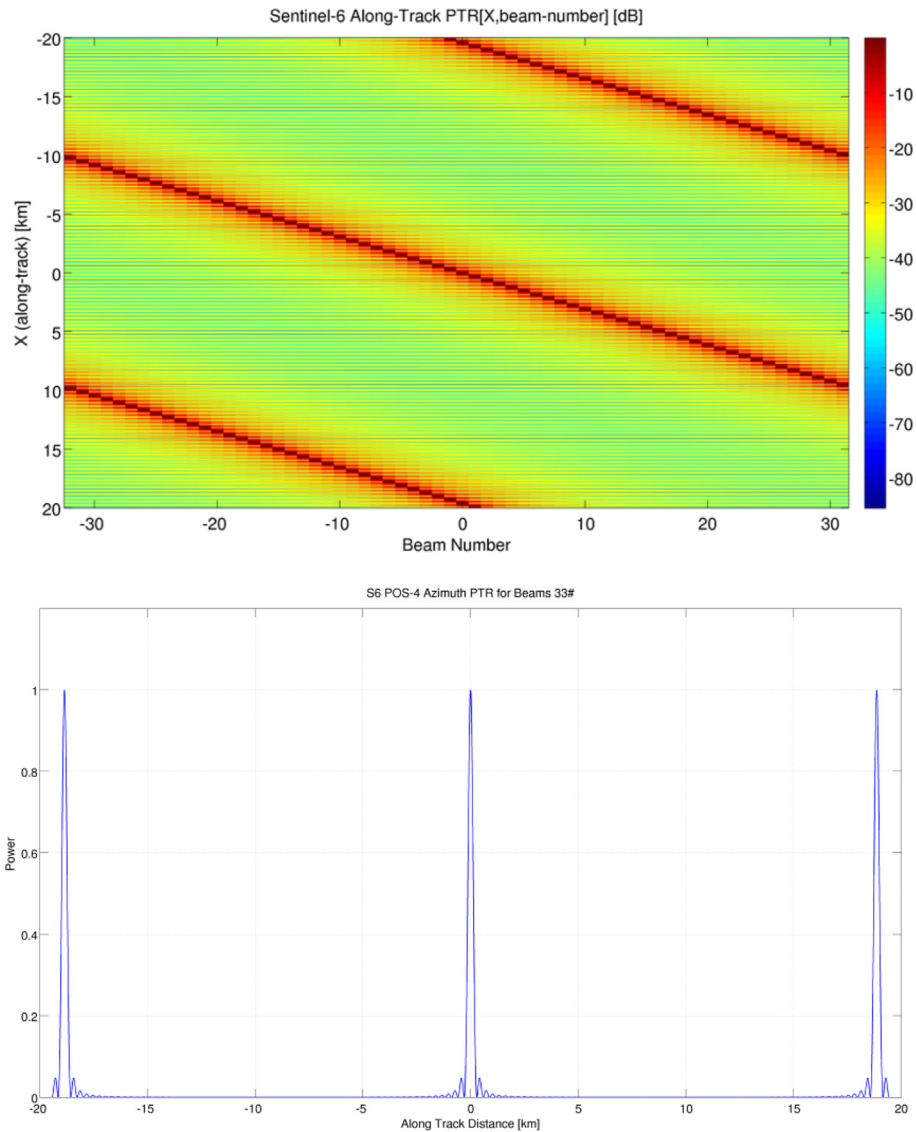


Fig. 14. (Top) Azimuth PTR in dB as expressed by equation (39) as function of the along-track distance x and of the beam index l ; (Bottom) cut of this bi-dimensional function at beam index $l = 0$ (nadir).

mis-pointing angles in input to the waveform model, we have used constant values as estimated from the operated roll/pitch cross-manoevres and from the 90° yaw-flip manoeuvre which are -0.03° for the roll and -0.005° for the pitch.

With the regard to the computational time, for a single thread of execution, the HRM frequency domain numerical retracker implemented in S6PP is typically twice as slow as real-time if the beam sub-sampling factor is set to “1 out of 7” and once the mis-pointing angles are null in input. If the aim is to have non-null mis-pointing angles, the computational time increases by a factor of two since the waveform model FSSR becomes complex-valued in the frequency domain.

Using the CNES cluster high computing capabilities, one year of S6-MF L1A data products can be processed to UF-SAR L2 in only 5 days.

6. S6PP Cal/Val analysis in LRM and HRM

6.1. LRM Cal/Val and sensitivity analysis

A full assessment of the S6PP LRM dataset is carried out over open ocean. For this Cal/Val analysis, the 1 Hz NTC latency is used from the beginning of the tandem phase until December 2021.

To compute POS-4 SSHA, the same geophysical corrections are applied on both Jason-3 GDR-F and S6PP LRM datasets. In particular, we use the ECMWF wet tropospheric correction and the Jason-3 GDR-F filtered ionosphere correction on the S6PP LRM dataset. Note that two orbit solutions are considered: CNES POD POE-F (Precise Orbit Ephemeris-F) orbits and JPL POE orbits. The sea state bias is recomputed using the Jason-3 GDR-F sea state bias solution applied on the S6PP LRM data (i.e. to the S6PP LRM SWH and wind speed).

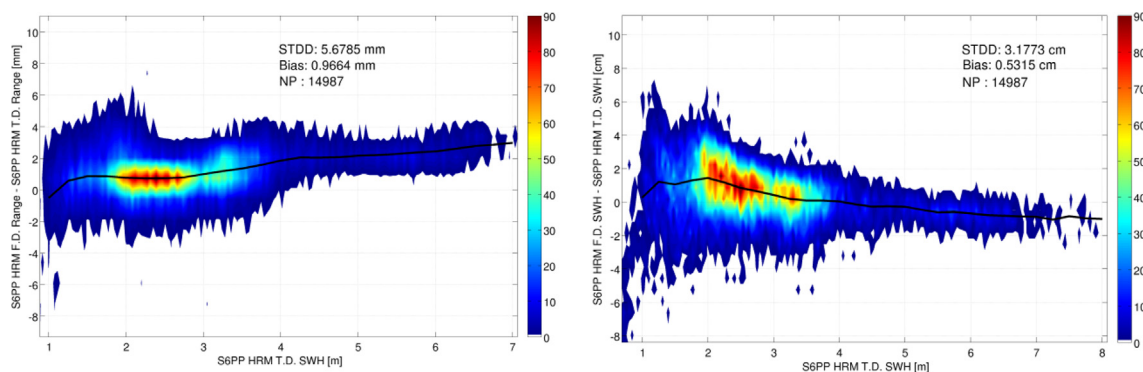


Fig. 15. Cloud-plot of the difference between frequency domain and time domain retracker versus HRM SWH for range (left-hand side plot) and SWH (right-hand side plot).

The quality assessment of the POS-4 SSHA mainly points out the existence of an east–west hemispheric bias (see Fig. 16-left, case POS-4 side-A) in the difference between S6PP and J3 SSHA, which is mitigated once the JPL orbits are used on both the J3 and S6-MF sides (see Fig. 16-right).

Note that the root-cause of this bias was identified and corrected via a CNES POD orbit update consisting in blocking the GNSS phase ambiguities for the orbit computation. The update is applied as from the cycle 22 in the PDAP operational orbit products.

After the cycle 22, the east–west hemispheric bias appears to be less strong in the case of the CNES POD orbit (see Fig. 17, for the POS-4 side-B). From the cycle 22 on, using the CNES POD orbit or JPL orbit to compute the SSHA difference between S6PP LRM and J3 gives identical results in terms of geographical pattern. The mean values of the SSHA bias are -0.44 cm in the case of the CNES POD orbit and -0.20 cm in the case of the JPL orbit. This is an excellent result for the S6PP LRM dataset showing an excellent consistency with Jason-3. In addition, the maps do not highlight any significant sea state dependency, except for the low SWH areas.

In all the cases, a strip at equator with few mm of amplitude appears and whose origin is still under investigation. A secondary strip at 40 S is visible as well, with a minor amplitude than the equatorial band.

The time series of the SSHA difference reveals a jump of a few mm occurring concomitantly with the update of the satellite central software on 27/28 April 2021, as shown in Fig. 18-left. Also, the AMR-C WTC underwent an update on 17 March 2021 (see Fig. 18-right), which explains the jump around that day in the SSHA difference time series if the AMR-C WTC is used.

The SSH differences at mono-mission crossover enable highlighting any discrepancies between ascending and descending tracks. A maximum time lag of 10 days is set to reduce any error in the performance estimation, linked to the ocean variability. The SSH difference at mono-mission crossover reveals the consistency between the

Jason-3 and S6PP LRM performances in terms of mean and standard deviation.

The crossover residual distribution is very similar in both cases: centred around 0 and varying between -1.5 cm and 1.5 cm (Fig. 19 for the CNES POD orbits and Fig. 20 for the JPL orbits).

The J3 and S6PP LRM time series of the SSH crossover mean do not reveal any major discrepancies between the two missions (see Fig. 21-left). The standard deviation of the SSH difference at crossover is a great marker of the overall data quality. Results highlight the stability of the processing with a consistent standard deviation between J3 and S6PP LRM (centred around 5.3 cm with the CNES POD POE-F orbit), and stable in time (see Fig. 21-right). Note that the peak visible on the S6PP LRM standard deviation at the end of April 2021 is concomitant with the update of the satellite central software on 27/28 April 2021, as already mentioned.

To fully characterise the SSHA behaviour at all observable wavelengths, a spectral analysis is performed. The power spectrum is computed on an SSHA without the geophysical corrections (that is orbit – range – mean sea surface), for J3 IGDR-F (Intermediate Geophysical Data Record-F) and S6PP LRM. In order to properly compare the results between missions, the power spectra are computed on the same sets of points for all datasets.

The LRM SLA wavenumber spectra (Fig. 22, left plot) can be split in three parts. First, we have the oceanic slope for wavelengths larger than 100 km, characterised by a linearly decreasing spectra. J3 and S6PP LRM oceanic slope are perfectly in line. The two satellites thus have the same capability to detect the oceanic signal down to 100 km.

The second part of the spectra exhibits the transition to a constant white noise level (third part), reached around 3 km. Between 3 and 100 km, both satellites exhibit the well-known LRM bump (Dibarboure et al, 2014). The amplitude of this bump is identical for both datasets, as shown after the noise plateau removal (Fig. 22, right plot). This amplitude of the LRM bump was expected to be the same between the two missions since the S6-MF retracking

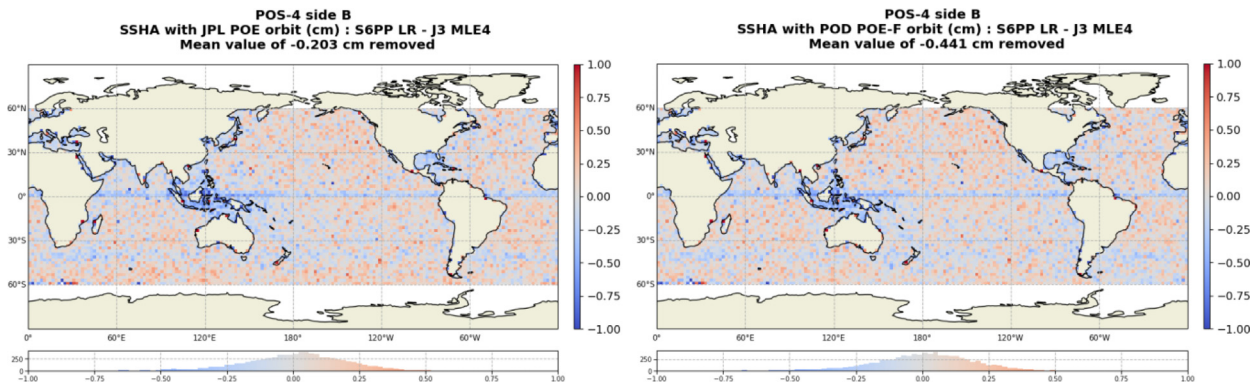


Fig. 16. Geographical map of the difference between S6PP LRM and J3 SSHA if the CNES POD orbits are used (left) and if JPL orbits are used (right). The SSHA is computed using ECMWF wet tropospheric correction and is relative to side-A only. The axis unit is the degree.

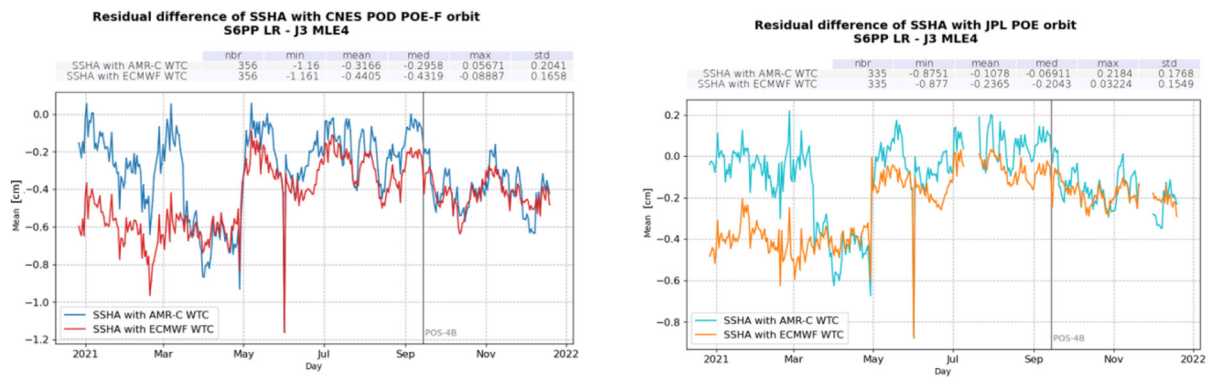


Fig. 17. Geographical map of the difference between S6PP LRM and J3 SSHA if the CNES POD orbits are used (left) and if the JPL orbits are used (right). The SSHA is computed using ECMWF wet tropospheric correction and is relative to side-B only. The axis unit is the degree.

window size has been “ad-hoc” tuned to have the same size in metres as in Jason-3. From 100 km, the two spectra are no longer in line. The S6PP LRM spectrum displays a lower level of energy, resulting in a lower level of noise compared to Jason-3 by 0.8 cm rms.

In Fig. 23, the geographical map of the difference between the J3 and S6PP LRM SWH is shown (left-hand side), along with their histogram (right-hand side).

The consistency in the SWH measurement between the two missions is again excellent with no significant bias, a standard deviation of the difference less than 2 cm and with centimetric differences limited to only low sea state conditions (SWH < 1 m) and related to a different standard which is used between J3 and S6PP to compress the 20 Hz SWH in the 1 Hz SWH.

The wavenumber spectra analysis confirms the excellent agreement between J3 and S6PP LRM SWH dataset with a consistent level of the spectral bump between the two missions and a lower level of random noise in favour of S6PP LRM (see Fig. 24), due to the higher number of accumulated looks compared to the Jason-3 case.

The wind speeds at a height of 10 m from the ocean surface are computed from the altimeter sigma0 using the Collard model (Collard, 2005). This is the same model which is used on the J3 side. A calibration bias of + 1.39 dB for

side-A and 1.31 dB for side-B is applied to the S6PP sigma0 in the computation of the wind speed. Once this is done, the wind speeds from the two altimeters agree with a standard deviation less than 10 cm/sec (Fig. 25-left) and with a similar histogram shape (Fig. 25-right).

The time series for the difference between S6PP LRM and J3 SWH (Fig. 26-left) and for the difference between the S6PP LRM and J3 wind speed (Fig. 26-right) exhibit a bias around -1.8 cm for SWH and around 0.6 cm/s for the wind speed. Just after the transition to side-B, the wind speed difference is slightly noisier because of the CAL-1 power jittering at high frequency, as reported in (Dinardo et al. 2022).

6.2. LRM stability analysis and errors

The paper (Dinardo et al., 2022) observed that the Poseidon-4 PTR shape does not evolve in a perfectly symmetrically way between the left and right side of the PTR and the PTR undergoes a compression of the main-lobe 3 dB width, as far as side-A is concerned.

The standard internal path delay methods (like the classic half-power method) have some difficulties in capturing these asymmetric evolutions of the PTR shape, see for instance (Poisson et al. 2019) and (Dinardo et al. 2019),

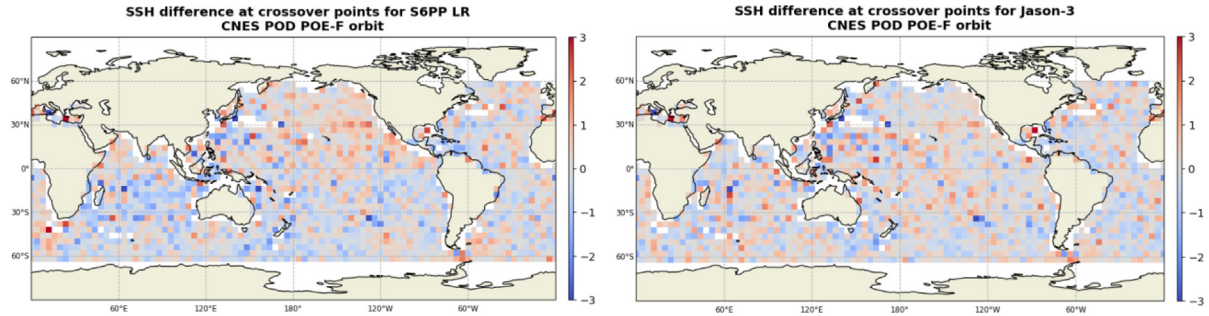


Fig. 18. Time series of the difference between S6PP LRM and J3 SSHA in the case of the CNES POD orbit (left, red for ECMWF WTC and blue for AMR-C WTC) and in the case of the JPL orbit (right, orange for ECMWF WTC and cyan for AMR-C WTC case).

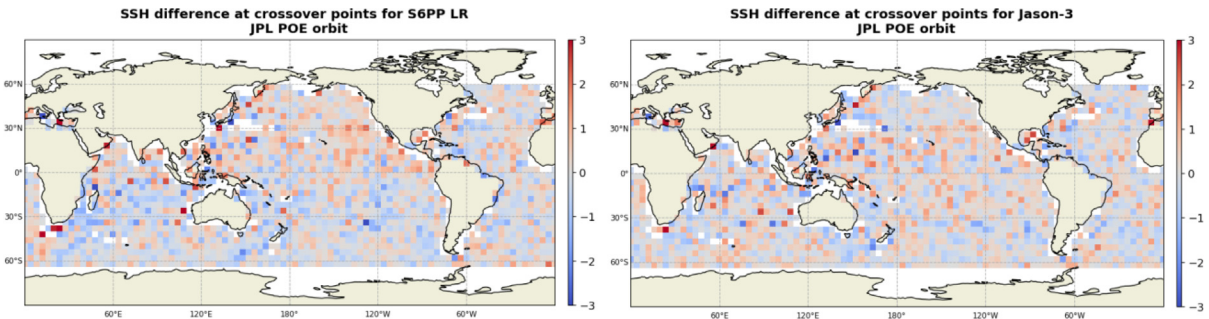


Fig. 19. Crossover map of the SSH difference mean (cm) for S6PP LRM (left) and J3 (right). Both cases are made with the CNES POD orbits. The axis unit is the degree.

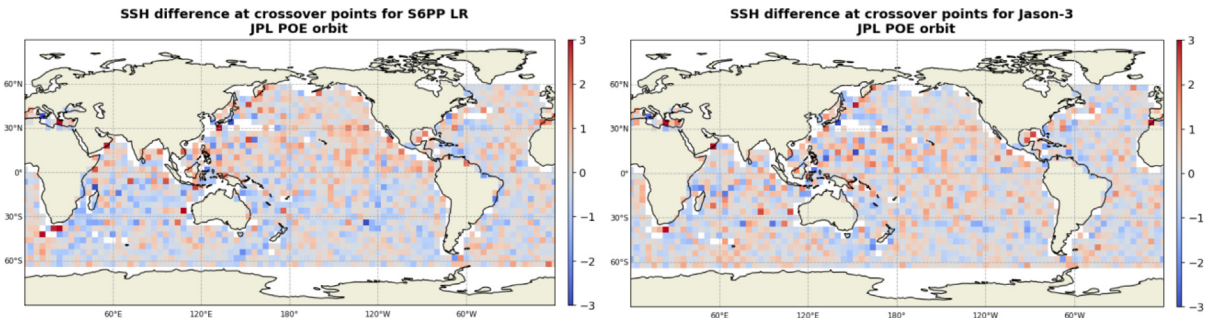


Fig. 20. Crossover map of the SSH mean (cm) for S6PP LRM (left) and J3 (right). Both cases are made with the JPL orbits. The axis unit is the degree.

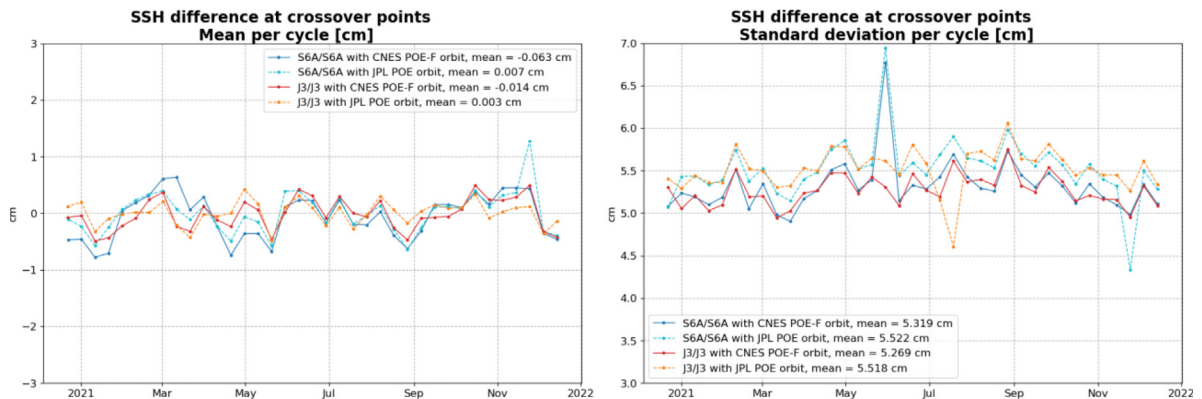


Fig. 21. J3 and S6PP LRM time series of the SSH crossover mean (left) and standard deviation (right).

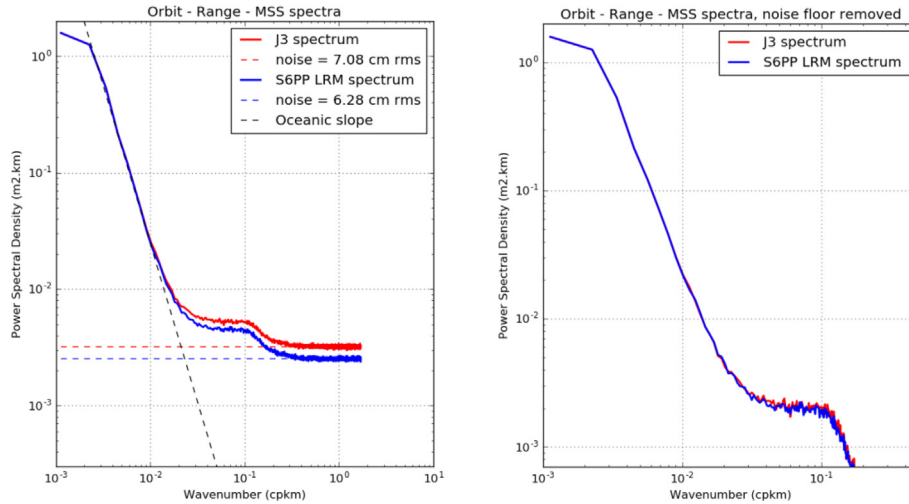


Fig. 22. S6-MF and J3 wavenumber spectra for orbit-range-mean sea surface XXX when the noise floor is not removed (left) or is removed (right). The spectra are computed over 20 days.

whereas the main-lobe compression is expected to drive an over-estimation of the SWH measurement level.

In this section, we aim to assess the impact of these dissymmetries and of the main-lobe width evolution in term of erroneous range and SWH drift using the S6PP LRM numerical retracker with, on one side, the interface to the in-flight PTR and, on the other side, the interface to an ideal PTR (squared sinc). In the latter case (i.e. “without in-flight PTR”), the PDP internal path delay is part of the tracker range, whereas in the first case it is not.

Due to an anomaly in the ground processing (EUMETSAT, 2021a) that strongly impacts the stability of the NTC data, the analysis of the impact of the PTR shape evolution in LRM has moved necessarily to the STC latency for this study. The issue was solved after PDP update deployed in operations on 9th November 2022.

Once the difference between the STC LRM dataset generated without in-flight PTR and with in-flight PTR for the three geophysical quantities range, SWH and sigma0 is made, we are finally able to provide an estimation of the stability error currently committed by the PDP LRM

MLE-4 retracker in measuring the global mean sea level trend because of the on-going instrument ageing.

The reported relative drifts, for side-A, are -0.48 mm/year for the range, 8.1 mm/year for the SWH and 0.005 dB/year for the sigma0 (see Fig. 27).

The side-B appears to be more stable than the side-A in term of relative drifts, but the time period is too short to draw any conclusions.

In the range time series, the jump occurring on 28 April 2021 is relative to a satellite’s restart operation. There is another jump in the range time series of about 0.5 mm at the transition between side-A and side-B: also in this case, after the switch-over, the range difference went back to a similar value (around $+2$ mm) as seen on side-A at the beginning of the tandem phase. Such offset will not impact the GMSL quality as it is later calibrated in the GMSL time series.

With regard to the SWH time series, a jump of 5 mm can be observed at the switch-over between side-A and side-B which is related to a slightly different 3 dB PTR main-lobe width value between side-A and side-B, as reported in (Dinardo et al. 2022): after the switch-over, the SWH

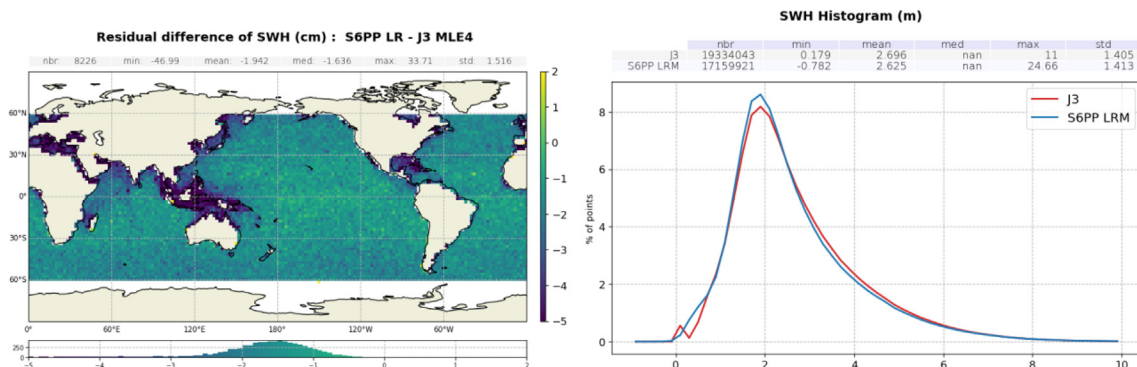


Fig. 23. Geographical map of the difference between J3 and S6PP LRM SWH (left) and the histogram (right).

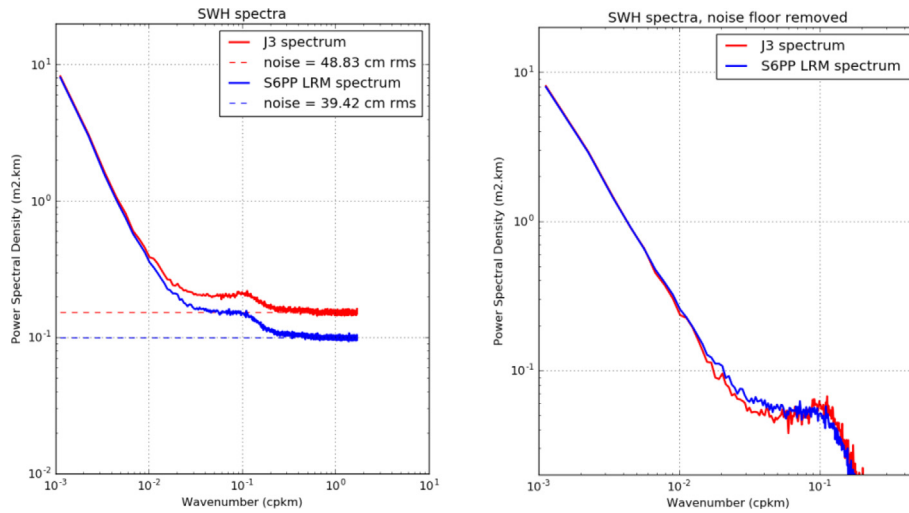


Fig. 24. S6PP LRM and J3 wavenumber spectra for SWH once the noise floor is not removed (left) or is removed (right).

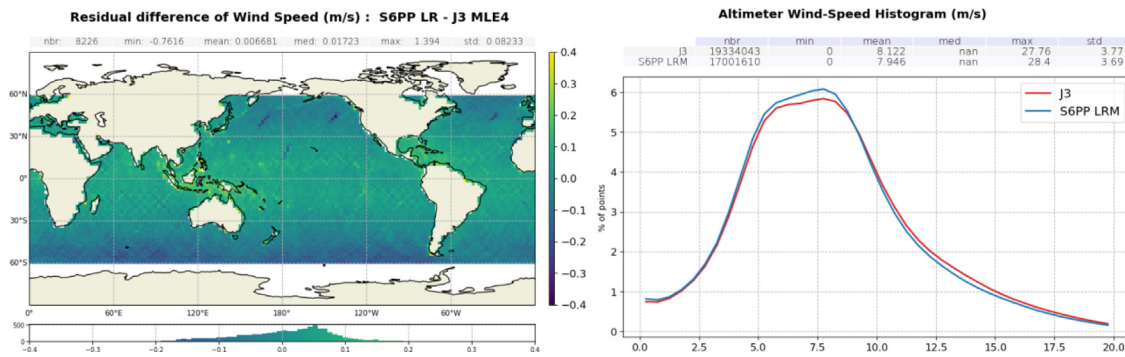


Fig. 25. Geographical map of the difference between the J3 and S6PP LRM wind speed (left) and the histogram (right).

level went back to the value (around 0 mm) as seen on side-A at the beginning of the tandem phase.

The jumps in sigma0 time series occurring on 26 August 2021 and on 14 September 2021 are relative to a PDP anomaly (special altimeter calibrations treated as nominal and added in the LTM file) (EUMETSAT, 2021a). This issue was solved with a PDP update deployed in operations on 9 November 2021.

In addition to the direct impact of range drift on the sea level stability, there is also an SWH contribution on the sea level drift via the sea state bias. This contribution is evaluated here to be 0.03 times the SWH (as in Poisson et al., 2019). Considering both range and SWH contributions to the sea level drift, it is thus estimated that, due to ongoing instrumental ageing, the PDP side-A LRM sea level measurement has drifted by:

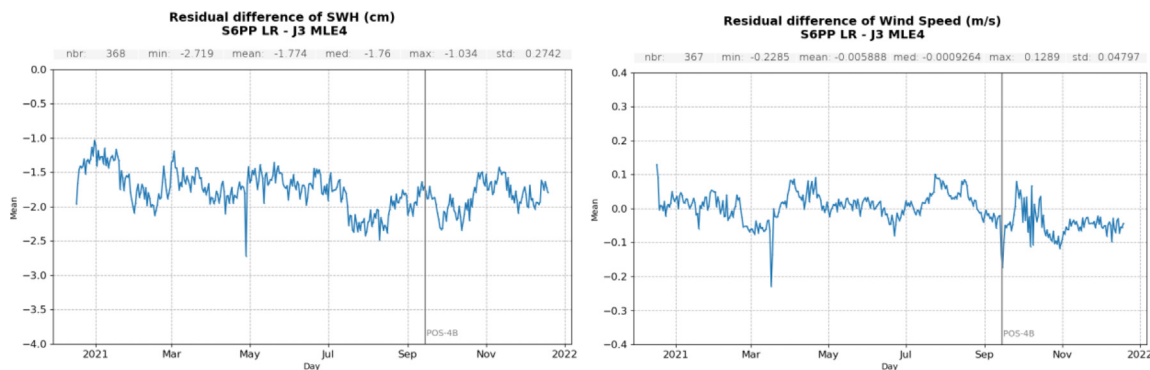


Fig. 26. Time series of the difference between S6PP LRM and J3 SWH (left) and between S6PP LRM and J3 wind speed (right).

$$\text{drift}_{\text{sl/LRM}} = 0.48 + 0.03 \cdot 8.04 = 0.75 \text{ mm/year} \quad (45)$$

assuming a sea state bias given by the 3% of SWH.

This drift is more than double that reported by (Poisson et al., 2019) for Sentinel-3A, which is reasonable given the stronger instrumental ageing of S6-MF with respect to Sentinel-3A.

In conclusion, using the in-flight PTR in the S6PP processing allows the instrument ageing to be calibrated out in the final sea level computation and remove a large error from the GMSL time series.

The time series of the squared mis-pointing estimated from the waveform is displayed in Fig. 28. In green, the evolution of the sun beta-prime angle (Vallado, 2007) is added in overlap to highlight the correlation between them. On 18 January 2021, there was a patch to the on board star tracker assembly which resulted in a better platform mis-pointing. Since the mis-pointing is a variable estimated from the waveform via retracking, the instability of the platform pointing in the early mission phase has no effect on the LRM SSHA stability.

The occurrence of three cross-maneuvres (10 February, 14 April, 24 May 2021) are also annotated in Fig. 28, as well as the occurrence of the Poseidon-4 side switch-over. The waveform mis-pointing mean value is therefore around $0.002^{\circ 2}$, which is considered to be the result of the reported roll bias and pitch bias, as estimated by the cross-maneuvres.

To quantify the stability performances of the S6PP LRM global mean sea level with respect to the one from Jason-3, we compare the two respective time series during their tandem phase. Such configurations enable cancelling out the geophysical differences between the two missions (sea state and atmosphere) and precisely observe the discrepancies originating from the altimeter and radiometer instruments. We use the full S6-MF side-A data in NTC latency and the GDR-F Jason-3 L2-Plus products. Fig. 29 (top) shows that the two GMSL time series agree closely, with differences of around ± 4 mm at worst (bottom). To guarantee this continuity, an offset of 2.1 ± 0.3 mm (1-sigma) has been applied to the S6-MF time series. Such offset uncertainty is of the same order as the other reference missions (Guérou et al., 2022) and guarantees the continuity of the GMSL reference time series.

We also assess the potential drift difference between the S6PP and Jason-3 GMSL (Fig. 29-bottom) using an ordinary least square fit (as described in Ablain et al. 2019) combined with a matrix of variance–covariance of the errors to quantify the trend uncertainty. The errors budget is constructed as in Jugier et al. (2022) in the case of a tandem phase. We find a drift of 2.9 ± 3.4 mm/year (at the 5–95% confidence level). Therefore, within the large uncertainty (expected on these short periods), it can be said that the S6PP LRM data are not drifting as compared to Jason-3. To assess the potential drift of the order of the GMSL stability requirement (about 0.3 mm/year), it is necessary

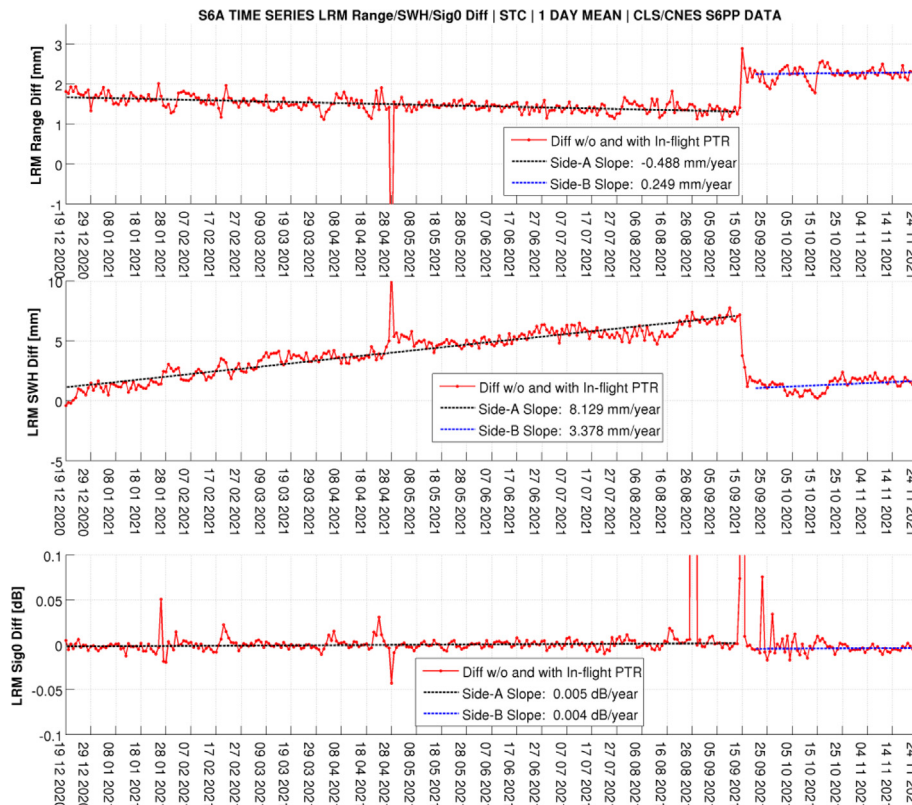


Fig. 27. Time series of the difference between the LRM range (top), SWH (middle), sigma0 (bottom) between the case without in-flight PTR and the case with in-flight PTR for the STC latency.

to wait for a longer time series and/or to test a new configuration such double tandem phases.

6.3. HRM Cal/Val and sensitivity analysis

Similarly to S6PP LRM, a full assessment of the S6PP HRM dataset is carried out over open ocean. For this Cal/Val analysis, the 1 Hz STC latency is used from the beginning of the tandem phase till December 2021.

The quality assessment of the HRM range is performed with respect to the S6PP LRM. With the implementation of a skewness parameter in the S6PP HRM processing, the difference between the two retrievals does not exceed 1 cm, with a low dependency to sea state conditions. The range difference between HRM and LRM is limited to half-cm for LRM SWH ranging between 1 m to 8 m (see Fig. 30).

In order to quantify any variation that depends on the track orientation, we apply the same method as in (Raynal et al., 2019): two maps of HRM-LRM range difference are computed, one for the ascending and one for the descending tracks. Then, we perform the differences between these two maps. It enables removing the systematic errors and only highlighting the ascending versus descending tracks differences. The result (see Fig. 31) seems to show a correlation to meridional wind speed map, as it has formerly been reported for the Sentinel-3A SAR dataset (Raynal 2019). The amplitude of the ascending minus descending patterns are of the order of a couple of cm.

In Fig. 32, the geographical map of the difference between the S6PP HRM SWH and the S6PP LRM SWH is shown (left-hand side), along with its dependency with respect to the S6PP LRM SWH (right-hand side).

As clearly shown in Fig. 32 (right-hand side), there is a strong dependency with the LRM SWH (up to 60 cm for larges waves) of the difference between SWH HRM and

SWH LRM. This dependency has been related to the orbital wave velocity effect, which is expected to be stronger in Sentinel-6 than in Sentinel-3 (Boy et al., 2022). The difference between ascending and descending of HRM minus LRM SWH map does not highlight patterns correlated to echo centering as has been observed with the Sentinel-3 data (Raynal et al., 2019), nor another significant pattern (see Fig. 33). This improvement is due to the better echo centering in the open-loop tracking mode in the case of Sentinel-6 because of the bigger size of the Sentinel-6 OLTC digital elevation model.

To compute the S6PP HRM SSHA, the wet tropospheric correction from S6-MF PDAP AMR-C and the filtered ionospheric correction from the Jason-3 IGDR-F are used. The sea state bias is recomputed using the Jason-3 GDR-F sea state bias solution applied to the S6PP HRM data (i.e. to the S6PP HRM SWH and wind speed). The difference between the S6PP HRM SSHA and the S6PP LRM SSHA (Fig. 34) shows an average bias of 1.1 cm with a low sea state dependency. Part of the remaining differences can be linked to the meridional wind effect observed on HRM range and also to the impact of the vertical ocean velocity on the HRM retrievals.

For the S6PP HRM analysis, a spectral analysis is performed on the SSHA without applying geophysical corrections (this is orbit – range – mean sea surface). The wavenumber spectra presented in Fig. 35 are computed for the J3 IGDR-F, S6PP LRM and S6PP HRM dataset on the same sets of points for all datasets.

For wavelengths larger than 100 km, the three spectra are overlaid over the oceanic slope, meaning that the three datasets have the same capacity to detect the oceanic signal down to 100 km. Between 50 and 100 km, the HRM spectrum continues to follow the oceanic slope, while this is not the case for LRM S6PP and J3. It highlights the capacity to retrieve oceanic signals at a higher resolution for HRM

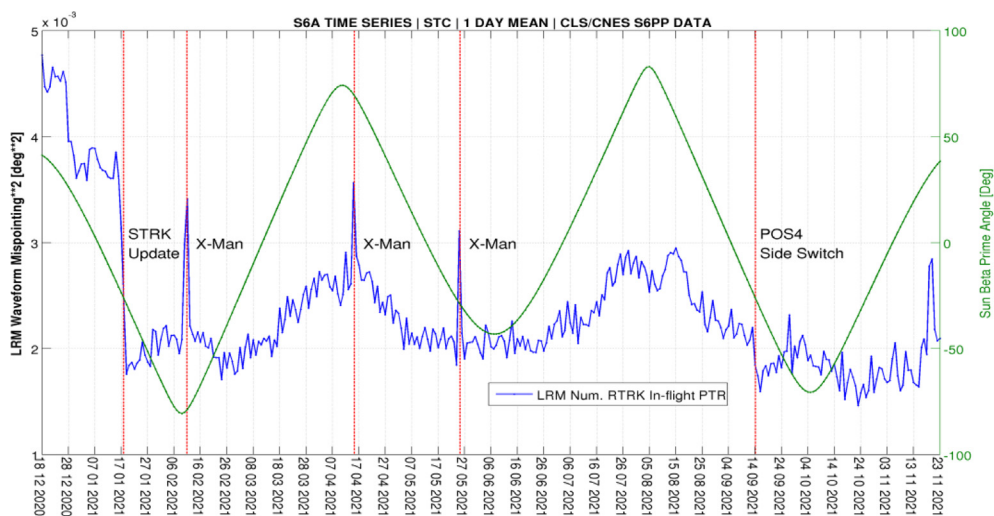


Fig. 28. Time series of the STC waveform squared mis-pointing (blue) with sun beta-prime angle in overlap (green).

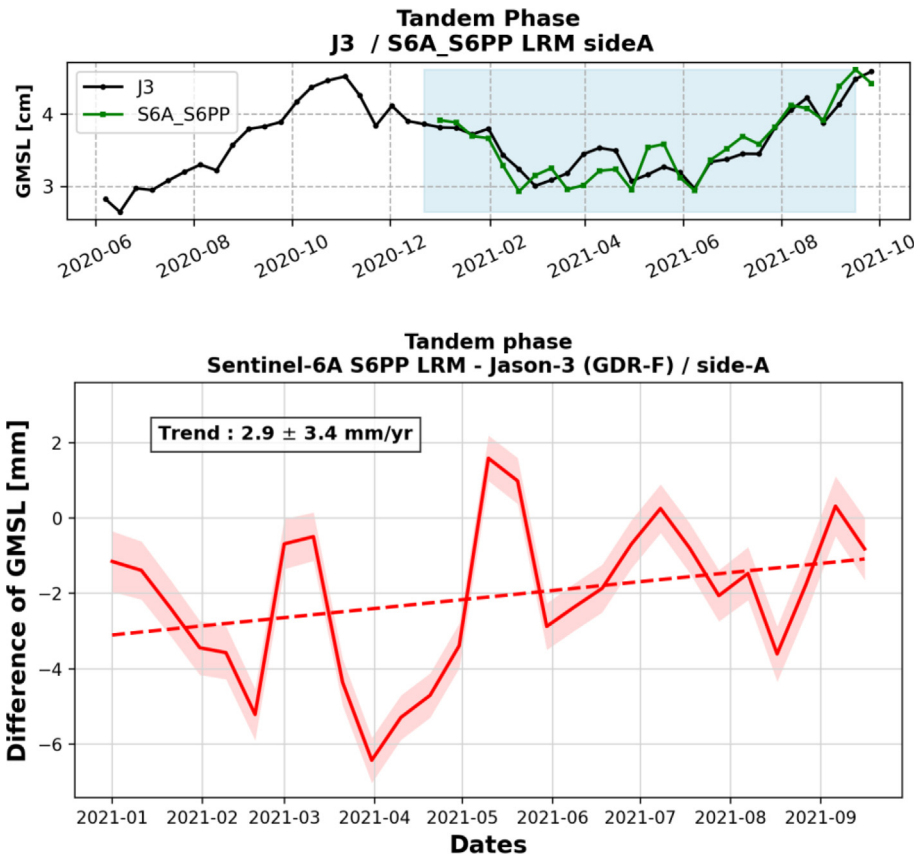


Fig. 29. S6PP LRM and Jason-3 GMSL (top plot) and trend with uncertainty of the GMSL difference (bottom plot).

S6PP (down to 50 km) than for LRM S6PP and J3 (down to 100 km).

For shorter wavelengths, the HRM spectrum is different from the S6PP LRM and J3 spectra since at these wavelengths the HRM spectrum decreases in power following the so-called “red noise” power spectrum, characteristic of the HRM SLA spectrum (Vergara et al., 2019).

Therefore, the wavenumber spectra analysis confirms the superiority of the HRM SSHA dataset with respect

to J3 and S6PP LRM, with a smaller level random noise level.

A sensitivity analysis of the impact of the ocean topography’s skewness coefficient value of 0.1 in HRM is carried out compared to the LRM dataset. As shown in Fig. 36-left, the impact in range of the 0.1 skewness coefficient is mainly a sea state bias of around -0.4% of SWH, which is close to the impact reported historically in LRM (Thibaut et al., 2005), given by:

$$\Delta R = -\frac{\lambda_s}{24} \cdot SWH$$

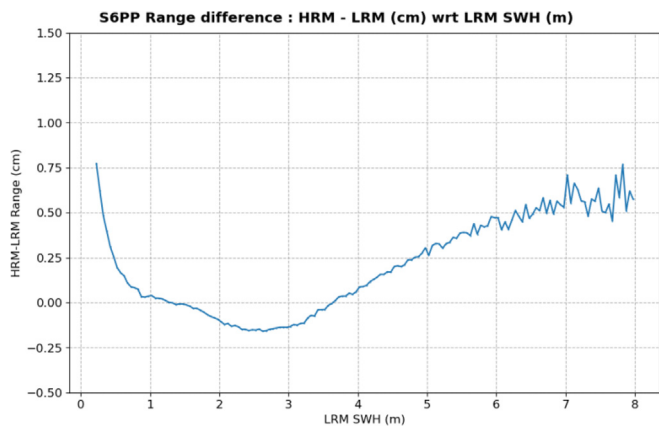


Fig. 30. Difference between S6PP HRM and LRM ranges versus LRM SWH.

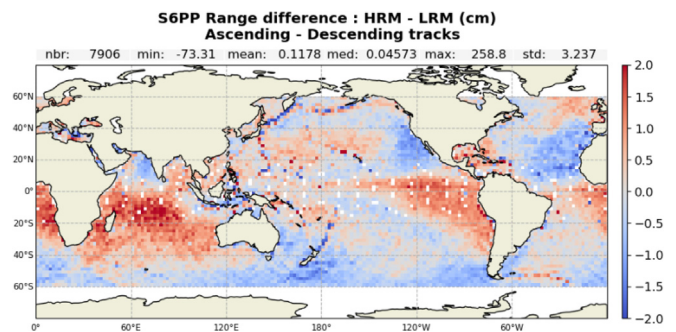


Fig. 31. Geographical map of the difference between ascending S6PP HRM – LRM range and descending S6PP HRM – LRM range.

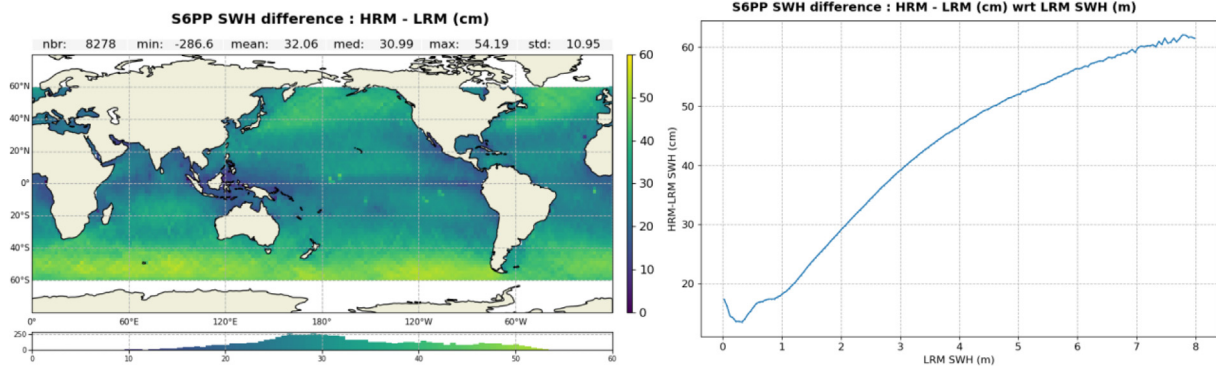


Fig. 32. Geographical map of the difference between S6PP HRM and LRM SWH (left) and S6PP HRM-LRM SWH versus LRM SWH (right).

Regarding the HRM SWH, the impact is almost null for all the sea states conditions (see Fig. 36-right).

A sensitivity analysis is also carried out by varying the number of looks (Nlook) of the multi-looking process, which corresponds to the along-track size of the stack: it has been observed that when this Nlook is reduced by a stack’s sub-setting process (see Fig. 37), the consistency between HRM SWH and LRM SWH improves very significantly and the relative bias between the two modes goes down to less than 10 cm for Nlook = 112 (Fig. 38-right). The wavenumber spectra in Fig. 39 and Fig. 40 reveal how, reducing Nlook, the S6-MF HRM SWH measurements are more in line with the J3 SWH at long scales without a detrimental increase of the level of the noise. This improvement in HRM SWH bias arising from the stack’s sub-setting process is deemed to stem from the fact that the stack’s outer (off-nadir) beams are more impacted by the wave orbital velocity effect than the nadiral ones.

With regard to the range, the impact also exists but only at millimetric level (Fig. 38-left) and only for the waves greater than 2 m. When reducing Nlook less than 224 looks, the SSHA spectrum detaches from a linear behaviour much earlier and the level of the noise increases sig-

nificantly (for Nlook = 224, the noise level increase is 12% compared to Nlook = 448 case).

6.4. HRM stability analysis and errors

As far as the HRM data stability analysis is concerned, the impact of the range walk correction application (i.e. via ABS + CZT beam-forming) is first assessed with respect to the case in which the range walk correction is omitted (i.e. via ABS + FFT beam-forming).

This is of particular relevance since the range walk correction is currently not applied on the PDP data science processing side (EUMETSAT, 2021b) and because of the on-going Poseidon-4 instrumental ageing. In the case of Sentinel-3A, whose radar altimeter also suffered instrumental ageing in the first year of the mission, an impact up to -2 mm/year from the omission of the range walk correction (Aublanc et al, 2020) has been reported for the SAR range stability.

In Fig. 41, the time series of the differences between the two cases (without and with range walk) for the geophysical quantities range, SWH and sigma0 are shown in the case of the STC latency.

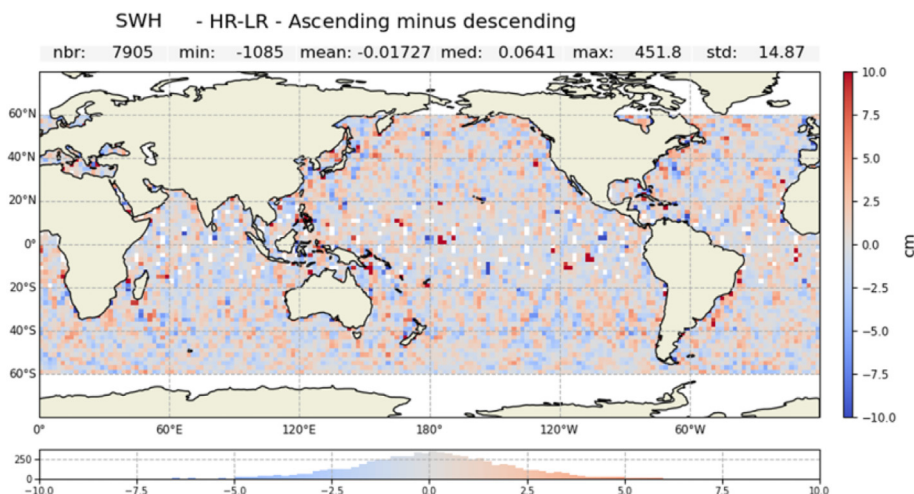


Fig. 33. Geographical map of the difference between ascending S6PP HRM minus LRM SWH and descending S6PP HRM minus LRM SWH.

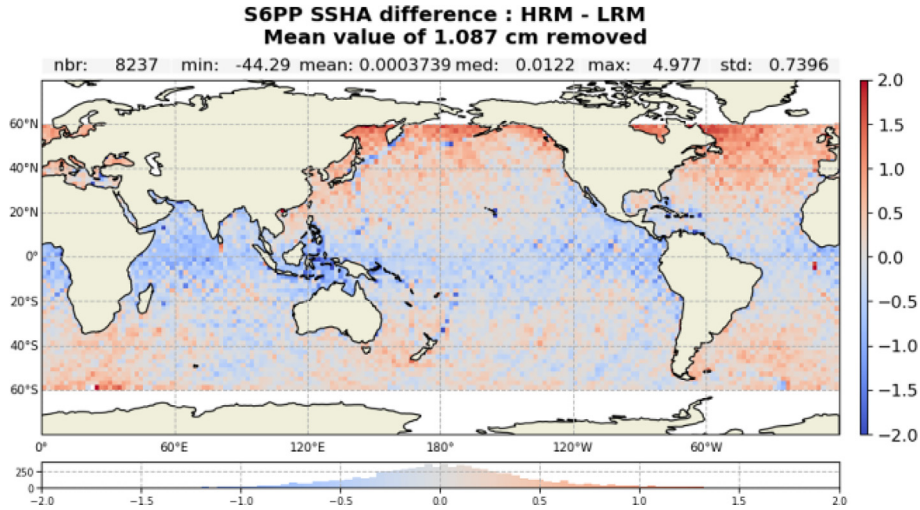


Fig. 34. Geographical map of the difference between S6PP HRM minus LRM SSHA.

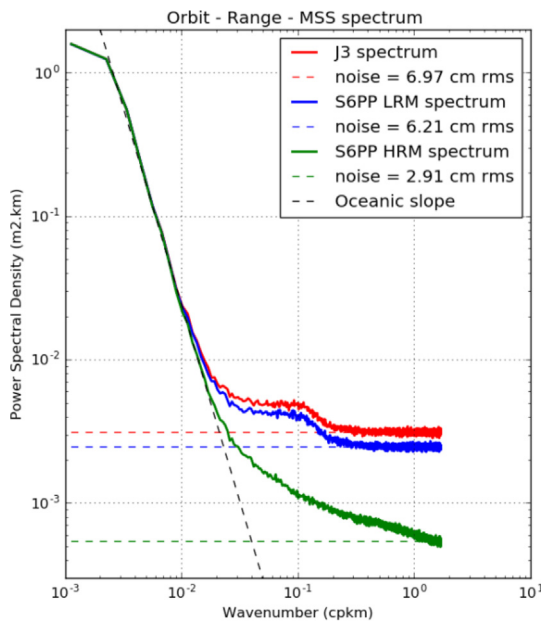


Fig. 35. SSHA wavenumber spectra for S6-MF HRM (green curve), LRM (blue curve) and J3 (red curve). The SSHA are relative to the cycle 27.

For the range, the omission of the range walk correction gives rise to a significant drift in the HRM range measurement which is estimated at -1.76 mm/year for side-A. The effect appears to be still on-going for side-B, but the time period is too short to draw any conclusions.

The reason why the omission of the range walk correction gives rise to a drift in the HRM range measurement is not yet fully understood and is currently under investigation.

There is also a clear jump of about 1.5 mm on the time series concomitant with the Poseidon-4 side switch-over: it seems that, once switched to side-B, the range walk impact went back to the value seen on side-A at the beginning of the tandem phase (+0.8 mm).

The magnitude of this drift is consistent with the analogous strong drift estimation reported for Sentinel-3A in the first year of its mission (Aublanc et al, 2020) and appears to be linked to the on-going Poseidon-4 instrumental power decay, which is similar between side-A and side-B (Dinardo et al., 2022).

On top of the linear drift, some patterns with an amplitude of 0.5 mm and related to the variation of the sun beta-prime angle (and hence to the in-orbit temperatures) show up.

As for SWH, the application of the range walk reduces the HRM SWH level by a value between 4.5 and 5 cm, whereas the sigma0 is not impacted significantly by the application of this correction (a part from a bias of + 0.002 dB).

Next, the time series of the difference between S6PP HRM and S6PP LRM for range, SWH and sigma0 is computed and displayed in Fig. 42. In it, the HRM data are processed with the range walk and both HRM and LRM data are retracked with a retracker interfacing to the in-flight PTR.

From it, it appears that the range measurement between HRM and LRM is stable for side-A with a mean value around -2 mm. The side-B period, instead, is too short to allow to draw any conclusions.

As far as SWH is concerned, the HRM is affected by a strong bias related to the wave orbital velocity effect (Egido et al., 2021b) (Maraldi et al., 2021) which amounts to 33 cm, but also varies seasonally between 36 and 30 cm.

As for sigma0, since the satellite platform nadir-pointing improved between the beginning of the tandem phase (18 December 2021) and 18 January 2021 as a result of the on board star tracker patch and since the HRM data are retracked with constant mis-pointing angles, there is a slight variation in the HRM sigma0 level (about 0.03 dB) between 18 December 2020 and 18 January 2021 compared to LRM.

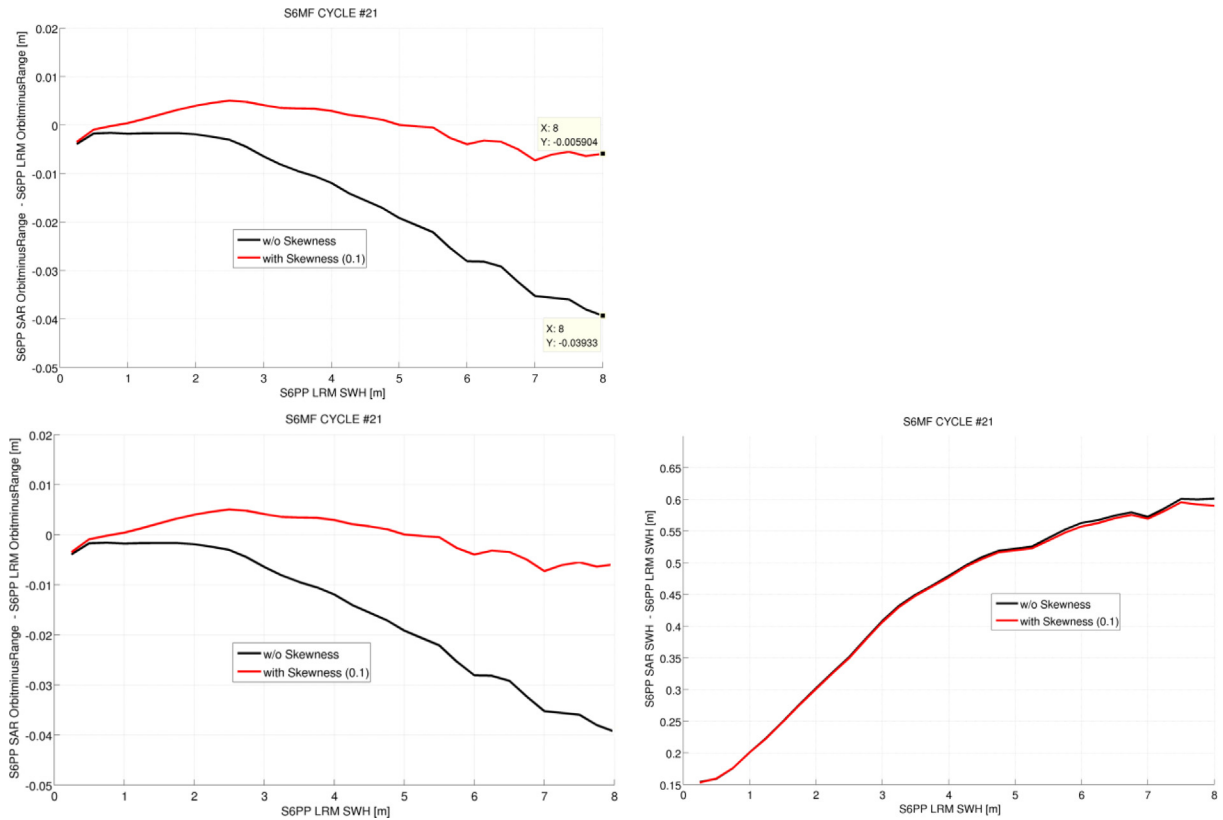


Fig. 36. Impact of changing the skewness coefficient from 0 to 0.1 for S6PP HRM orbit minus range (left) and for S6PP HRM SWH (right) compared to S6PP LRM.

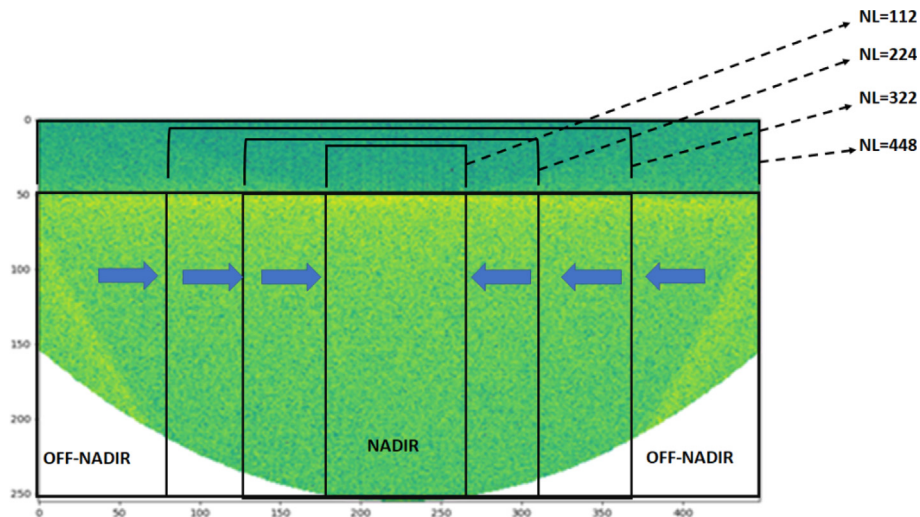


Fig. 37. Stack’s sub-setting process: only the looks from the different sizes of the stack data are accumulated during the multi-looking.

In order to recover from this spurious HRM σ_0 level variation, it would be necessary to retrack HRM data using as input the platform mis-pointing angles as estimated by the star trackers.

After 18 January 2021, three spurious spikes caused by the operated cross-maneuvres appear in the σ_0 difference of Fig. 42-bottom.

Finally, no significant jump in Fig. 42 is observed concomitantly with the transition between Poseidon-4 side-A

and side-B when making the difference between HRM and LRM for all three geophysical quantities range, SWH and σ_0 .

In conclusion, assuming that the impact of the range PTR shape evolution is similar between LRM and HRM, (following Poisson et al., 2019 who found very comparable results between Pseudo-LRM and SAR for Sentinel-3A), the expected drift in the PDP HRM sea level (side-A) is estimated to be 0.75 mm/year (due to the PTR shape

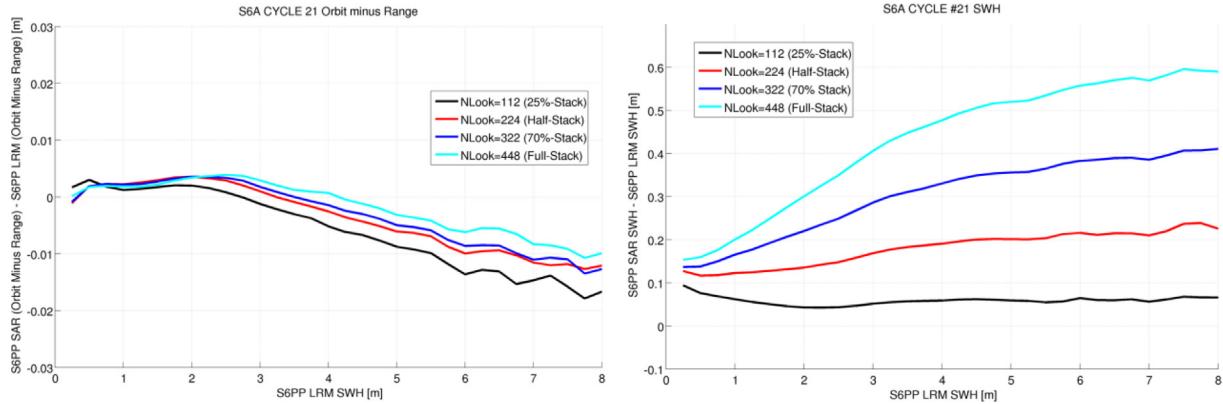


Fig. 38. Impact of the reduction of the number of looks (Nlook) for S6PP HRM orbit minus range (left) and for S6PP HRM SWH (right) compared to S6PP LRM.

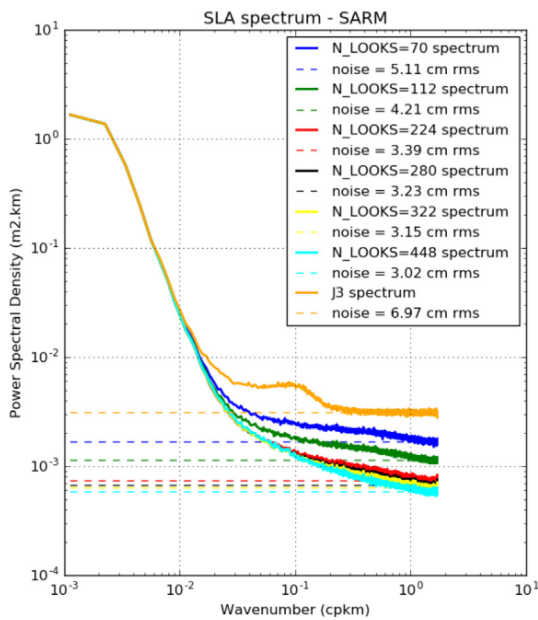


Fig. 39. Impact of the reduction of the number of looks on the S6PP HRM SSHA wavenumber spectrum.

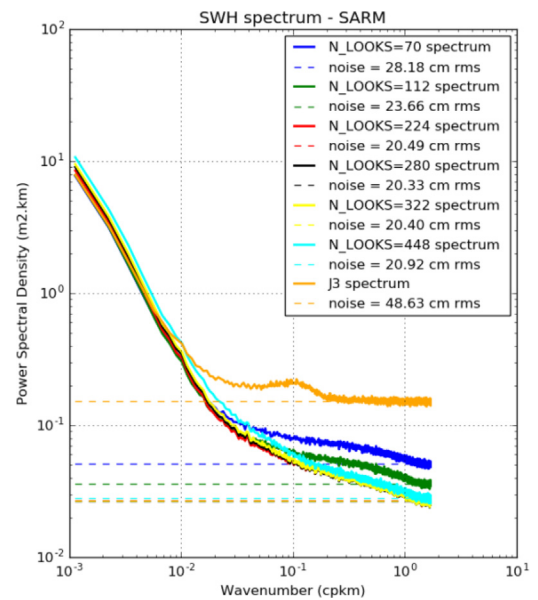


Fig. 40. Impact of the reduction of the number of looks on the S6PP HRM SWH wavenumber spectrum.

evolution) plus 1.76 mm/year (due to the range walk omission), i.e. around + 2.5 mm/year in total (see also Table 5).

7. Conclusions

The first satellite of the European Union Sentinel-6 constellation, named after Dr Michael Freilich, was launched on 21 November 2020 and the first radar altimetry data successfully acquired on 28 November 2020.

In this study, we have presented the more relevant results from the CLS/CNES S6PP prototype relative to the LRM and HRM science chains in the first year of the mission, during which the satellite was in the commissioning phase.

Both S6PP LRM and HRM chains feature a novel frequency domain numerical retracking approach with an interface to the in-flight PTR. In addition, the HRM chain

has the possibility to apply the range walk correction via a Chirp Zeta-Transform technique in the approximate beam-steering configuration.

In the S6PP LRM data flavour, the Cal/Val analysis highlighted the excellent agreement between the Jason-3 mission and the S6-MF mission results. The only reported significant discrepancy has been linked to a west-east hemispheric bias which is mitigated once the JPL orbits are used in post-processing. This hemispheric bias is also mitigated after a CNES POD orbit update consisting in blocking the GNSS phase ambiguities for the orbit computation (in operation after cycle 22).

As regards the LRM measurement stability, the impact of the dissymmetry evolution between the left and right side of the PTR and PTR main-lobe width evolution has been assessed and quantified at around -0.5 mm/year for the range and 8.1 mm/year for the SWH, which leads to

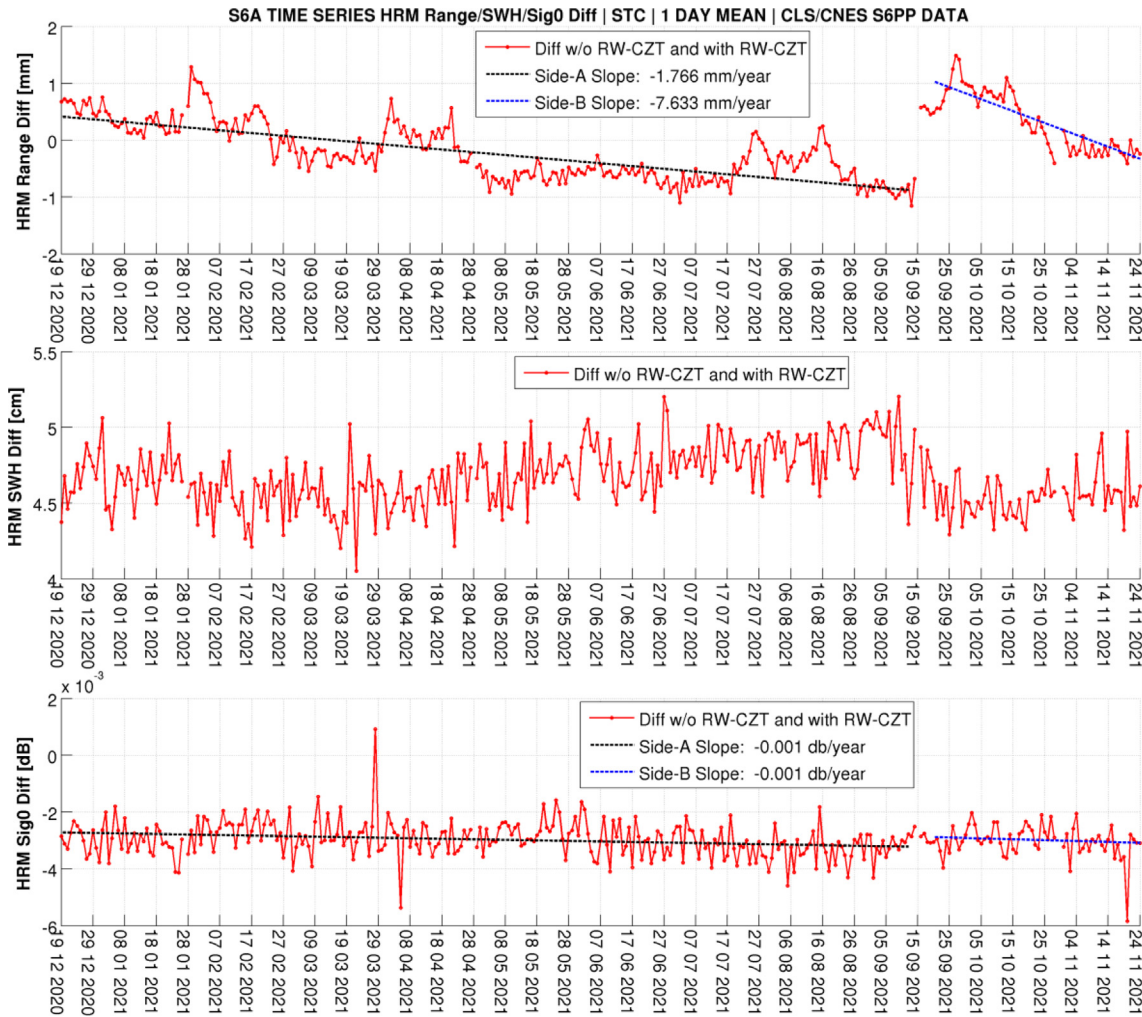


Fig. 41. Time series of the difference between the HRM range (top), SWH (middle), sigma0 (bottom) between the case without range walk (FFT-based beam-forming) and the case with range walk (CZT-based beam-forming) for the STC latency.

a drift error in the sea level measurement of 0.75 mm/year for side-A, which is very close to the S6-MF GMSL drift requirement of 1 mm/year. Once the interface to the in-flight PTR is activated inside the LRM numerical retracking, the S6PP LRM data are reported to not drift as compared to Jason-3 (within the large uncertainty expected on these short periods) and the offset uncertainty (0.3 mm at 1 sigma) is of the same order as the other reference missions.

As far as the S6PP HRM data flavor is concerned, the ascending-descending difference between S6PP HRM and LRM ranges has pointed out the existence of the geographical patterns with an amplitude of a couple of cm, which are correlated to the meridional wind speed map, as previously reported for Sentinel-3A SAR data (Raynal et al., 2019). This ascending versus descending pattern is not present in the case of SWH and wind speed.

In addition, the difference between HRM and LRM SWH has a strong dependency with SWH (errors up to 60 cm for larges waves), which was related to a wave orbi-

tal velocity effect stronger for Sentinel-6 than for Sentinel-3 (Boy et al., 2019).

Furthermore, for the first time, the impact of the ocean topography’s skewness coefficient value of 0.1 is assessed in UF-SAR mode and it is reported to be linear (around 0.4% of SWH), which is very similar to the one historically known in LRM. The favourable impact of the stack’s sub-setting process on the HRM SWH bias reduction and on the wavenumber spectrum shape is characterised for several values of the number of looks. This reduction in the number of looks does not worsen the SWH level of noise, but this is no longer the case insofar as it concerns the range.

From a spectral standpoint, the superiority of HRM versus LRM is highlighted by the spectral analysis since between 50 and 100 km, HRM spectrum continues to follow the oceanic slope, while this is not the case for S6PP LRM. This confirms the HRM capacity to retrieve the oceanic signal at a higher resolution (down to 50 km) than



Fig. 42. Time series of the difference between the HRM and LRM for range (top), SWH (middle), sigma0 (bottom) for the STC latency. The range walk (via CZT-based beam-forming) is applied on HRM side and both HRM and LRM are retracked with the numerical retracker using the in-flight PTR interface.

Table 5
Estimated stability error for PDP SSHA in LRM and HRM because of the instrument ageing and because of the range walk correction omission in the PDP (the latter just for HRM).

Drift	LRM	HRM
SSHA	+0.75 mm/year	+2.5 mm/year

for LRM S6PP and J3 (down to 100 km) and with a smaller random noise level.

As already reported by (Aublanc et al., 2019) for Sentinel-3A, the omission of the range walk correction has a very strong impact on the HRM range stability, given the on-going Poseidon-4 power decay and that is regarded as an absolutely essential correction to apply in UF-SAR processing in order to derive consistent GMSL between LRM and UF-SAR mode. Its impact in range for side-A has been estimated to be around -1.75 mm/year which is higher than the GMSL drift requirement of 1 mm/year

and appears to be still on-going for side-B. The impact is not just a linear drift since, once the range walk correction is omitted, spurious patterns with an amplitude of 0.5 mm and driven by the in-orbit temperatures may end up being assimilated in the final HRM sea level measurements.

Once the range walk correction is applied, the S6PP LRM and HRM range measurements no longer exhibit a relative drift between them and it is therefore expected that the S6PP HRM range measurements would also not drift compared to Jason-3.

Given all the results presented in this paper, we conclude that a numerical retracking with an interface to the in-flight PTR enables an accurate calibration of the instrument in power, range, and bandwidth, thus:

- ensuring the continuity between Sentinel-6 Michael Freilich and the Jason missions series in measuring GMSL trend
- guaranteeing the continuity of the GMSL reference time series, once S6-MF takes the role of reference mission

Table 6
Meaning of the symbols used in the paper.

Symbol	Meaning
c_0	speed of light
R_{Earth}	local Earth radius
f_c	RF carrier frequency
λ_0	RF wavelength
BW	useful (or reception) chirp bandwidth
F_s	digitiser sampling frequency
α	chirp slope (absolute value)
sgn_{chirp}	sign of the chirp slope
PRF	pulse repetition frequency
PRI	pulse repetition interval
N_b	number of pulses per burst
N_p	number of range bins per pulse
G_0	antenna power gain at boresight
G	antenna power gain
G_{cr}	antenna gain in the across-track dimension
G_{al}	antenna gain in the along-track dimension
$\Delta\theta_{x3dB}$	3 dB antenna aperture in the along-track dimension
$\Delta\theta_{y3dB}$	3 dB antenna aperture in the across-track dimension
v_r	satellite radial velocity
V_s	satellite velocity
H	satellite altitude
R_{trk}	tracker range
R	range between sensor and a generic scatterer
(x, y, z)	coordinates of a generic scatterer
θ_{Look}	look angle
t	fast time
t_0	epoch
f	range frequency
η	slow time
λ_s	ocean topography skewness coefficient
v	inverse of mean-square-slope
σ_0	backscattering coefficient
ξ^2	antenna squared mis-pointing
P_u	waveform amplitude
SWH	significant wave-height
SSHA	sea surface height anomaly

The in-flight PTR may also come from the ECHO CAL calibration mode (after averaging it for a proper period of time) in place of CAL-1 SAR RAW (as done in this study) in order to correct for any instrumental impact from:

- any intra-orbital thermal variations in the case of high sun beta-prime angle period
- any instrumental on board events occurring at very high frequency, such as after a satellite or altimeter restart operation
- jitter noise on the internal path power as reported in the case of a high sun beta-prime angle period for Poseidon-4 side-B.

Finally, given the strong HRM SWH bias arising from the wave orbital velocity effect, one of the open challenges to be addressed in the future for the Sentinel-6 Michael Freilich mission will be how to mitigate this effect and thus how to properly compute a sea state bias solution in HRM.

Symbols Table
(See Table 6).

Declaration of Competing Interest

The authors declare that they have no known competing financial interests or personal relationships that could have appeared to influence the work reported in this paper.

Acknowledgements

The authors wish to thank EUMETSAT for providing the Sentinel-6 Michael Freilich PDAP data products, the NASA JPL for the orbit solutions, the European Space Agency (ESA) for the Sentinel-6 Michael Freilich expertise and sensor characterisation data and CNES for the financial funding (under SALP 200443 contract and DOPPLER OCEAN 220142/00 contract), expert support, cloud-storage and cloud computing. We would like also to acknowledge the anonymous reviewers for their painstaking revision which helped to improve the final quality of the paper. Finally, we would like thank Francesca Haack and Maddalena Cellerino (CNES language translation service) for the final proof-reading of the paper.

References

- Ablain, M., Meyssignac, B., Zawadzki, L., Jugier, R., Ribes, A., Spada, G., Benveniste, J., Cazenave, A., Picot, N., 2019. Uncertainty in satellite estimates of global mean sea-level changes, trend and acceleration. *Earth Syst. Sci. Data* 11 (3), 1189–1202. <https://doi.org/10.5194/essd-11-1189-2019>.
- Amarouche, L., Thibaut, P., Zanife, O.Z., Dumont, J.P., Vincent, P., Steunou, N., 2004. Improving the Jason-1 ground retracking to better account for attitude effects. *Mar. Geod.* 27 (1–2), 171–197. <https://doi.org/10.1080/01490410490465210>.
- Amraoui, S., and the Sentinel-MF Mission Transponder Working Group (2021): New results of Sentinel-6 Transponder Working Group. 3rd Sentinel6 Validation Team Meeting, October 2021. https://cdn.events-force.net/files/ef-xnn67yq56yglu/website/29/3.1-amraoui_s._._new_results_of_sentinel-6_transponder_working_group.pdf.
- Aublanc, J., Dinardo, S., Cadier, E., Raynal, M., Moreau, T., Boy, F., Picot, N., Maraldi, C. and Femenias, P., 2020a. Impact of the Range Walk Processing in the Sentinel-3A Sea Level Trend. Virtual Presentation Ocean Surface Topography Science Team Meeting (Virtual). Available on-line at the URL: https://ostst.avisio.altimetry.fr/fileadmin/user_upload/tx_ausycslseminar/files/S3A_range_drift_OSTST_3.pdf.
- Beckman, P., Spizzichino, A., 1963. *The Scattering of Electromagnetic Waves From Rough Surfaces*. Oxford Pergamon Press, Oxford.
- Boisot, O., Amarouche, L., Lalaurie, J., Guérin, C., Dec. 2016. Dynamical properties of sea surface microwave backscatter at low-incidence: correlation time and Doppler shift. *IEEE Trans. Geosci. Remote Sens.* 54 (12), 7385–7395. <https://doi.org/10.1109/TGRS.2016.2601242>.
- Boy, F., Callahan, P., Desjonqueres, J.D., Egido, A., Smith, W.H.F., Fornari, M., Martin-Puig, C., 2022. High-Level Instrument Processing Summary for Jason 3 and Sentinel-6 Michael Freilich Tandem Phase. Oral Presentation, Ocean Surface Topography Science Team Meeting (Virtual). Available on-line at the URL: https://ostst.avisio.altimetry.fr/fileadmin/user_upload/OSTST2022/presentations/01-Jason3and-Sentinel-6MFTandemPhaseInstrumentProcessing_20220321.pdf.
- Buchhaupt, C., Fenoglio-Marc, L., Dinardo, S., Scharroo, R., Becker, M., 2018. A fast convolution-based waveform model for conventional and unfocused SAR altimetry. *Adv. Space Res.* 62 (6), 1445–1463. <https://doi.org/10.1016/j.asr.2017.11.039> (ISSN 0273-1177).

- Buchhaupt, C. 2019. Model Improvement for SAR Altimetry. Ph.D. Thesis. Darmstadt, Schriftenreihe Fachrichtung Geodäsie der Technischen Universität Darmstadt, ISBN 978-3-935631-44-0. <https://tu-prints.ulb.tu-darmstadt.de/9015/>.
- Collard, F. 2005. Algorithmes de Vent et Période Moyenne des Vagues JASON à Base de Réseaux de Neurones. BO-021-CLS-0407-RF, Boost Technologies, pp. 33.
- Copernicus Service, 2020. Web Portal News. Published on 22 November 2020. Available on-line at the URL: <https://www.copernicus.eu/en/news/news/observer-successful-launch-copernicus-sentinel-6-michael-freilich>.
- CP40 Project Report, 2014a. Algorithm Theoretical and Validation Document, CP40 Project, WP4000 Delivery Report, version 1.0. Available on-line at the URL: http://www.satoc.eu/projects/CP40/docs/CP40_WP4000_Starlab_ATBD_v1.0.pdf.
- CP40 Project Report, 2014b. Cryosat-2 Data Processing for CP40, CP40 Project, WP4000. Available on-line at the URL: <http://www.satoc.eu/projects/CP40/docs/ESRIN%20EOP-SER%20for%20CP40.pdf>.
- Dibarboure, G., Boy, F., Desjonqueres, J.D., Labroue, S., Lasne, Y., Picot, N., Thibaut, P., 2014. Investigating short-wavelength correlated errors on low-resolution mode altimetry. *J. Atmos. Oceanic Tech.* 31 (6), 1337–1362. <https://doi.org/10.1175/JTECH-D-13-00081.1>.
- Dinardo, S., 2020a. Techniques and Applications for Satellite SAR Altimetry Over Water, Land and Ice. Technische Universität, Darmstadt.
- Dinardo, S., Lucas, B., Benveniste, J., 2013. Coastal and Inland Water Altimetry at 80 Hz. OSTST Conference: Poster Presentation. Available on-line at the URL: https://www.aviso.altimetry.fr/fileadmin/documents/OSTST/2013/posters/Dinardo_coastal.pdf.
- Dinardo, S., Scagliola, M., Recchia, L., 2019. Impact of the Sentinel-3A SRAL PTR Evolution on the L2 Marine Measurements. Poster Presentation. Ocean Surface Topography Science Team Meeting (Chicago). Available on-line at the URL: https://ostst.aviso.altimetry.fr/programs/abstracts-details.html?tx_ausyclsseminar_pi2%5BobjAbstracte%5D=2811&cHash=273cd4c094c8628b2006e8ad8b132f9b.
- Dinardo, S., Moreau, M., Maraldi, C., Boy, F., Picot, N., 2020. Time and Frequency Domain Numerical SAR Retracking for Sentinel-6: First Results Prior to the S6PP Implementation. Oral Presentation, Ocean Surface Topography Science Team Meeting (Virtual). Available on-line at the URL: https://ostst.aviso.altimetry.fr/fileadmin/user_upload/tx_ausyclsseminar/files/Time_and_Frequency_Domain_Numerical_SAR_Retracking_for_Sentinel-6_First_results_prior_to_the_S6PP_implementation OSTST2020_vers1.1.pdf.
- Dinardo, S., Maraldi, C., Daguze, J.A., Amraoui, S., Boy, F., Moreau, T., Picot, N., 2022. Sentinel-6 MF Poseidon-4 radar altimeter in-flight calibration and performances monitoring. *IEEE Trans. Geosci. Remote Sens.* 60, 1–16. <https://doi.org/10.1109/TGRS.2022.3216595>.
- Doerry, A.W., 2012. Basics of Polar-Format Algorithm for Processing Synthetic Aperture Radar Images. Technical Report. Contract No. AC04-94AL85000. Sandia National Laboratories (SNL), United States. <https://doi.org/10.2172/1044949>.
- Donlon, J.C., Cullen, R., Giulicchi, L., Vuilleumier, P., Francis, C.R., Kuschnerus, M., Simpson, W., Bouridah, A., Caleno, M., Bertoni, R., Ranaño, J., Pourier, E., Hyslop, A., Mulcahy, J., Knockaert, R., Hunter, C., Webb, A., Fornari, M., Vaze, P., Brown, S., Willis, J., Desai, S., Desjonqueres, J.D., Scharroo, R., Martin-Puig, C., Leuliette, E., Egido, A., Smith, W.H.F., Bonnefond, P., Le Gac, S., Picot, N., Tavernier, G., 2021. The copernicus Sentinel-6 mission: enhanced continuity of satellite sea level measurements from space. *Remote Sens. Environ.* 258. <https://doi.org/10.1016/j.rse.2021.112395> (ISSN 0034-4257).
- Egido, A., Dinardo, S., Ray, C., 2021a. The case for increasing the posting rate in delay/doppler altimeters. *Adv. Space Res.* 68 (2), 930–936. <https://doi.org/10.1016/j.asr.2020.03.014> (ISSN 0273-1177).
- Egido, A., Buchhaupt, C., Boy, F., Maraldi, C., 2021b. Correcting for the Discrepancies in the S6-MF HR SWH measurements. In: 3rd Sentinel6 Validation Team Meeting. Available on-line at the URL: https://cdn.eventsforce.net/files/ef-xnn67yq56y/website/29/2.4-agencies_validation_noaa_vwm_final_short_version.pdf.
- Egido, A., Smith, W.H.F., 2017. Fully focused SAR altimetry: theory and applications. *IEEE Trans. Geosci. Remote Sens.* 55 (1), 392–406. <https://doi.org/10.1109/TGRS.2016.2607122>.
- Egido, A., Smith, W.H.F., 2019. Pulse-to-Pulse correlation effects in high PRF low-resolution mode altimeters. *IEEE Trans. Geosci. Remote Sens.* 57 (5), 2610–2617. <https://doi.org/10.1109/TGRS.2018.2875622>.
- ESA, 2013. Guidelines for the SAR (Delay-Doppler) L1b Processing: XCRY-GSEG-EOPS-TN-14-0042. European Space Agency/ESRIN. Frascati. Available on-line at the URL: <https://earth.esa.int/eogateway/documents/20142/37627/Guidelines-for-the-SAR-Delay-Doppler-L1b-Processing.pdf>.
- ESA, 2020. Sentinel6-MF Mission Performance Working Group Cal/Val Concept Plan. JC-TNESA-MI-0500, ESA/ESTEC Noordwijk, the Netherlands. Available on-line at the URL: <https://earth.esa.int/eogateway/documents/20142/1557871/Sentinel-6-Calibration-and-Validation-Concept-Plan.pdf>.
- EUMETSAT, 2021. Copernicus Sentinel-6 Michael Freilich Product Notice (Altimetry). November 2021. EUM/RSP/DOC/21/1230254, EUMETSAT Darmstadt, Germany. Available on-line at the URL: <https://www.eumetsat.int/media/48237>.
- EUMETSAT, 2021b. Sentinel-6/Jason-CS ALT Level 1 Product Generation Specification (L1 ALT PGS). May 2021, EUM/LEO-JASCS/SPE/17/901031, EUMETSAT Darmstadt, Germany. Available on-line at the URL: <https://www.eumetsat.int/media/48261>.
- EUMETSAT, 2021. Sentinel-6/Jason-CS ALT Level 2 Product Generation Specification (L2 ALT PGS). May 2021, EUM/LEO-JASCS/SPE/17/901321, EUMETSAT Darmstadt, Germany. Available on-line at the URL: <https://www.eumetsat.int/media/48266>.
- EUMETSAT, 2019. Sentinel-6/Jason-CS Calibration and Validation Implementation Plan. EUM/LEO-JASCS/TEN/18/981813, v2B 19 December 2019. EUMETSAT Darmstadt, Germany.
- EUMETSAT, 2020. Web Portal News. Published 09 December 2020. Available on-line at the URL: <https://www.eumetsat.int/copernicus-sentinel-6-michael-freilich-satellite-delivers-promising-first-altimeter-data>.
- Figerou, S., Urien, S., Cadier, E., Bourdeau, A., Moreau, T., Amarouche, L., Cullen, R., Fornari, M., Giulicchi, L., Figa-Saldana, J., Scharroo, R., Bignalet-Cazalet, F., 2020. Jason-CS Level-2 Processing Development from GPP To PDAP: Performance Analysis and Validation Strategy Using Both Simulated Sentinel-6 and Real Sentinel-3 Data. Virtual Presentation Ocean Surface Topography Science Team Meeting (Virtual).
- Frigo, M., Johnson G.S., 1998. FFTW: An Adaptive Software Architecture for the FFT. Proceedings of the International Conference Acoustics, Speech, and Signal Processing. Seattle, WA: The Institute of Electrical and Electronics Engineers, May 1998, vol. 3, pp. 1381–1384.
- Gommenginger, C.P., Martin-Puig, C., Amarouche, L., Raney, R.K., 2013. SAR Mode Error Budget Study: Review of State of Knowledge of SAR Altimetry over Ocean. EUMETSAT Ref. EUM/RSP/REP/14/749304, version 2.2, Darmstadt, Germany. Available on-line at the URL: http://nora.nerc.ac.uk/id/eprint/507775/1/SARAltimetry_Review_JasonCS_EUMETSAT.pdf.
- Guccione, P., 2008. Beam sharpening of delay/doppler altimeter data through chirp zeta transform. *IEEE Trans. Geosci. Remote Sens.* 46 (9), 2517–2526. <https://doi.org/10.1109/TGRS.2008.918863>.
- Guccione, P., Scagliola, M., Giudici, D., 2018. 2D frequency domain fully focused SAR processing for high PRF radar altimeters. *Remote Sens. (Basel)* 10 (12). <https://doi.org/10.3390/rs10121943>.
- Guérou, A., Meyssignac, B., Prandi, P., Ablain, M., Ribes, A., Bignalet-Cazalet, F., 2022. Current Observed Global Mean Sea Level Rise and Acceleration Estimated from Satellite Altimetry and the Associated Uncertainty. *EGU sphere*. <https://doi.org/10.5194/egusphere-2022-330>.
- Hayne, G., 1980. Radar altimeter mean return waveforms from near-normal-incidence ocean surface scattering. *IEEE Trans. Antennas Propag.* 28 (5), 687–692. <https://doi.org/10.1109/TAP.1980.1142398>.

- Hayne, G.S., Hancock, D.W.I.I., 1982. Sea-State-related altitude errors in the SEASAT radar altimeter. *J. Geophys. Res.* 87 (C5), 3227–3231. <https://doi.org/10.1029/JC087iC05p03227>.
- Lipa, B.J., Barrick, D.E., 1981. Ocean surface height-slope probability density function from SEASAT altimeter echo. *J. Geophys. Res.* 86 (C11), 10921–10930. <https://doi.org/10.1029/JC086C11p10921>.
- MacArthur, J., 1976. Design of the SEASAT-a radar altimeter. *Oceans '76*, 222–229. <https://doi.org/10.1109/OCEANS.1976.1154217>.
- Maraldi, C., Boy, F., Cadier, E., Dinardo, S., Guerou, A., Moreau, T., 2021. S6-MF HR Product Quality over Ocean. 3rd Sentinel6 Validation Team Meeting, October 2021. Available on-line at the URL: https://cdn.eventsforce.net/files/ef-xnn67yq56yly/website/29/2.2-2021-10-21-s6vt_calval_over_ocean.pdf.
- Moreau, T., Aublanc, J., Thibaut, P., Rieu, P., Boy, F., Picot, N., Mavrocordatos, C., Borde, F., 2017. Investigation of SWH Bias in SAR Altimetry Mode. Oral Presentation, Ocean Surface Topography Science Team Meeting (Miami). Available on-line at the URL: https://ostst.avisio.altimetry.fr/fileadmin/user_upload/IPM_03_OSTST2017_InvstigBiasSwh_Tmoreau_v1.pdf.
- Oppenheim, V.A., Schaffer, W.R., 1975. *Digital Signal Processing*. Prentice-Hall International Editions, 1975 ISBN 9780132146357.
- Phalippou, L., Caubet, E., Deemster, F., Richard, J., Rys, L., Deschaux-Beaume, M., Francis, R., Cullen, R., 2012. Reaching Sub-Centimeter Range Noise on Jason-CS with the Poseidon-4 Continuous SAR Interleaved Mode. Oral Presentation at Ocean Surface Topography Science Team Meeting, Venice, Italy, 27–28 September 2012. Available on-line at the URL: https://www.avisio.altimetry.fr/fileadmin/documents/OSTST/2012/oral/02_Friday_28/05_instr_processing_jib/05_IP2B_Phalippou.pdf.
- Poisson, J.C., Piras, F., Raynal, M., Cadier, E., Thibaut, P., Boy, F., Picot, N., Borde, F., Féménias, P., Dinardo, S., Recchia, L., Scagliola, M., 2019. SENTINEL-3A Instrumental Drift and its Impacts on Geophysical Estimates. Oral Presentation at Ocean Surface Topography Science Team Meeting, Chicago. Available on-line at the URL: https://ostst.avisio.altimetry.fr/fileadmin/user_upload/2019/IPM_02_Poisson_OSTST2019_PTR_Drift.pdf.
- Poisson, J.C., Quartly, G.D., Kurekin, A.A., Thibaut, P., Hoang, D., Nencioli, F., 2018. Development of an ENVISAT altimetry processor providing sea level continuity between open ocean and arctic leads. *IEEE Trans. Geosci. Remote Sens.* 56 (9), 5299–5319. <https://doi.org/10.1109/TGRS.2018.2813061>.
- Rabiner, L.R., Schafer, W.R., Rader, M.C., 1969. The Chirp Z-Transform algorithm and its application. *Bell Syst. Tech. J.* 48, 1249–1292 https://ia802704.us.archive.org/33/items/bstj48-5-1249/bstj48-5-1249_text.pdf.
- Raney, R.K., 1998. The delay doppler radar altimeter. *IEEE Trans. Geosci. Remote Sens.* 36 (5), 1578–1588. <https://doi.org/10.1109/36.718861>.
- Raney, R.K., 2012. CryoSat SAR-mode looks revisited. *IEEE Geosci. Remote Sens. Lett.* 9 (3), 393–397. <https://doi.org/10.1109/LGRS.2011.2170052>.
- Ray, C., Martin-Puig, C., Clarizia, M.P., Ruffini, G., Dinardo, S., Gommenginger, C., Benveniste, J., 2015. SAR altimeter backscattered waveform model. *IEEE Trans. Geosci. Remote Sens.* 53 (2), 911–919. <https://doi.org/10.1109/TGRS.2014.2330423>.
- Raynal, M., Cadier, E., Labroue, S., Moreau, T., Rieu, P., Féménias, P., Bordes, F., Boy, F., Picot, N., 2019. Lessons Learned from Sentinel SARM Missions in Preparation of Jason-CS. Oral Presentation, Ocean Surface Topography Science Team Meeting (Virtual). Available on-line at the URL: https://ostst.avisio.altimetry.fr/fileadmin/user_upload/2019/ERR_04_SARM_lessons_learned_raynal.pdf.
- Reale, F., Pugliese, C.E., Di Leo, A., Dentale, F., 2020. Wave orbital velocity effects on radar doppler altimeter for sea monitoring. *J. Marine Sci. Eng.* 8 (6). <https://doi.org/10.3390/jmse8060447>.
- Rieu, P., Aublanc, J., Dinardo, S., Poisson, J.C., Cadier, E., Raynal, M., Moreau, T., Boy, F., Picot, N., Maraldi, C., 2020. Analysis of the Sentinel-3A SAR Range Drift. In: Presentation at S3 STM Mission Performance Center ESL Council Meeting #7, 4-5 June 2020.
- Rieu, P., Moreau, T., Cadier, E., Raynal, M., Clerc, S., Donlon, C., Borde, F., Boy, F., Maraldi, C., 2021. Exploiting the Sentinel-3 tandem phase dataset and azimuth oversampling to better characterize the sensitivity of SAR altimeter sea surface height to long ocean waves. *Adv. Space Res.* 67 (1), 253–265. <https://doi.org/10.1016/j.asr.2020.09.037> (ISSN 0273-1177).
- Rudin, W., 1976. *Principles of Mathematical Analysis*. McGraw-Hill, Third Edition, 9780070856134.
- Scagliola, M., Recchia, L., Maestri, L., Giudici, D., 2021. Evaluating the impact of range walk compensation in delay/doppler processing over open ocean. *Adv. Space Res.* 68 (2), 937–946. <https://doi.org/10.1016/j.asr.2019.11.032>.
- Scharroo, R., von Engeln A., 2018. Sentinel-6 End-User Requirements Document. EUM/LEO-JASCS/REQ/12/0013, v3E, EUMETSAT. Darmstadt, Germany. 29 January 2018. Available on-line at the URL: <https://earth.esa.int/eogateway/documents/20142/1557871/Sentinel-6-End-User-Requirements-Documents-EURD.pdf>.
- Scharroo, R., Bonekamp, H., Ponsard, C., Parisot, F., von Engeln, A., Tahtadjiev, M., de Vriendt, K., Montagner, F., 2016. Jason continuity of services: continuing the Jason altimeter data records as Copernicus Sentinel-6. *Ocean Sci., EGU* 12 (2), 471–479. <https://doi.org/10.5194/os-12-471-2016>.
- Thibaut, P., Amarouche, L., Zanife, O.Z., Steunou, N., Vincent, P., Raizonville, P., 2004. Jason-1 altimeter ground processing look-Up correction tables. *Mar. Geod.* 27 (3–4), 409–431. <https://doi.org/10.1080/01490410490902133>.
- Thibaut, P., Amarouche, L., Ferreira, F., Zanife, O.Z., Vincent, P., 2005. Estimation of the Skewness Coefficient Using Jason-1 Altimeter Data. *Proceedings. IEEE International Geoscience and Remote Sensing Symposium, IGARSS*, vol. 4, pp. 2556–2559. <https://doi.org/10.1109/IGARSS.2005.1525506>.
- European Union, 2014. Regulation (EU) No 377/2014 of the European Parliament and of the Council of 3 April 2014 establishing the Copernicus Programme and repealing Regulation (EU) No 911/2010 Text with EEA relevance. Available on-line at the URL: <https://eur-lex.europa.eu/legal-content/EN/TXT/?uri=CELEX%3A32014R0377>.
- Vallado, D.A., 2007. *Fundamentals of Astrodynamics and Applications*. Microcosm Press, New York/ Springer, New York.
- Vergara, O., Morrow, R., Pujol, I., Dibarboure, G., Ubelmann, C., 2019. Revised global wavenumber spectra from recent altimeter observations. *J. Geophys. Res.* 124 (6), 3523–3537. <https://doi.org/10.1029/2018JC014844>.
- Wingham, D.J., Phalippou, L., Mavrocordatos, C., Wallis, D., 2004. The mean echo and echo cross product from a beamforming interferometric altimeter and their application to elevation measurement. *IEEE Trans. Geosci. Remote Sens.* 42 (10), 2305–2323. <https://doi.org/10.1109/TGRS.2004.834352>.